



Universiteit
Leiden
The Netherlands

Exploring the interactions of M dwarf winds and cosmic rays

Mesquita, A.L.

Citation

Mesquita, A. L. (2022, October 25). *Exploring the interactions of M dwarf winds and cosmic rays*. Retrieved from <https://hdl.handle.net/1887/3484534>

Version: Publisher's Version

License: [Licence agreement concerning inclusion of doctoral thesis in the Institutional Repository of the University of Leiden](#)

Downloaded from: <https://hdl.handle.net/1887/3484534>

Note: To cite this publication please use the final published version (if applicable).

Exploring the interactions of M dwarf winds and cosmic rays

Proefschrift

ter verkrijging van

de graad van doctor aan de Universiteit Leiden,
op gezag van rector magnificus prof.dr.ir. H. Bijl,
volgens besluit van het college voor promoties
te verdedigen op dinsdag 25 oktober 2022
klokke 10:00 uur

door

Amanda Lúcia Mesquita
geboren te Lavras, Minas Gerais, Brazil
in 1992

Promotor:

Dr. A.A. Vidotto

Co-Promotores:

Dr. D. Rodgers-Lee (Dublin Institute for Advanced Studies)

Prof.dr. I.A.G. Snellen

Promotiecommissie:

Prof.dr. H.J.A. Röttgering

Prof.dr. S. Viti

Prof.dr. Ch. Helling (Austrian Academy of Sciences)

Dr. A.M. Taylor (Deutsches Elektronen-Synchrotron DESY)

Dr. N. van der Marel

Contents

1	Introduction	1
1.1	Habitable zone and exoplanet habitability	1
1.2	M dwarfs	4
1.2.1	Magnetic fields and stellar activity	5
1.2.2	Stellar winds of cool dwarfs	8
1.2.2.1	Techniques to indirectly detect stellar winds	9
1.2.2.2	What drives the wind of M dwarfs?	13
1.3	The interaction between the interstellar medium and the stellar wind .	15
1.4	Galactic cosmic rays and stellar wind interaction	18
1.4.1	Galactic cosmic ray observations at Earth and correlation with solar activity	19
1.4.2	The Local interstellar spectrum	21
1.4.3	How to infer/detect cosmic rays on other planets	23
1.5	This thesis	24
1.6	Outlook	27
2	Global trends in winds of M dwarf stars	29
2.1	Introduction	29
2.2	Alfvén-wave driven stellar wind model	31
2.3	Parametric study of winds of M-dwarfs	34
2.3.1	The structure of the wind	34
2.3.2	Global trends of M dwarf winds	36
2.4	Applications of our model	42
2.4.1	The extension of the chromosphere in inactive or moderately ac- tive M dwarfs	42
2.4.2	The wind of the planet-hosting star GJ 436	43
2.5	Discussion	46
2.5.1	Comparison between the Alfvén-wave driven wind and the Parker wind models	46
2.5.2	Different parameters of the model	47
2.5.2.1	Flux tube geometry	48

CONTENTS

2.5.2.2	Thermal properties	50
2.5.2.3	Properties of the waves	50
2.6	Conclusions	51
	Appendices	52
2.A	Further comparison between our wind models and a Parker wind	52
3	The Earth-like Galactic cosmic ray intensity in the habitable zone of the M dwarf GJ 436	55
3.1	Introduction	56
3.2	Galactic Cosmic ray propagation	59
3.2.1	Local Interstellar Spectrum (LIS)	62
3.2.2	Stellar wind parameters	62
3.2.3	What is the size of the astrosphere of GJ 436?	65
3.3	Galactic Cosmic Rays in M dwarf systems	68
3.3.1	Intensity of cosmic rays as a function of the particle's kinetic energy	68
3.3.2	Advective and diffusive timescales	69
3.3.3	The intensity of Galactic cosmic rays in the habitable zone and at GJ 436 b	71
3.4	Discussion	73
3.5	Conclusions	77
4	Galactic cosmic ray propagation through M dwarf planetary systems	79
4.1	Introduction	80
4.2	The stars in our sample	82
4.3	The stellar wind environment	84
4.3.1	The Alfvén-wave-driven wind simulation	84
4.3.1.1	Stellar surface magnetic field	86
4.3.1.2	The base density of the stellar wind	87
4.3.2	Stellar wind density, velocity and magnetic field profiles	87
4.3.3	The size of the M dwarf astrospheres	88
4.4	Cosmic ray transport	90
4.4.1	Diffusion coefficient	91
4.4.2	Local Interstellar Spectrum (LIS)	92
4.5	Galactic cosmic ray fluxes around M dwarfs	93
4.5.1	The flux of Galactic cosmic rays at the habitable zone and at planetary orbits	93
4.5.2	GJ 273 b's surface radiation dose	96

4.5.3	How are Galactic cosmic rays modulated by the magnetised wind of M dwarfs?	96
4.6	Discussion & Conclusions	100
5	The strong suppression of Galactic cosmic rays reaching AU Mic b, c and Prox Cen b	105
5.1	Introduction	105
5.2	Modelling Framework	108
5.2.1	Stellar wind properties	108
5.2.2	The astrosphere size	111
5.2.3	Cosmic ray transport equation	112
5.2.3.1	The diffusion coefficient	113
5.2.3.2	The particle drift	114
5.3	Prox Cen: the Galactic cosmic ray fluxes including particle drift effects	115
5.4	AU Mic: the effect of an unconstrained mass-loss rate on Galactic cosmic ray fluxes	117
5.5	Discussion & Conclusions	120
	Appendices	123
5.A	Galactic cosmic ray propagation in the solar system	123
5.B	Extrapolation of stellar wind profiles to the edge of the astrosphere . .	125
	Bibliography	127
	Nederlandse Samenvatting	143
	English Summary	147
	Publications	151
	Curriculum Vitae	153
	Acknowledgements	155

CONTENTS

Introduction

In this thesis, I will discuss the interaction between M dwarf stellar winds and Galactic cosmic rays and the possible effects on the habitability of exoplanets. In particular, I have used numerical simulations to describe the stellar winds of M dwarfs using observable constraints, such as the mass-loss rate, X-ray luminosity, and magnetic field strength/flux. Additionally, I have also used numerical simulations to describe the propagation of Galactic cosmic rays within M dwarfs planetary systems. With these simulations, I was able to calculate the flux of Galactic cosmic rays reaching exoplanet magnetospheres/atmospheres. Measuring cosmic ray fluxes in exoplanet atmospheres is yet not possible, but cosmic rays are an important ingredient in the context of planetary habitability. For this reason, quantifying these fluxes is essential to complete the habitability “puzzle”. Future exoplanet atmosphere observations with space telescopes, such as the James Webb Space Telescope (JWST) and the Atmospheric Remote-sensing Infrared Exoplanet Large-survey (ARIEL), will enable us to constrain cosmic ray fluxes in exoplanet atmospheres.

1.1 Habitable zone and exoplanet habitability

In the last few decades, more than 5000 exoplanets have been discovered. With so many exoplanets having been observed so far, there is a lot of interest in determining if any of these exoplanets are habitable. However, many factors are associated with the habitability of an exoplanet, such as planetary and stellar properties, stellar effects (see e.g., Meadows & Barnes, 2018) and determining if an exoplanet is habitable (or not) seems a complex problem. Fig. 1.1 shows a summary of the planet, stellar and planetary system properties that are believed to affect planetary habitability. The font colour indicates the way these properties can be obtained. Blue represents the properties that could possibly be observed, orange are properties that can be modelled using observable constraints and green are properties that can be theoretically modelled.

1.1 Habitable zone and exoplanet habitability

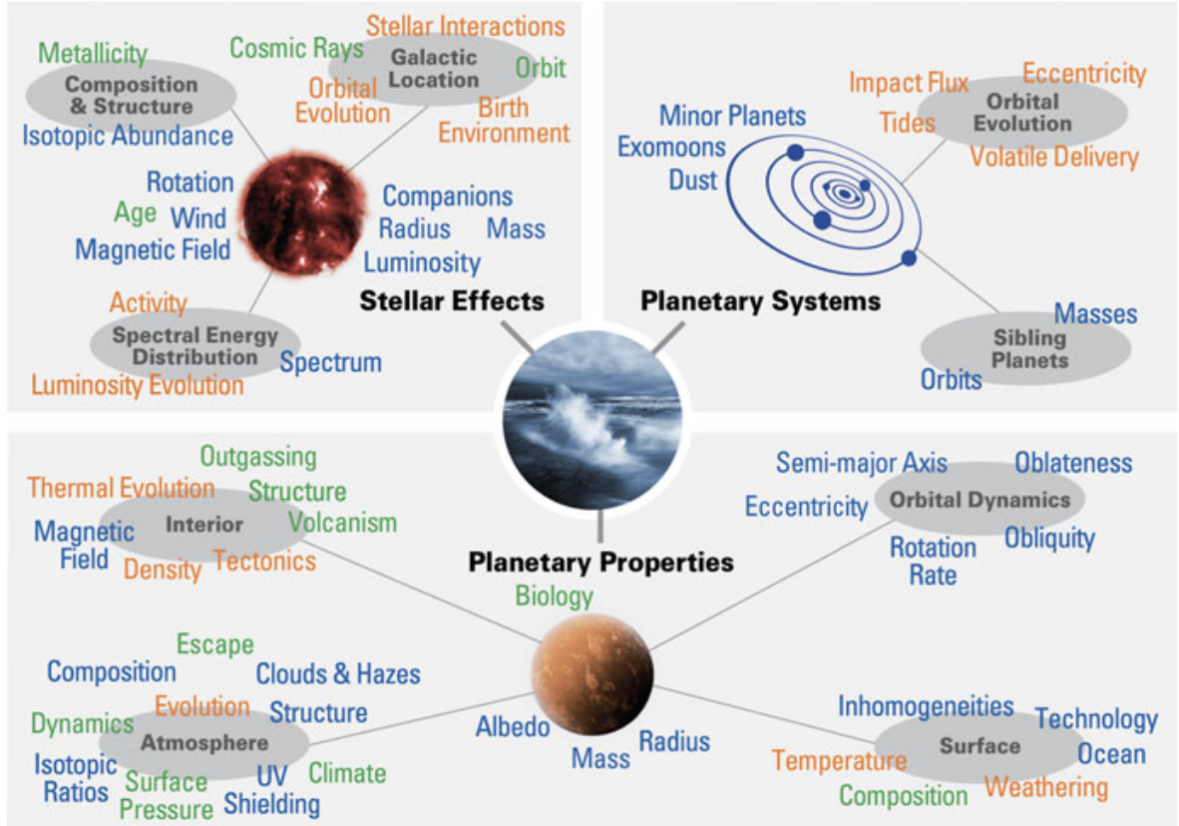


Figure 1.1: Diagram showing the possible factors affecting planetary habitability. In blue are shown possible observable properties while green are properties that require modelling with observational constraints. In orange are the properties which require theoretical modelling. Figure from Meadows & Barnes (2018).

One extremely important factor for life as we know it is the presence of liquid water¹ on the exoplanet’s surface that can be influenced by many factors including properties of the stellar system and planet itself. The circumstellar region around a star in which a planet can sustain liquid water on its surface is commonly called the habitable zone (Kasting et al., 1993; Selsis et al., 2007). This region is close-in for small stars, such as M dwarfs, and further out for F and G dwarfs, such as our Sun. Being in the habitable zone is believed to be the first condition to be important for exoplanet habitability, although it does not necessarily mean that a planet in the habitable zone is habitable.

Fig. 1.2 shows the habitable zone as a function of the stellar mass for stars of solar metallicity and effective temperature between 3700 K and 7200 K. The dark grey region is the habitable zone defined by the empirical “early Mars” and “recent Venus” criteria

¹Life as we know requires at least three ingredients: energy, “biogenic” elements (C, H, O, N and S) and a liquid solvent (see e.g., Hoehler et al., 2018). All Earth-based life needs liquid water as a solvent.

(cloud-free limits). The “recent Venus” criterion gives an empirical indication of the inner edge of the habitable zone. This criterion is due to the fact that surface maps of Venus indicate that liquid water has not been present on the planet in the last ~ 1 Gyr (Solomon & Head, 1991). At that time, the luminosity of the Sun was believed to be around 8% dimmer than its present value¹. Thus, the luminosity received by Venus, at that time, was equal to the one received today at a distance ~ 0.75 au (Selsis et al., 2007). Similar to the inner edge, the outer edge of the habitable zone can be defined by empirical indication of the early Mars conditions. The “early Mars” criterion is due to the fact that geological and geochemical characteristics show that, around ~ 4 Gyr ago, Mars was warm enough to have surface liquid water (Pollack et al., 1987; Bibring et al., 2006). The Sun’s luminosity was 28% dimmer at that time, thus the flux received at Mars was equal to what it is today at a distance of ~ 1.77 au (Selsis et al., 2007).

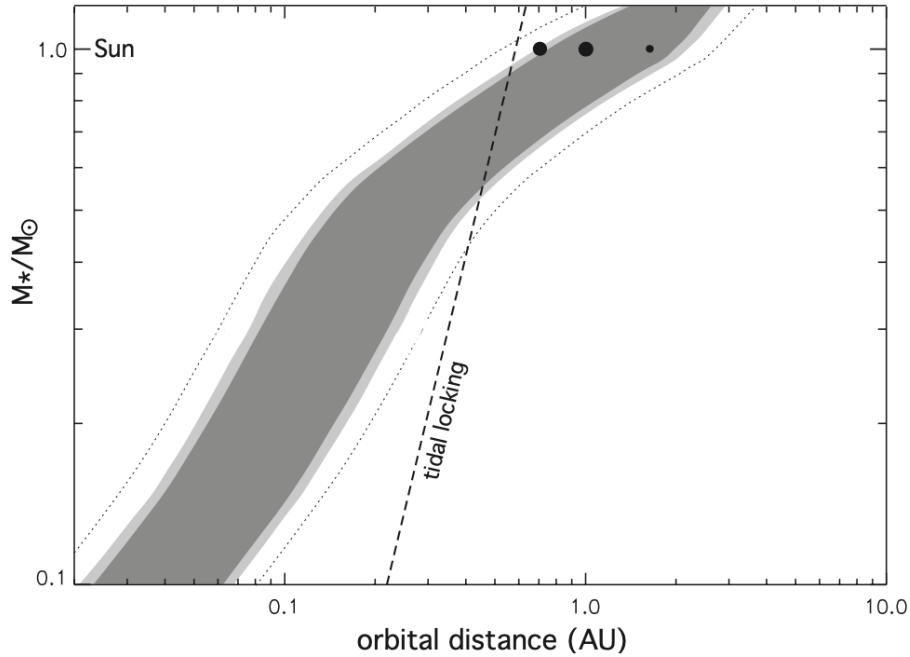


Figure 1.2: Habitable zone as a function of the stellar mass. The darker region represents the habitable zone defined by the empirical “early Mars” and “recent Venus” criteria. The light grey regions give the theoretical limits with 50% clouds and the dotted lines correspond to the theoretical limits with 100% cloud cover. The dashed line shows the distance ($\lesssim 0.7$ au) at which a $1 M_{\oplus}$ planet becomes tidally locked in less than 1 Gyr. The black dots represent Venus, Earth and Mars, respectively. Figure modified from Selsis et al. (2007).

The light grey areas of Fig. 1.2 represent the theoretical limits with 50% cloud cover

¹Solar evolution models have shown that during its lifetime in the main sequence, the Sun has slowly increased its luminosity (e.g., Neronov et al., 2017; Gough, 1981).

and the dotted lines give the theoretical limits with 100% cloud cover. H_2O -clouds can increase the planetary albedo and thus move the inner habitable zone boundary limits closer to the star by reducing greenhouse warming (Selsis et al., 2007). The presence of CO_2 -clouds, on the other hand, can extend the outer habitable zone boundary limits by warming the planet’s surface caused by a scattering variation of the greenhouse effect (Mischna et al., 2000; Selsis et al., 2007). The dashed line represents the distance ($\lesssim 0.7 \text{ au}$) at which a $1 M_\oplus$ planet becomes tidally locked (one side of the planet always faces the star, similar to the moon with respect to the Earth) in $< 1 \text{ Gyr}$. This is particularly important for M dwarfs since planets within the habitable zone are expected to be tidally locked (Kasting et al., 1993). A tidally locked exoplanet can have a low heat distribution from the day side to the night that could affect the exoplanet’s climate.

In the context of this thesis, any planet in the habitable zone will be called a potentially habitable planet. This is not the same as a “real” habitable planet, i.e., any other criteria except for the habitable zone will not be considered here.

1.2 M dwarfs

M dwarfs are by far the most common type of stars in our Galaxy, accounting for at least 70% of all the stars in our solar neighbourhood (Henry et al., 2006; Winters et al., 2015; Henry et al., 2018). They are small, main-sequence stars with masses in the range of $0.08 - 0.5 M_\odot$, low effective temperatures ($< 4000 \text{ K}$) and low brightness. All of these characteristics make M dwarfs the perfect candidates for observing exoplanets with current observing techniques, in particular rocky potentially habitable planets. Due to their low luminosities, M dwarfs present a good contrast to detect smaller-size exoplanets using the transit method, and their low masses enable the detection of lower-mass exoplanets using the radial velocity method. These exoplanet detection methods usually favour the detection of close orbiting planets.

M dwarfs are also interesting because of their close-in habitable zone which makes it easier to observe planets in these regions. The majority of planets observed around M dwarfs are located within 1 au . For these reasons, M dwarfs are currently the main targets in search of potentially habitable exoplanets. Our closest star, Proxima Centauri (Prox Cen), for instance, hosts an Earth-like planet in its habitable zone (Anglada-Escudé et al., 2016). Trappist-1 is another extremely interesting M dwarf system, as it hosts 7 planets with 4 of these planets orbiting within the habitable zone (Gillon et al., 2017).

One potential issue for exoplanet habitability is that a large fraction of main-sequence M dwarfs remain magnetically active for a longer fraction of their lives compared to solar-mass stars (West et al., 2004; Scalo et al., 2007; West et al., 2015; Guinan et al., 2016). The fraction of active M dwarfs is larger for later spectral types (e.g., West et al., 2008). Additionally, M dwarfs can generate strong kilogauss magnetic fields (Morin et al., 2010; Shulyak et al., 2019). Magnetic fields play an important role in interior (e.g., Mullan & MacDonald, 2001; Browning, 2008) and atmospheric properties (e.g., Kochukhov, 2021) of M dwarfs as well as influencing close-in exoplanets. Strong stellar magnetic activity can affect the stellar wind properties (Vidotto et al., 2014a), generate strong flares (Vida et al., 2017; Tilley et al., 2019), coronal mass ejections (Lammer et al., 2007; Khodachenko et al., 2007) and accelerate more high energy particles (Gri  meier et al., 2005). All of these phenomena can affect the exoplanets orbiting M dwarfs close-in habitable zones as well as planet habitability (Khodachenko et al., 2007; Vida et al., 2017; Tilley et al., 2019). Strong stellar winds can erode exoplanet atmospheres (e.g., Zendejas et al., 2010; Vidotto et al., 2013) while the longer exposure to stellar radiation and high energy particles can affect the planet’s climate (e.g., Grenfell et al., 2013) and possibly the planetary atmosphere (e.g., Rimmer & Helling, 2013; Rimmer et al., 2014; Tabataba-Vakili et al., 2016; Scheucher et al., 2018).

1.2.1 Magnetic fields and stellar activity

Similar to the Sun, the magnetic fields of cool dwarfs are believed to be produced by the dynamo mechanism in the interface layer, known as tachocline, between the radiative zone and the convection zone (Charbonneau, 2014). The dynamo theory describes how the magnetic field is generated inside a star. The dynamo process is complex and not fully understood even for the Sun.

Not all M dwarfs have the tachocline layer in their interior. Two scenarios exist for the interior structure of M dwarfs and those are represented in Fig. 1.3. M dwarfs with $M \gtrsim 0.35 M_{\odot}$ (early than M3.5 spectral type) have an interior similar to that of a solar-like star, with a radiative zone followed by a convective envelope. While M dwarfs with $M \lesssim 0.35 M_{\odot}$ (later than M3.5 spectral type) have a fully convective interior (Chabrier & Baraffe, 1997). Despite not having a tachocline, low-mass fully convective stars also show magnetic activity and strong magnetic fields (Route, 2016; Reiners et al., 2022). Large-scale magnetic fields are starting to be observationally reconstructed for fully

convective stars (Morin et al., 2010; Morin, 2012; Klein et al., 2021a), even though it is still not fully understood how the magnetic fields are produced in these types of stars.

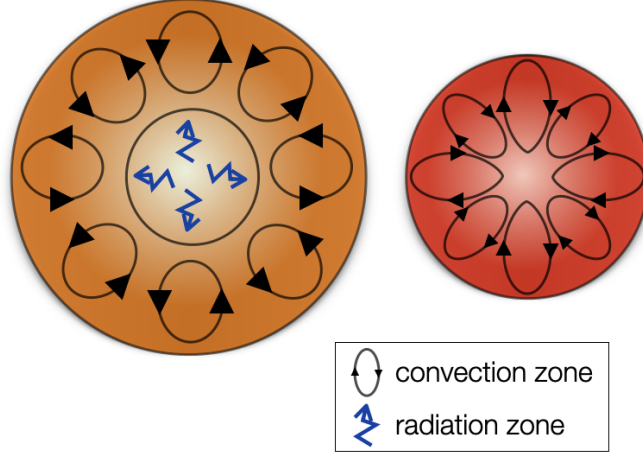


Figure 1.3: Schematic of stellar interior structure of M dwarfs. *Left:* partially convective interior, with radiative zone followed by a convective envelope. *Right:* fully convective interior.

For cool dwarfs, the large-scale magnetic field is believed to be generated by the $\alpha\Omega$ dynamo mechanism (Charbonneau, 2014). The convective zone is formed by plasma (a fluid of electrically charged particles) in continuous motion. The combination of electrically charged particles and motion creates electric currents, which generate magnetic fields, which in turn produce electric currents, and therefore a loop is generated. First, starting with a poloidal magnetic field, with a perpendicular direction, the stellar differential rotation stretches the magnetic field and winds it around the star, building a toroidal magnetic field with a horizontal direction (Ω -effect). Once the toroidal field has grown unstable, possibly due to cyclonic motions inside the star, the interaction of convection and rotation then restores a poloidal field with opposite polarity (α -effect).

In the solar case, the dynamo mechanism results in a magnetic activity cycle called the solar cycle (e.g., Hathaway, 2010). One of the best manifestations of the solar cycle is the sunspots¹ cycle. The solar cycle has a period of ~ 11 years, which is characterised by an increase and decrease in the sunspot number. This period is also characterised by a flip in the north-south orientation of the solar large-scale magnetic field. Solar activity is distinguished by two periods: a solar minimum with weak magnetic activity and few or no sunspots visible on the solar surface and a solar maximum with strong magnetic activity and an increase in the number of sunspots visible.

¹Sunspots are dark regions observed in the solar photosphere.

Other stars also show magnetic activity and measurements of the stellar magnetic field are essential to understand the dynamo process and also the many phenomena occurring in the stellar atmosphere due to magnetic activity. Photospheric magnetic fields can be directly observed by studying the Zeeman effect in which a single spectral line splits into multiple observable components due to the presence of a magnetic field. The splitting of the lines depends on the magnetic field strength. These spectropolarimetric observations show that M dwarfs can produce strong large-scale magnetic fields (Donati et al., 2006, 2008; Morin et al., 2008a,b, 2010; Hébrard et al., 2016; Moutou et al., 2017). Techniques such as Zeeman broadening and Zeeman Doppler Imaging (ZDI) are commonly used to understand the surface magnetic field properties of cool stars (e.g., Morin, 2012; Kochukhov, 2021). The Zeeman broadening method gives information on the unsigned surface magnetic field intensity (“total” magnetic field, large-scale and small-scale) while the ZDI method provides information on the large-scale stellar magnetic field geometry.

At this point, more than 300 M dwarfs have Zeeman broadening measurements (Kochukhov, 2021; Reiners et al., 2022) and more than 30 M dwarfs have ZDI observations (Donati et al., 2006, 2008; Morin et al., 2008a,b, 2010; Hébrard et al., 2016; Moutou et al., 2017). Fig. 1.4 shows the ZDI reconstruction of the large-scale magnetic field of Prox Cen with an average large-scale magnetic field of ~ 200 G (Klein et al., 2021a). The average large-scale magnetic field of Prox Cen is 3 times smaller than the average Zeeman broadening measurements (Reiners & Basri, 2008). The magnetic field above the stellar surface can be calculated using the ZDI map as a boundary and a field extrapolation technique. Fig. 1.5 shows an example of the extrapolated magnetic field topology of Prox Cen using its ZDI map as the boundary for the surface large-scale magnetic field. Prox Cen shows a large-scale magnetic field geometry with dipole and quadrupole components (Klein et al., 2021a).

X-ray emission is one of the traditional magnetic activity indicators which has been observed for many stars. Fig. 1.6 shows the correlation between X-ray luminosity and magnetic flux. The left panel shows the correlation from Zeeman broadening measurements (Pevtsov et al., 2003) and the right panel from ZDI measurements (Vidotto et al., 2014b). The magnetic field strength is proportional to magnetic flux, as $\Phi = 4\pi R_\star^2 B$, where R_\star is the stellar radius. In both panels, the magnetic flux increases with X-ray luminosity which indicates that the large-scale field and the total field increase with X-ray luminosity. This relation suggests that coronal activities are powered by magnetic fields.

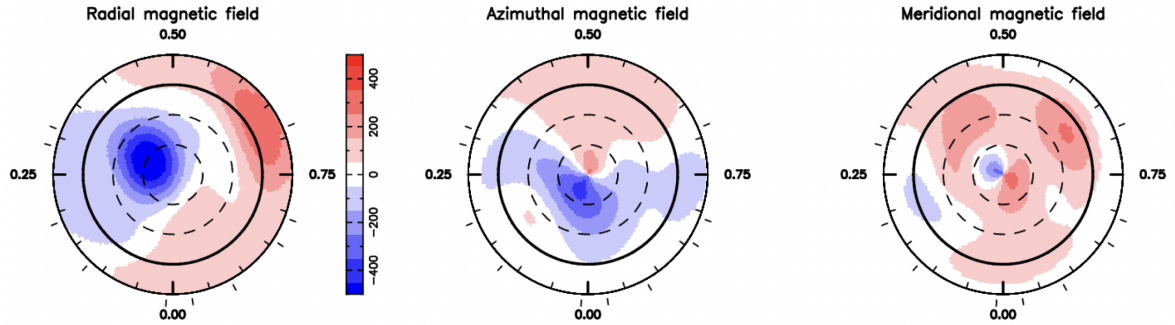


Figure 1.4: Surface distribution of the large-scale magnetic field topology of Prox Cen reconstructed with ZDI. From left to right the panels show the radial, azimuthal and meridional magnetic field components. Figure from Klein et al. (2021a).

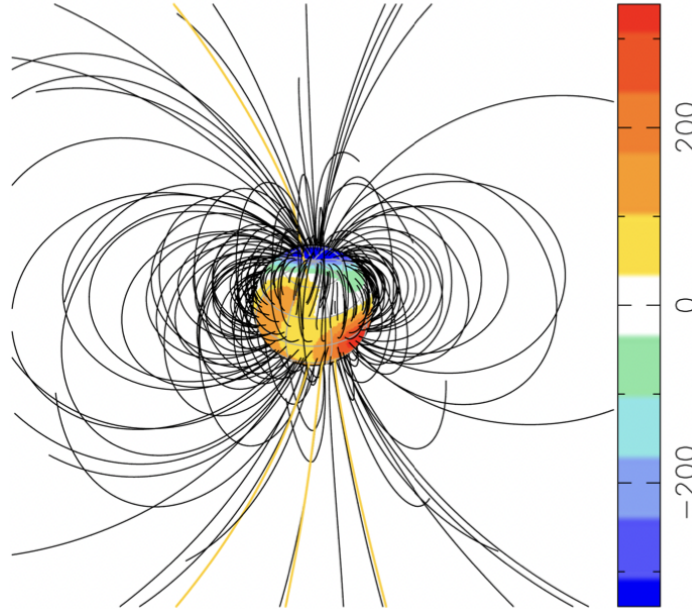


Figure 1.5: Large-scale magnetic field extrapolation of Prox Cen indicating the open and closed magnetic field lines. The color scale indicates the intensity of the radial magnetic field in Gauss. Figure from Klein et al. (2021a).

1.2.2 Stellar winds of cool dwarfs

Nearly all stars lose mass during their lifetimes in a process known as stellar wind. Stellar winds are the continuous outflow of material from the star surface (Lamers & Cassinelli, 1999). The stellar wind, and the stellar atmosphere dynamics, are dominated by the stellar magnetic field. Stellar winds play a key role in stellar evolution from the star's origin to its death (Matt et al., 2015; Johnstone et al., 2015). Stellar winds also interact with exoplanets.

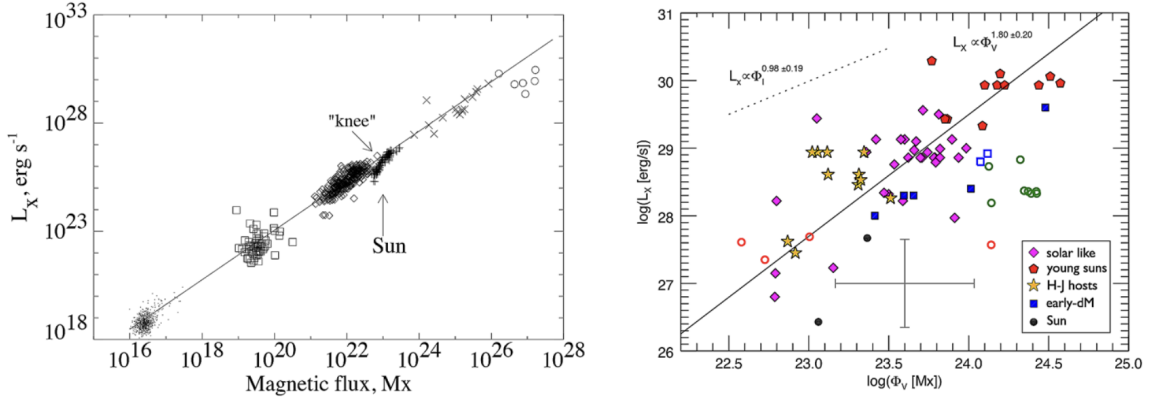


Figure 1.6: Correlation between X-ray luminosity and magnetic flux obtained from *Left:* Zeeman broadening measurements from Pevtsov et al. (2003). Dots represent the quiet Sun, squares the X-ray bright points, diamonds the solar active regions, crosses G, K, and M dwarfs, and circles the T Tauri stars. *Right:* ZDI measurements from Vidotto et al. (2014b). Open circles are the late and mid M dwarfs and are not considered in the fit. The solid lines in both panels are power-law fits.

1.2.2.1 Techniques to indirectly detect stellar winds

M dwarfs, similar to other cool dwarf stars, have very tenuous winds and, consequently, it is difficult to directly quantify them (Wood, 2004; Vidotto & Bourrier, 2017; Jardine & Collier Cameron, 2019). Fortunately, there are some techniques developed to indirectly infer the mass-loss rates of cool dwarfs. Here, I will briefly discuss some of the most successful techniques to infer mass-loss rates for cool dwarfs. A more in-depth review of the different methods can be found in Vidotto (2021).

The most successful method used to detect stellar winds is related to the study of stellar Ly- α absorption (Wood, 2004; Wood et al., 2021, and references therein). Ly- α absorption occurs when the stellar wind exchanges charges with a neutral (or partially neutral) interstellar medium (ISM). This absorption can be detectable in UV spectra. This technique favours stars within 7 pc from the Sun, because around this region the ISM is partially ionised making it possible to detect the astrospheric¹ Ly- α absorption. Beyond 7 pc the Local Bubble (which extends to ~ 100 au) is mainly fully ionised (Welsh et al., 2010).

Fig. 1.7 shows the example of α Cen B. The top panel shows the path of the stellar photons from the star towards the Sun. The middle panels show the Ly- α line profile as photons pass through the astrosphere, the ISM and the heliosphere. The purple

¹Associated with the astrosphere which is analogous to the Sun's heliosphere. The concept of an astrosphere will be discussed in Section 1.3.

regions indicate the fraction of the line absorbed in each region. The bottom panel shows the observed Ly- α profile for α Cen B. The solid line is the assumed intrinsic stellar spectrum and the dashed line is the ISM profile. The shaded regions are the excess absorption due to the astrosphere (red region) and heliosphere (green region).

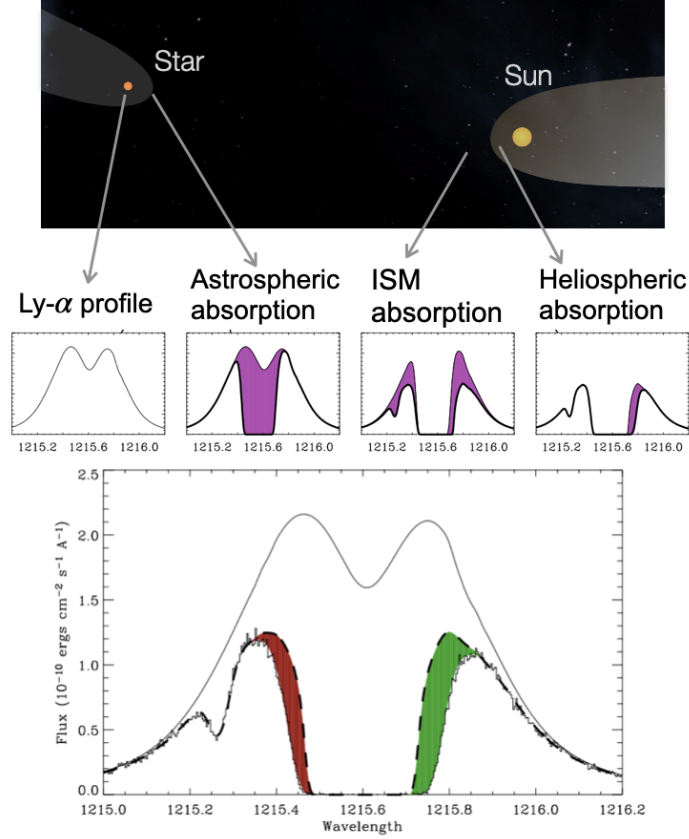


Figure 1.7: Schematic diagram of Lyman- α absorption observation. The top panel shows the Ly- α profile path from the star to the Sun. The middle panel shows how the Ly- α profile changes as it passes through the stellar astrosphere, the ISM and the heliosphere. The purple regions are the profile absorbed in each region. The bottom panel shows the observed Ly- α profile of α Cen B. The solid line is the assumed emission profile and the dashed line is the ISM line profile. The shaded regions show excess absorption from astrospheric absorption (red) and heliospheric absorption (green). Figure modified from Wood (2004).

By conducting and modelling Ly- α observations it is possible to estimate the wind ram pressure, P_{ram} (Wood et al., 2001). The mass-loss rate, \dot{M} , assuming spherical symmetry, can be determined by knowing the stellar wind terminal velocity, u_{∞} , from the relation

$$\dot{M} = \frac{4\pi R^2 P_{\text{ram}}}{u_{\infty}}, \quad (1.1)$$

where R is a given reference distance where the wind has reached its terminal velocity. By assuming the Sun’s asymptotic wind velocity of 400 km s^{-1} for all the stars in their sample, the method employed by Wood and collaborators Wood et al. (e.g., 2021) has estimated the mass-loss rate of nearly 30 stars. Almost half of this sample are M dwarfs. Some of the stars only have a mass-loss rate upper limit since the astrospheric absorption was not detected. That is the case, for instance, of Prox Cen with an inferred upper limit of \dot{M} . Prox Cen has a mass-loss rate ~ 0.2 times smaller than the solar wind mass-loss rate (Wood et al., 2001).

Another proposed method to infer the stellar mass-loss rate is the use of planet-wind interaction (Vidotto & Bourrier, 2017). This method favours planets with strong atmospheric escape, in particular close-in gas giant planets. The evaporating planet’s atmosphere can be observed in Ly- α line absorption during its transit. By modelling the Ly- α line profile it is possible to obtain the local stellar wind properties. Three stars have had their mass-loss rates constrained using this technique but only one of these is an M dwarf (Bourrier & Lecavelier des Etangs, 2013; Kislyakova et al., 2014; Vidotto & Bourrier, 2017).

The study of slingshot prominences is another method used to derive mass-loss rates of cool dwarfs (Jardine & Collier Cameron, 2019). A slingshot prominence is a very extended, bright feature extending outward from the stellar surface. This technique is successful for very fast rotating stars (Villarreal D’Angelo et al., 2018). The slingshot prominences can be detected in H- α line absorption transients as the star rotates. These transients are associated with built up material trapped within large prominences above the stellar surface (Collier Cameron & Robinson, 1989). The mass trapped in the prominence and its lifetime can be determined with H- α observations. These two quantities are then used to infer the mass of the upflow in the prominence. The stellar mass-loss rate is then estimated by knowing the prominence surface coverage. Five stars have had their mass-loss estimated using this method with mass-loss rates 2-4 orders of magnitude higher than the solar values. These fast rotating stars are very active with larger X-ray fluxes and larger mass-loss rates than the Sun.

Other techniques, such as the study of thermal radio emission from stellar winds can provide measurements of stellar wind densities (Panagia & Felli, 1975). However, due to non-detections, this method has so far only been used to derive an upper limit for mass-loss rates (Lim & White, 1996; Gaidos et al., 2000; Fichtinger et al., 2017; Vidotto & Donati, 2017).

Fig. 1.8 show the mass-loss rates derived with different methods as a function of the stellar X-ray flux. The red circles are the quantities derived using Ly- α observations

for M dwarfs. The green circles are the same for G and K dwarfs and the blue squares for subgiants/giants stars (Wood et al., 2021). The red circle #16 was derived using the exoplanet-wind interaction (Vidotto & Bourrier, 2017). The magenta squares are derived from prominences (Jardine & Collier Cameron, 2019). The arrows represent upper limits for the mass-loss rate. The dashed line is the power-law fit to the data excluding the subgiants/giants stars (shown in black).

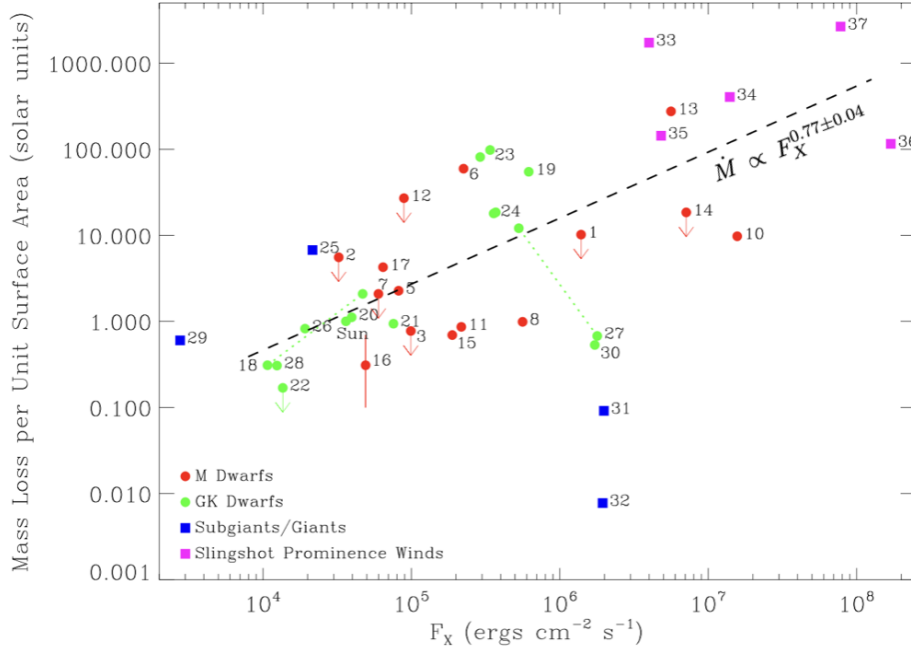


Figure 1.8: Mass-loss rates derived for low-mass stars as a function of X-ray flux. The circles and the blue squares are values derived with Ly- α observations. The red symbols are M dwarfs, the green G and K dwarfs and the blue are subgiants/giants stars. The magenta squares are values derived using prominences (Jardine & Collier Cameron, 2019). The red circle #16 was derived using the exoplanet as a probe of the stellar wind (Vidotto & Bourrier, 2017). The mass-loss rate is expressed in terms of solar wind units where $\dot{M}_{\odot} = 2 \times 10^{-14} M_{\odot} \text{ yr}^{-1}$. The dashed line is a power-law fit excluding the blue squares. Figure from Wood et al. (2021).

Mass-loss and coronal X-ray emission are both phenomena associated with the corona. \dot{M} is associated with a wind that originates from open field lines (coronal holes). On the other hand, F_X originates from close field lines (bright regions in X-ray and UV images). Overall, mass-loss increases with X-ray luminosity, $\dot{M} \propto F_X^{0.77}$, but with some scatter as seen in Fig. 1.8. This may indicate that coronal activity and spectral type are not enough to explain stellar wind properties (Wood et al., 2021).

1.2.2.2 What drives the wind of M dwarfs?

X-rays are usually used as a magnetic proxy (see Section 1.2.1) and the relation shown by Wood et al. (2021) suggests a link between mass-loss rate and X-ray flux (see Section 1.2.2.1), which means that mass-loss is also magnetic in nature. However, there is still no agreement about which physical mechanisms of magnetic nature are responsible for heating and accelerate the winds of cool dwarfs, and even in the case of the solar wind it remains an open question (e.g., Cranmer, 2009; Cranmer & Winebarger, 2019). The study of the solar wind is important to better understand other stellar winds. Some mechanisms have been suggested to explain how stellar winds of cool dwarfs are driven.

From solar observations, it is known that the corona has a higher temperature than the solar surface (photosphere). This temperature gradient can be described by a thermally-driven wind, in which the physical reason behind the temperature increase from the photosphere to the corona is not taken into consideration. Instead, it assumes the corona has already reached around a million-Kelvin temperature before the wind is launched. A thermally driven wind usually uses a polytropic index to indicate the relation between temperature (or thermal pressure) and density to describe the temperature profile. In the case of an index equal to one, the wind is isothermal or a Parker wind (Parker, 1958). An isothermal wind description is commonly adopted to study winds of cool dwarfs due to its “simplicity”. The only forces operating in the wind, in this case, are the gravity and the gradient of thermal pressure. A thermally-driven wind can include or not the effects of a magnetic field.

Another possibility is the use of MHD waves capable of naturally increasing the temperature from the photosphere to the corona and driving the outflowing stellar wind via the propagation of Alfvén waves. Magnetohydrodynamic (MHD) waves were first suggested as being associated with the presence of sunspots on the solar surface by Alfvén (1942). At this point, it was hypothesised that some type of MHD waves originating in the lower layers of the Sun was responsible for the photospheric activity observed. Only later were these MHD waves named after Hannes Alfvén. In 1949, Schatzman (1949) proposed that MHD waves could be the mechanism responsible for heating the solar corona to a higher temperature than the solar surface.

Alfvén waves propagate with an Alfvén velocity,

$$v_A = \frac{B}{\sqrt{4\pi\rho}}, \quad (1.2)$$

where B is the stellar wind magnetic field and ρ is the stellar wind density. Alfvén waves are generated by oscillations induced in the magnetic field lines at the base of the stellar wind. Fig. 1.9 presents a sketch of a stellar atmosphere where the open magnetic field lines oscillate and generate Alfvén waves. The stellar corona can be heated and accelerated by the dissipation of energy and momentum associated with the propagation of Alfvén waves, generating a stellar wind outflow (Hartmann & MacGregor, 1980; Vidotto & Jatenco-Pereira, 2006).

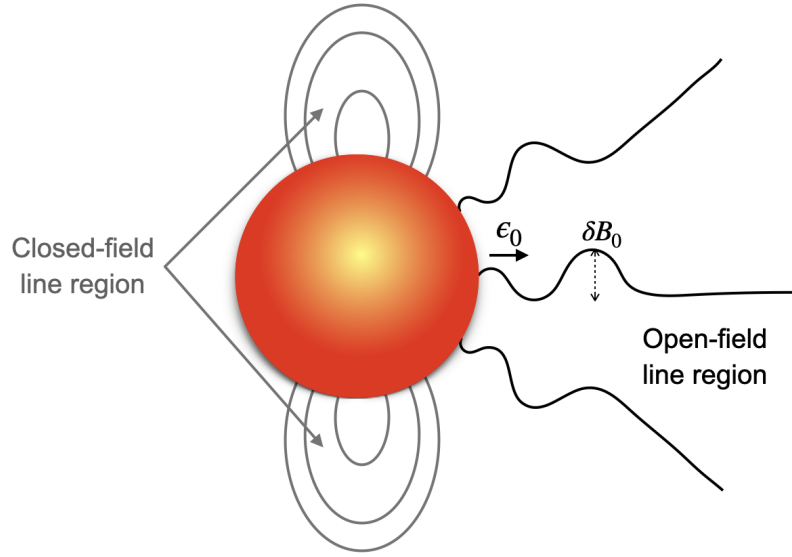


Figure 1.9: Schematic diagram of stellar atmosphere showing the closed and open magnetic field line regions. The open magnetic field lines oscillate in the form of Alfvén waves due to perturbations induced at the base of the wind. The amplitude of the wave depends on the magnetic field perturbation (δB_0) and the wave energy density at the base is given by ϵ_0 .

Alfvén waves can be used to describe outflows in the form of an Alfvén-wave-driven wind. This approach includes the effects of magnetic fields. In this type of stellar wind models, it is possible to derive the detailed structure of the wind energetics, such as cooling and heating, contrary to a Parker wind, which assumes a wind temperature a priori. In this thesis, I assume that the winds of M dwarfs are heated and accelerated by magnetic processes. To implement this process, I use a stellar wind model that considers the presence of Alfvén waves to heat and accelerate the winds of M dwarfs.

It is known that Alfvén waves can transport energy to contribute to the coronal heating, but it is still unclear how the wave energy is converted into thermal energy and if the energy from the waves is enough to heat up the solar corona (Pagano & De

Moortel, 2019; Prokopyszyn et al., 2019). Tomczyk et al. (2007) reported the detection of Alfvén waves in the solar corona, but they estimated that the energy carried out by the waves was not enough to heat the corona. Although this might not be the only mechanism, Alfvén waves are still believed to be one of the main contributors to explain the temperature gradient in the Sun’s atmosphere (e.g., Winebarger & Warren 2004; De Moortel & Browning 2015).

1.3 The interaction between the interstellar medium and the stellar wind

The solar wind interaction with the ISM creates a vast bubble-like shaped region around the Sun called the heliosphere. The region inside the heliosphere is dominated by the solar wind while the outside region is dominated by the interstellar wind. Similar to the solar wind, stellar wind interaction with the ISM also leads to the formation of an astrosphere. It is because of these interactions that stellar winds can be detected using Ly- α line observations (see Section 1.2.2.1).

Fig. 1.10 shows a sketch of a bubble-like shaped astrosphere. When the stellar wind starts to interact with the ISM, its velocity slows down. The region where the stellar wind properties start to change due to the interaction with the ISM is called the termination shock. The boundary where the ISM and stellar wind pressures are balanced is called the astropause. The pressure balance can be calculated as,

$$\begin{aligned} P_{\text{ram}} &= P_{\text{ISM}} \\ \frac{\dot{M}u_{\infty}}{4\pi R^2} &= m_p n_{\text{ISM}} \nu_{\text{ISM}}^2, \end{aligned} \quad (1.3)$$

where m_p is the proton mass, n_{ISM} is the total ISM number density of hydrogen and ν_{ISM} is the ISM velocity as observed by the star. P_{ram} can be expressed in terms of Equation (1.1) because at large distances, where the wind has reached its terminal velocity, the density of the wind falls with r^{-2} and P_{ram} follows the same trend.

Equation (1.3) allows us to calculate the extension of the astrosphere, R_{ast} , in terms of the stellar mass-loss rate, as

$$R_{\text{ast}} = \left(\frac{\dot{M}u_{\infty}}{4\pi m_p n_{\text{ISM}} \nu_{\text{ISM}}^2} \right)^{1/2}. \quad (1.4)$$

Thus, the astrospheric size is not only influenced by the stellar wind properties but also by the ISM properties, such as density, velocity and ionisation fraction. In addition,

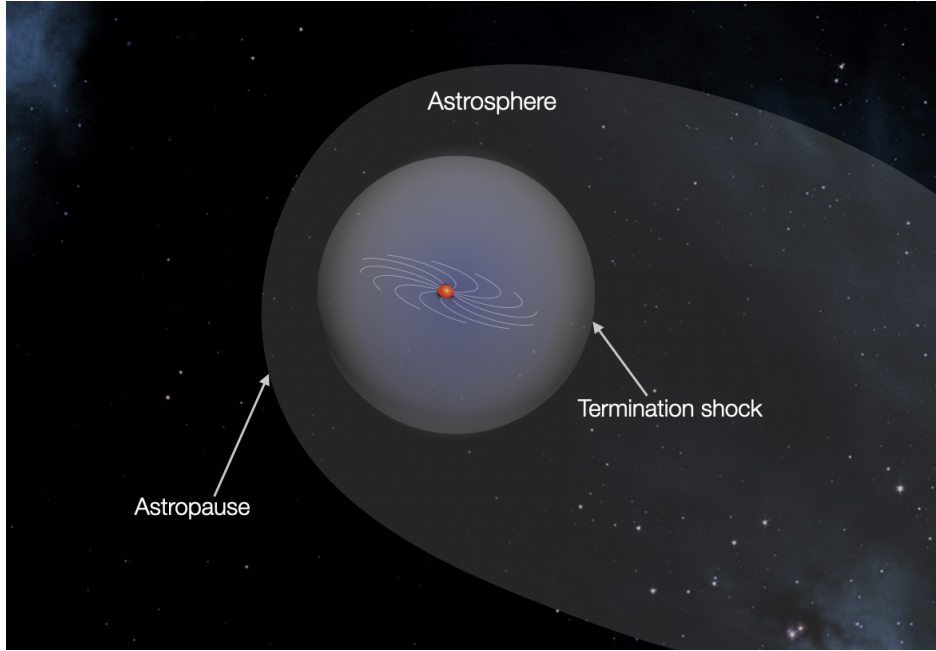


Figure 1.10: Schematic of an astrosphere shaped by the interaction between the ISM and the stellar wind. The termination shock is the region where the stellar wind properties start to change due to the interaction with the local ISM and the astropause.

the astrosphere can change in response to the Galactic environment around the star since the star moves through the ISM.

The heliosphere is located in the Local Interstellar Cloud (LIC) inside the Local Bubble. The LIC is the cloud immediately surrounding the Sun roughly 5-7 pc across (Redfield & Linsky, 2000) while the Local Bubble is the low density region within ~ 100 pc of the Sun. Fig. 1.11 shows the solar system within the LIC along with other stellar systems (blue dots) and stars with detected astrospheres (yellow bubble-like shape symbols).

Since the ISM can have different properties in different locations of the Galaxy, this change can directly impact the astrosphere size. Some works have investigated the astrosphere response under different ISM scenarios for both general astrospheres (Jasinski et al., 2020) and the heliosphere (Scherer et al., 2002, 2008; Müller et al., 2006). Müller et al. (2006) found that the extent (or size) of the heliosphere and structure can be vastly influenced by different ISM properties while assuming the same properties for the solar wind. In their model, the heliopause location was found to vary from 12 au, for an ISM $\sim 3\times$ denser and $\sim 4\times$ faster than contemporaneous values, to 402 au, for an ISM $\sim 3\times$ slower than contemporaneous values. Currently, the heliosphere extends to ~ 122 au as observed by *Voyager 1* (Stone et al., 2013, 2019).

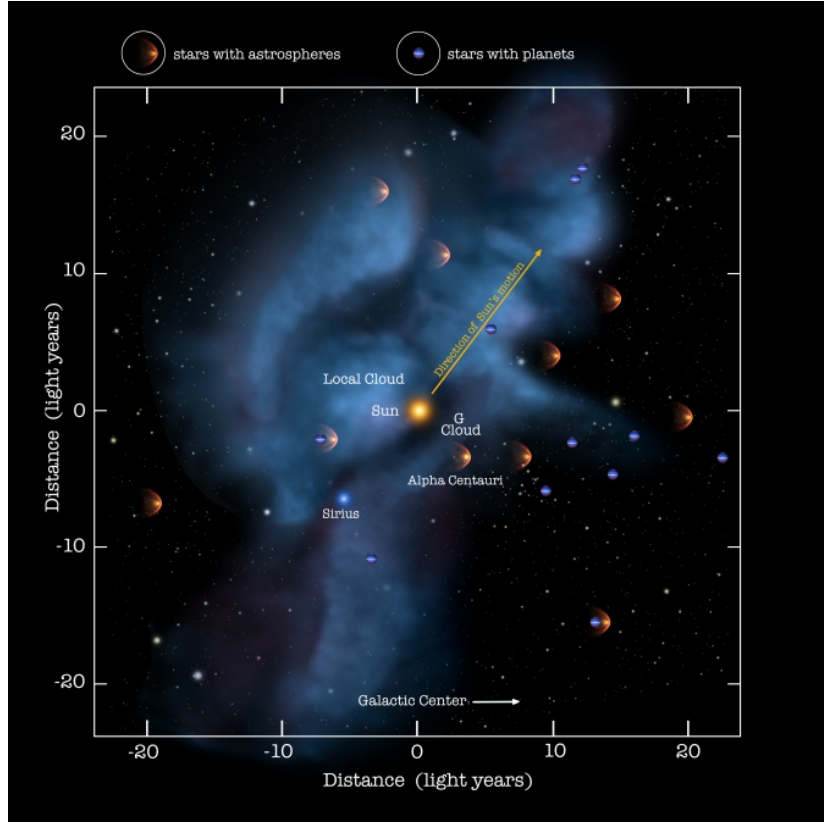


Figure 1.11: Local Interstellar Cloud structure. The solar system is shown in the center and its motion direction is shown by the yellow arrow. The yellow bubble-like shape symbols represent other detected astrospheres and the blue dots represent stars with known exoplanets. The direction of the Galactic Center is indicated by the white arrow. Image Credits: NASA/Adler/U. Chicago/Wesleyan.

On the other hand, Rodgers-Lee et al. (2020) investigated the heliosphere response due to changes in the solar wind for different ages of the solar system (while assuming the same properties for the ISM). They found that the heliopause distance decreased as the Sun aged varying from ~ 1530 to 47 au.

In terms of stars, astrosphere sizes can vary from a few au to 10^3 au (Herbst et al., 2020; Rodgers-Lee et al., 2021b; Mesquita et al., 2021, 2022a,b). Similar to the heliosphere, the astrosphere size can change as the star passes through different ISM regions and also when the star gets old and starts to be less active. All of these changes are especially important in the context of Galactic cosmic ray propagation inside stellar systems (see Section 1.4).

1.4 Galactic cosmic rays and stellar wind interaction

Cosmic rays are high-energy particles originating from the Sun (stellar cosmic rays), in our own Galaxy (Galactic cosmic rays), and outside our Galaxy (extra-galactic cosmic rays, Blasi, 2014). Galactic cosmic rays fill and are constantly present in the entire Galaxy. They mainly originate from, or are accelerated by, supernova remnant shocks formed in the ISM as the result of supernova explosions (Enomoto et al., 2002; Aharonian et al., 2004; Brose et al., 2020). It is assumed that cosmic rays with energy up to $\sim 10^{15}$ eV are from our own Galaxy, while the extra-galactic cosmic rays have much higher energy ($\sim 10^{18}$ eV) (Blasi, 2014). The origin of such high-energy cosmic rays is still unknown (Alves Batista et al., 2019). Stellar cosmic rays, also known as stellar energetic particles, originate in stellar events such as flares and coronal mass ejections (Rodgers-Lee et al., 2021b). Stellar cosmic ray typical energies can vary accordingly with stellar activity. For instance, during strong solar flares, the present-day Sun, an inactive star, can accelerate particles to $\sim 10^9$ eV energies (Ajello et al., 2014; Kafexhiu et al., 2018).

In this work, I will only focus on Galactic cosmic ray protons. Galactic cosmic rays can penetrate the astrosphere and reach planet magnetosphere/atmospheres. When interacting with planet atmospheres, cosmic rays can produce showers of secondary particles, which can reach the planet's surface. Fortunately, the magnetised stellar wind throughout the astrosphere acts as a barrier to Galactic cosmic ray fluxes. Outside the astrosphere, the Galactic cosmic ray has its background level (see Section 1.4.2), while inside the astrosphere it is modulated in an energy-dependent way. The modulation of cosmic rays can be explained as follows: to penetrate inside the astrosphere, Galactic cosmic rays need to overcome the outward flow of magnetised and turbulent stellar wind plasma. The magnetised stellar wind prevents low-energy cosmic rays from freely propagating into the inner astrosphere while high-energy cosmic rays are nearly unaffected (Parker, 1965; Potgieter, 2013).

When interacting with exoplanet atmospheres, cosmic rays can ionise molecules and lead to the production of prebiotic molecules (Dartnell, 2011; Rimmer et al., 2014; Airapetian et al., 2016; Barth et al., 2021). These prebiotic molecules are associated with the start of life. Thus, cosmic rays may have been associated with the emergence of life at Earth and possibly in other exoplanets (Airapetian et al., 2016; Atri, 2016). Many works have suggested cosmic rays can also affect Earth's climate through cloud coverage (Svensmark & Friis-Christensen, 1997; Shaviv, 2002, 2003; Kirkby et al., 2011; Svensmark et al., 2017).

Additionally, cosmic rays can also affect developed life-forms by causing cellular mutation (Dartnell, 2011) and damaging DNA in cells (Sridharan et al., 2016). The influence of cosmic rays on life-forms can be quantified by the planetary radiation dose (Atri, 2020; Atri et al., 2020). The planet’s surface is protected by the presence of an atmosphere and possibly a magnetosphere and the majority of cosmic rays do not reach the surface. It has been shown that magnetospheres (Grenfell et al., 2007; Grießmeier et al., 2009, 2015) and atmospheres (Grießmeier et al., 2016; Atri, 2020) can lessen cosmic ray fluxes at the planetary surface. In contrast, the lack of a planetary magnetic field can enhance cosmic ray intensities by more than three orders of magnitude (Grießmeier et al., 2015). The radiation dose on the planet’s surface can also be affected by the depth of the planet’s atmospheric column density (Atri et al., 2013; Atri, 2017). A larger atmospheric depth is effective at reducing the radiation dose at the planet’s surface (Atri, 2020). The radiation dose is therefore distributed further up in the atmosphere.

1.4.1 Galactic cosmic ray observations at Earth and correlation with solar activity

Cosmic rays fluxes are an important element in exoplanet habitability and quantifying their fluxes is essential (as described in Section 1.4). Galactic cosmic ray fluxes reaching Earth have been measured by different instruments at different times as shown in Fig. 1.12. The dotted line is representative of the unmodulated Galactic cosmic ray spectrum outside the heliosphere (see Section 1.4.2). The symbols indicate measurements made by different instruments. Red, yellow and blue symbols and shaded regions indicate approximately maximum, moderate and minimum solar activity regimes. The observations span over 40 years, and the differential intensity of cosmic rays varies by two orders of magnitude over the solar cycle. The cosmic ray intensity exhibits a link with the solar activity in which during solar minimum more cosmic rays are detected and during solar maximum cosmic rays are strongly suppressed.

The anti-correlation between the solar 11-year activity cycle and the intensity of Galactic cosmic rays at Earth is shown in Fig. 1.13. The top panel shows the percentage of cosmic rays observed at Earth in different epochs for particles with a cut-off momentum of 4.6 GeV/c. The values are normalised to 100% in March 1987. The bottom panel shows the yearly average sunspot number observed for five solar minimum activity periods (indicated by vertical lines). The heliospheric magnetic field polarity (A) epoch is also indicated at the top of Fig. 1.13. $A > 0$ indicates epochs in which

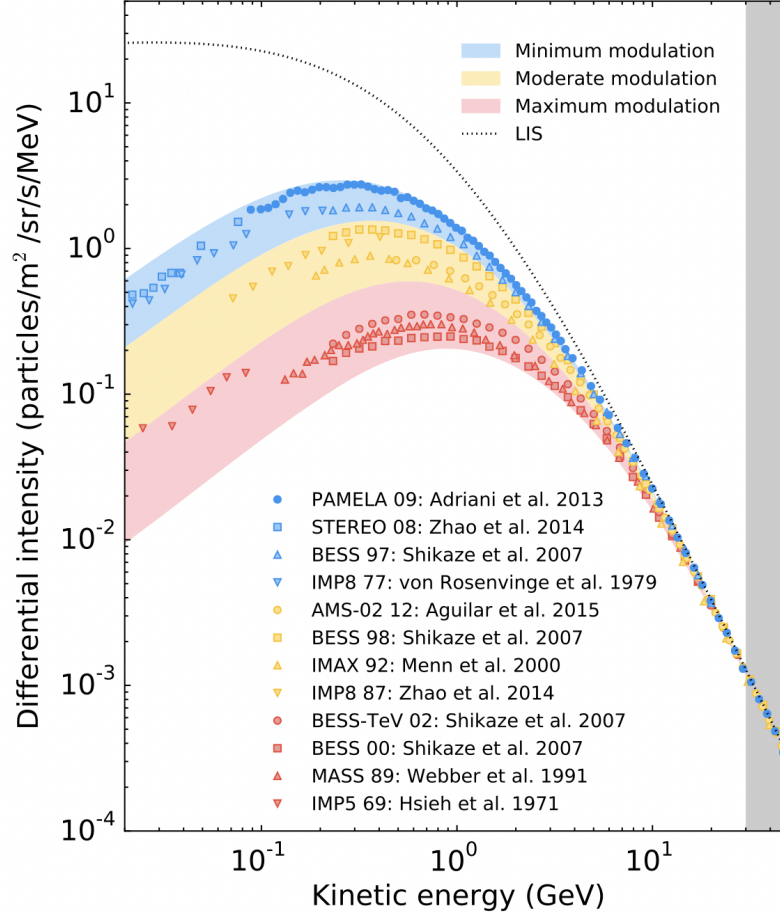


Figure 1.12: Galactic cosmic ray fluxes reaching Earth observed by different instruments throughout many years. Blue, yellow and red points are associated with minimum, moderate and maximum solar activity, respectively, which is anti-correlated with Galactic cosmic ray intensity. The dotted line is representative of the unmodulated Galactic cosmic ray spectrum. The grey shaded region indicates where suppression can be considered negligible. Figure from Vos & Potgieter (2015).

the solar magnetic field is pointed outward in the northern and inward in the southern polar region. Fig. 1.14 shows a schematic of these magnetic field polarity epoch configurations.

From Fig. 1.13 it is possible to observe that the magnetic field polarity epoch seems to affect the cosmic ray count. During solar minimum periods with $A < 0$ (solid and dashed lines), the cosmic ray count shows a sharp maximum while for periods with $A > 0$ (dotted and dash-dotted lines) an almost plateau is observed. This behaviour is attributed to particle drift effects (e.g, Strauss et al., 2012; Potgieter, 2013; Potgieter & Vos, 2017), a topic that will be discussed in Chapter 5.

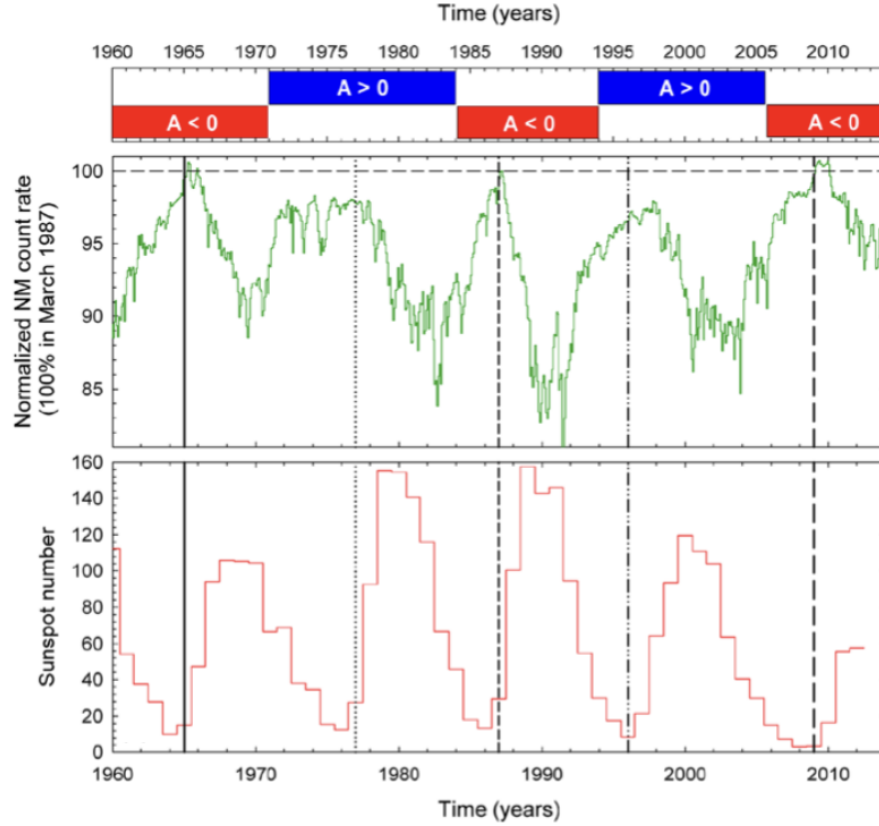


Figure 1.13: The top panel shows the solar modulation of cosmic rays observed by the Hermanus cosmic ray monitor in South Africa for a period of ~ 50 year, with counts normalised to 100% in March 1987. The bottom panel shows the yearly averaged sunspot number for the same period. The vertical lines indicate approximate times of solar minimum. The magnetic field polarity (A) is also indicated at the top. Figure from Strauss & Potgieter (2014).

1.4.2 The Local interstellar spectrum

Outside of the astrosphere, Galactic cosmic rays are not suppressed by the stellar outflow and have their background level. This background level is important because it sets the maximum flux of Galactic cosmic rays at the astropause boundary (assuming the star is not near a cosmic ray source). In August 2012, *Voyager 1* crossed the heliopause¹ and measured the cosmic ray intensity in the local ISM (Stone et al., 2013). These measurements are believed to be largely unaffected by the solar wind (Stone et al., 2013; Cummings et al., 2016) and represent the local interstellar spectrum (LIS) for cosmic rays with energy between 3 and 600 MeV. Vos & Potgieter (2015) developed

¹In 2012, *Voyager 1* crossed a region where it experienced a sharp drop in energetic heliospheric ions and an increase in low-energy Galactic cosmic rays protons, indicating it had crossed the heliopause (Stone et al., 2013).

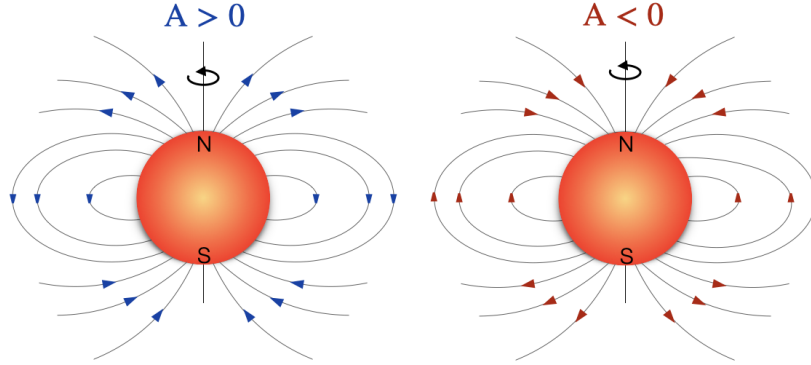


Figure 1.14: Schematic of the large-scale magnetic field polarity epochs. Magnetic field directed outward from the star in the northern polar region and inward in the southern polar region are known as $A > 0$, while $A < 0$ indicates the reverse magnetic field geometry.

a model fit, using the *Voyager 1* observations, to represent the cosmic ray differential intensities of the LIS, j_{LIS} ,

$$j_{\text{LIS}}(T) = 2.70 \frac{T^{1.12}}{\beta^2} \left(\frac{T + 0.67}{1.67} \right)^{-3.93} \text{ m}^{-2}\text{s}^{-1}\text{sr}^{-1}\text{MeV}^{-1}, \quad (1.5)$$

where T is the kinetic energy of the cosmic rays in GeV and $\beta = v/c$ is the particle speed as a fraction of the speed of light. Equation (1.5) represents the amount of Galactic cosmic rays at the heliopause at 122 au. Fig. 1.15 shows the *Voyager 1* observations of the LIS (green and yellow diamonds) and observations of cosmic rays at Earth using PAMELA (red circles) and AMS-02 (blue circles). Galactic cosmic rays with energies above 30–50 GeV are virtually unsuppressed by the solar wind (e.g., Potgieter, 2013; Vos & Potgieter, 2015) and measurements at Earth can be used to further constrain the LIS at this energy range. The model fit to the LIS is shown in Fig. 1.15 by the black line.

Unfortunately, in-situ measurements of Galactic cosmic ray fluxes in locations other than the solar system are not available. However, Galactic cosmic rays, with GeV energy, can be indirectly detected by observing γ -ray emission. As cosmic rays travel in the Galaxy, they interact with matter, and this interaction generates γ -ray emission. Many works have used γ -ray observations of nearby molecular clouds to infer the cosmic ray intensities in other locations in the Galaxy (Neronov et al., 2017; Aharonian et al., 2020; Baghmanyant et al., 2020) and it was found that γ -ray observations, with energy $\sim 10 - 10^4$ GeV, across a region of 1 kpc in the local Galaxy are consistent with the LIS measurements (Neronov et al., 2017). Some local variations in the cosmic ray spectrum

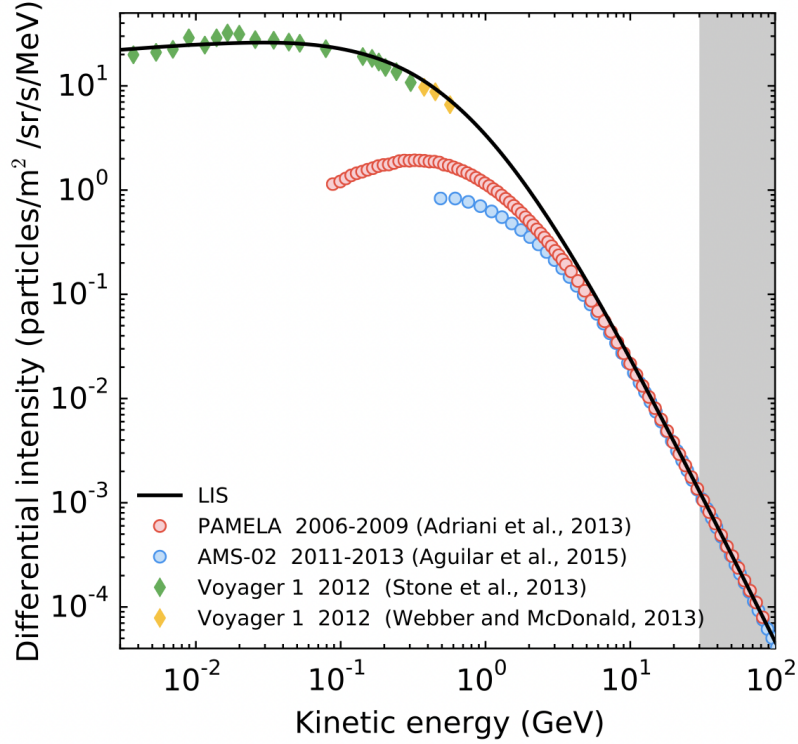


Figure 1.15: Differential intensity of Galactic cosmic rays as a function of kinetic energy. The diamond points are observations by *Voyager 1* while it is orbiting outside the heliosphere. The circles are observations at Earth made by PAMELA (red circles) and AMS-02 (blue circles). The black line is a model fit to the observations representative of the unmodulated cosmic ray outside the heliosphere, known as the LIS. Figure from Vos & Potgieter (2015).

are expected in the Galactic disk (Baghmanyant et al., 2020), mainly near acceleration regions, which can show a local increase in the cosmic ray flux (Fatuzzo et al., 2006). This allows us to use LIS observations outside the heliosphere to describe the Galactic cosmic ray spectrum outside other astrospheres if they are not near any cosmic ray accelerator region.

1.4.3 How to infer/detect cosmic rays on other planets

To understand the effect of cosmic rays on exoplanet habitability it is necessary to estimate their intensities at the planet’s magnetosphere, atmosphere, and/or surface. Cosmic ray transport models are currently the only approach to quantify the intensity of Galactic cosmic rays reaching exoplanets (e.g., Sadovskii et al., 2018; Herbst et al., 2020; Mesquita et al., 2021; Rodgers-Lee et al., 2021b; Mesquita et al., 2022a,b) and the Earth focusing on different ages of the solar system (e.g., Scherer et al., 2002, 2008;

Müller et al., 2006; Svensmark, 2006; Cohen et al., 2012; Rodgers-Lee et al., 2020). Many works have used cosmic ray models to understand the fluxes observed at Earth (e.g., Potgieter, 2013; Strauss et al., 2012; Strauss & Potgieter, 2014; Potgieter et al., 2015a). Similarly, models have also been used to understand the effects of stellar cosmic rays in exoplanet’s atmospheres (Segura et al., 2010; Grenfell et al., 2012; Tabataba-Vakili et al., 2016; Scheucher et al., 2020) and in M dwarf habitable zone (Fraschetti et al., 2019).

Cosmic rays are a source of ionisation in exoplanet atmospheres and some fingerprint ions, such as H_3O^+ , H_3^+ and NH_4^+ (Helling & Rimmer, 2019; Barth et al., 2021) have been identified as good indicators of the presence of cosmic rays (both Galactic and stellar counterparts) in exoplanet atmospheres. Absorption features in the transmission spectra of gas giant exoplanet atmospheres caused by the presence of these fingerprint ions may be observable with future observations with JWST (Gardner et al., 2006) and ARIEL (Tinetti et al., 2021). These observations could help constrain the cosmic ray fluxes reaching exoplanet atmospheres and give some constraints for simulations. Additionally, these observations could also help us to further piece together the habitability “puzzle”.

1.5 This thesis

This thesis is about modelling the Galactic cosmic ray propagation through the winds of M dwarfs with an emphasis on modelling cosmic ray fluxes at the planet’s orbit and the habitable zone. An outline of this thesis is presented next.

Chapter 2: Trends in stellar wind properties of M dwarfs

This chapter focuses on a parametric study of the winds of M dwarfs aiming to understand the general trends in the wind properties, such as the mass-loss rates, velocities, and temperatures. A 1D MHD Alfvén-wave driven stellar wind model was used to describe the stellar wind outflow. The input parameters are explored by varying the magnetic field strength and the wind density at the wind base, in this case at the chromosphere.

It is demonstrated that the temperature of our winds, driven by the presence of Alfvén waves, quickly reach an isothermal stage with mass-loss rates proportional to the wind base density, $\dot{M} \propto \rho_0^2$. Additionally, a comparison between our models and an isothermal wind model (Parker wind) is presented. It is shown that models with denser winds have terminal velocities and mass-loss rates values consistent with a Parker wind.

More rarefied winds, on the other hand, have their terminal velocities and mass-loss rate underestimated by a Parker wind. This implies that denser winds can be well described by simplified isothermal wind models.

Finally, using our wind models, the X-ray luminosity of the M dwarf GJ 436 was calculated by assuming that the luminosity is proportional to the radiative losses in the chromosphere. By comparing with observed X-ray luminosity, the mass-loss rate of GJ 436 was constrained to be $\dot{M} < 7.6 \times 10^{-15} M_{\odot} \text{ yr}^{-1}$. This value is compared with other models for the same star using different approaches.

This chapter was published in Monthly Notices as Mesquita & Vidotto (2020), 494, 1297–1307.

Chapter 3: The terrestrial Galactic cosmic ray flux in the habitable zone of GJ 436

This chapter explores the propagation of Galactic cosmic rays in the planetary system GJ 436. The flux of cosmic rays reaching different distances in GJ 436’s astrosphere was quantified by using a 1D cosmic ray transport model. Because the stellar wind properties of GJ 436 are not well constrained, two stellar wind models from Chapter 2 were used, one with a mass-loss rate consistent with X-ray luminosity observations and another one with a higher mass-loss rate (by 2 orders of magnitude). However, the two stellar wind regimes have similar magnetic field and velocity profiles.

Although the astrosphere size calculated for each regime was different, one ten times larger than the other, the Galactic cosmic ray fluxes at the habitable zone and at GJ 436 b were found to be similar for both wind regimes. In addition, the flux at the habitable zone was found to be comparable with the intensities observed on Earth. However, because GJ 436 b has a close-in orbit the cosmic ray flux reaching the exoplanet was calculated to be ~ 10000 times smaller than observed values at Earth for cosmic rays with energy $\lesssim 3 \times 10^{-2} \text{ GeV}$.

This chapter was published in Monthly Notices as Mesquita et al. (2021), 505, 1817–1826.

Chapter 4: Galactic cosmic ray fluxes in M dwarf with known exoplanets

This chapter expands the study of Galactic cosmic ray propagation in five M dwarf astrospheres (GJ 15A, GJ 273, GJ 338B, GJ 411, and GJ 887). These stars were chosen because they have at least one detected exoplanet and their wind mass-loss rates are

constrained by Lyman- α observations. To determine a stellar wind with properties constrained by observations a 1D MHD Alfvén-wave-driven stellar wind model was used (previously used in Chapter 2). For the Galactic cosmic ray propagation, a 1D cosmic ray transport model was used (previously used in Chapter 3).

The habitable zone of GJ 411 and GJ 887 was found to receive comparable Galactic cosmic ray fluxes with Earth’s value, while in GJ 15A, GJ 273, and GJ 338B the fluxes are lower. The Galactic cosmic ray fluxes received by almost all the planets in the sample are significantly lower than Earth’s values as the planets have a close-in orbit. The exceptions are GJ 15A c, which has a slightly higher flux than Earth, and GJ 411 c, which receives Galactic cosmic ray fluxes similar to the LIS.

Finally, the radiation dose received at the surface was calculated for the only habitable-zone planet in the sample, GJ 273 b. By assuming an Earth-like atmosphere and no magnetic field, it was found that GJ 273 b receives a radiation dose equivalent to 40% of the annual dose on Earth’s surface. This radiation dose is quite significant since GJ 273 b receives only ~ 2.3 times less GeV cosmic rays than Earth.

This chapter was published in Monthly Notices as Mesquita et al. (2022a), 509, 2091–2101.

Chapter 5: The effect of particle drift on Galactic cosmic ray propagation in M dwarf systems

In this chapter, the effect of particle drift is studied. Particle drifts are caused by gradients and curvatures in the stellar magnetic field that was incorporated in the Galactic cosmic ray propagation model. The study is focused on two M dwarfs: Prox Cen, the closest star in the solar neighbourhood, and AU Mic, a very young and active star. Both stars have known exoplanets, and in particular, Prox Cen b orbits in the habitable zone.

Particle drift was shown to affect the cosmic ray spectrum in M dwarf systems. In the case of Prox Cen and AU Mic, the inclusion of particle drift increased the intensity of Galactic cosmic rays in the astrosphere when compared with models without particle drift. This effect is more relevant for Prox Cen. Since the stellar wind properties of AU Mic are not well constrained, two wind environments were used (a high and a low stellar wind mass-loss rate). Both wind scenarios show a strong suppression of cosmic rays but they do not show similar modulation for the same distance. Galactic cosmic ray fluxes reaching Prox Cen b, AU Mic b and AU Mic c are strongly suppressed and, compared with Earth their fluxes are much smaller.

This chapter was published in *Monthly Notices* as Mesquita et al. (2022b), 515, 1218–1227.

1.6 Outlook

In this work, we have mainly used 1D stellar wind simulations and 1D cosmic ray transport models. 3D cosmic ray models are commonly used to describe cosmic ray transport in the heliosphere and to quantify the intensities at Earth (e.g., Potgieter, 2013). These models can help to understand the observations of Galactic cosmic rays at Earth and their effects. For this reason, a natural future step is to implement a 2D/3D model to better describe the 3D nature of the cosmic ray transport within other astrospheres. Since particle drifts seem to affect cosmic ray transport, the 3D cosmic ray models will further allow the inclusion of the three components of particle drift. 3D MHD simulations of stellar winds would also better characterise the system.

Stellar cosmic ray effects have been neglected in this work, however, it is expected that stellar cosmic ray fluxes dominate over Galactic cosmic rays up to a certain energy. This may be especially relevant for young and active stars which can accelerate stellar cosmic rays during flares and coronal mass ejections (Rodgers-Lee et al., 2021a). For this reason, the contribution of stellar cosmic rays should also be quantified for the M dwarfs studied here. In addition, Barth et al. (2021) showed that apart from fingerprints, stellar cosmic rays can also strongly enhance the abundance of organic molecules, such as formaldehyde (CH_2O) and ethylene (C_2H_2) which are both precursors to the production of glycine ($\text{C}_2\text{H}_5\text{NO}_2$). Glycine is one of the amino acids associated with the origin of life, originally produced in the Miller-Urey experiment (Miller, 1953). In particular, ethylene was enhanced to values possibly observable by spectroscopic atmosphere observations with JWST. Additionally, to interpret spectroscopic observations information from both cosmic ray fluxes (Galactic and stellar) will be needed.

Finally, Trappist-1 is a fascinating system with four habitable-zone planets in a total of seven planets. With so many possible habitable planets in a single system, it would be interesting to estimate the fluxes of Galactic and stellar cosmic rays reaching those exoplanets.

1.6 Outlook

Global trends in winds of M dwarf stars

Amanda L. Mesquita, & Aline A. Vidotto.
2020, MNRAS, 494, 1297–1307

Abstract

M dwarf stars are currently the main targets in searches for potentially habitable planets. However, their winds have been suggested to be harmful to planetary atmospheres. Here, in order to better understand the winds of M dwarfs and also infer their physical properties, we perform a one-dimensional magnetohydrodynamic parametric study of winds of M dwarfs that are heated by dissipation of Alfvén waves. These waves are triggered by sub-surface convective motions and propagate along magnetic field lines. Here, we vary the magnetic field strength B_0 and density ρ_0 at the wind base (chromosphere), while keeping the same relative wave amplitude ($0.1B_0$) and dissipation lengthscale. Our simulations thus range from low plasma- β to high plasma- β (0.005 to 3.7). We find that our winds very quickly reach isothermal temperatures with mass-loss rates $\dot{M} \propto \rho_0^2$. We compare our results with Parker wind models and find that, in the high- β regime, both models agree. However, in the low- β regime, the Parker wind underestimates the terminal velocity by around one order of magnitude and \dot{M} by several orders of magnitude. We also find that M dwarfs could have chromospheres extending to 18% to 180% of the stellar radius. We apply our model to the planet-hosting star GJ 436 and find, from X-ray observational constraints, $\dot{M} < 7.6 \times 10^{-15} M_\odot \text{ yr}^{-1}$. This is in agreement with values derived from the Lyman- α transit of GJ 436b, indicating that spectroscopic planetary transits could be used as a way to study stellar wind properties.

2.1 Introduction

M dwarf stars are the most common type of stars in our Galaxy. They are small, main-sequence stars with masses smaller than $\sim 0.5M_\odot$, low surface temperatures and low

2.1 Introduction

brightness. One of the most interesting features in M dwarfs is their close-in habitable zone, which is defined as the extended area away from the star where an orbiting planet could have liquid water on its surface (Kasting et al., 1993; Selsis et al., 2007). Because M dwarf stars have low luminosities, their habitable zones are much closer in, which makes it easier to observe exoplanets in their habitable zones due to current biases in planet detection. For a M dwarf with $0.5 M_{\odot}$, for example, the habitable zone is at $\sim 0.2 - 0.4$ astronomical units (Kasting et al., 1993; Selsis et al., 2007). However, one potential issue for planet habitability is that main-sequence M dwarfs remain active for a long fraction of their lives, generating strong kG magnetic fields (Morin et al., 2010; Lang et al., 2014; See et al., 2019; Shulyak et al., 2019). A star with strong activity can generate strong flares, winds and coronal mass ejections, which can affect the exoplanets orbiting their habitable zones as well as exoplanet habitability (Khodachenko et al., 2007; Vida et al., 2017; Tilley et al., 2019).

In addition to consequences to planetary habitability, stellar winds play an essential role in stellar evolution (Matt et al., 2015; Johnstone et al., 2015). However, M dwarfs, similar to other cool dwarf stars, have rarefied winds and, as a consequence, it is difficult to directly measure them (Wood, 2004; Vidotto & Bourrier, 2017; Jardine & Collier Cameron, 2019). There are some techniques developed to infer the mass-loss rates of cool dwarf stars, such as radio emission analysis (Panagia & Felli, 1975; Lim & White, 1996; Fichtinger et al., 2017; Vidotto & Donati, 2017), or the identification of X-ray emission generated due to the interaction between ionized wind particles with neutral atoms from the interstellar medium (Wargelin & Drake, 2002; Jardine & Collier Cameron, 2019). Another more successful method used to detect stellar winds is related to the study of stellar Ly- α line absorption when the stellar wind exchange charges with a neutral or partially neutral interstellar medium (Wood et al., 2002, 2005). By studying Ly- α observations of the binary system α Centauri (G2 + K0) and its distant companion star Proxima Centauri (M5.5), Wood et al. (2001) predicted a mass-loss rate upper limit of $\dot{M} < 4 \times 10^{-15} M_{\odot} \text{ yr}^{-1}$ for Proxima Centauri. A recently proposed method is to use the exoplanet atmosphere interaction with the host star wind to infer some properties of the local stellar wind (Vidotto & Bourrier, 2017). These techniques have provided some constraints on the winds of M dwarfs, but still a full picture does not yet exist.

In the present work, we turn to numerical simulations to investigate stellar winds of M dwarfs. There are still not many numerical studies dedicated to the winds of M dwarfs (e.g. Vidotto et al., 2014a; Garraffo et al., 2016; Vidotto & Bourrier, 2017). In cool dwarfs, it is common to study winds by adopting a Parker wind model (Parker,

1958), which consists of a stellar wind with constant temperature. One weakness of isothermal winds is that, by assuming that the temperature is constant, we cannot derive the detailed structure of the wind energetics, such as, heating and cooling. In our work, we assume that the winds of M dwarfs are heated by magnetic processes, similar to the solar wind. For that, we use a model that considers the presence of Alfvén-waves to drive the winds of M dwarfs. With this, we can better investigate the physical processes of the wind acceleration mechanism and of its heating.

Alfvén waves are magnetohydrodynamic (MHD) waves that propagate with an Alfvén velocity $v_A = B/\sqrt{4\pi\rho}$, where B is the magnetic field and ρ is the density. In 1942, Alfvén (1942) hypothesized that MHD waves generated in the lower layers of the Sun could be associated with sunspots. Later on, Schatzman (1949) proposed that MHD waves were responsible by the coronal heating. Alfvén waves are still one of the hypothesis to explain the temperature gradient in the Sun’s atmosphere (e.g., Winebarger & Warren 2004; De Moortel & Browning 2015). Alfvén waves are generated if oscillations are induced at the magnetic field at the base of the wind. The dissipation of energy and momentum associated with the wave propagation can lead to the acceleration of the outer atmosphere in the form of an Alfvén-wave driven wind (Hartmann & MacGregor, 1980; Vidotto & Jatenco-Pereira, 2006).

In this paper, we perform a parametric study of winds of M dwarf stars, using an Alfvén-wave driven stellar wind model to understand the winds of M dwarfs and also infer their properties, like mass-loss rates, velocities, etc. This paper consists of the following sections. In Section 2.2, we describe our stellar wind model and the simulation parameters. Our results for the wind structure and general trends of M dwarfs are presented in Section 2.3, followed by a discussion about the chromospheric size of M dwarfs and an application to the planet-hosting star GJ 436 in Section 2.4. Finally, we present a comparison with a Parker wind model and a discussion about the effects of the free input parameters in our simulation in Section 2.5 followed by conclusions in Section 2.6.

2.2 Alfvén-wave driven stellar wind model

We perform one dimensional magnetohydrodynamic simulations to heat and drive the wind of M dwarf stars. Alfvén waves are generated by perturbations induced in the magnetic field at the base of the wind. The waves accelerate the stellar atmosphere in the form of an Alfvén-wave driven wind (Hartmann & MacGregor, 1980; Holzer et al.,

2.2 Alfvén-wave driven stellar wind model

1983; MacGregor & Charbonneau, 1994). The model used in this work is based on Vidotto & Jatenco-Pereira (2010), and we describe it next.

We numerically solve the time-independent MHD equations including momentum and energy equations:

$$u \frac{du}{dr} = -\frac{GM_\star}{r^2} - \frac{1}{\rho} \frac{dP}{dr} - \frac{1}{2\rho} \frac{d\epsilon}{dr}, \quad (2.1)$$

$$\rho u \frac{d}{dr} \left(\frac{u^2}{2} + \frac{5}{2} \frac{k_B T}{m} - \frac{GM_\star}{r} \right) + \rho u \frac{d}{dr} \left(\frac{F_c}{\rho u} \right) + \frac{u}{2} \frac{d\epsilon}{dr} = Q - P_r, \quad (2.2)$$

where u is the wind velocity, r the radial coordinate, G the gravitational constant, M_\star the stellar mass, $P = \rho k_B T / m$ the gas pressure, m the average mass of the wind particles, ρ the wind density, T the wind temperature, ϵ the energy density of the Alfvén waves, F_c the thermal conduction, Q the volumetric heating rate and P_r is the volumetric radiative cooling rate.

The terms on the right-hand side of Equation (2.1) are the gravitational force, the gradient of the thermal pressure and the gradient of the wave pressure, respectively. The first, second and third terms on the left-hand side of Equation (2.2) are related to the wind energy (kinetic energy, enthalpy and gravitational energy), the thermal conductivity and the rate at which the waves do work, respectively. The terms on the right-hand side of Equation (2.2) are related to the wave heating and the radiative cooling.

The energy density of the Alfvén waves (Hartmann & MacGregor, 1980) are given by:

$$\epsilon = \epsilon_0 \frac{M_0}{M} \left(\frac{1 + M_0}{1 + M} \right) \exp \left[- \int_{r_0}^r \frac{1}{L} dr \right], \quad (2.3)$$

where M is the Mach number and L is the damping length. In this paper, whenever we use the subscript “0”, it represents a quantity calculated at the base of the wind, thus, in Equation (2.3), M_0 is the Mach number at the wind base at $r = r_0$. Here, we assume the nonlinear damping mechanism for the waves, as this has been used in some solar wind models (Suzuki & Inutsuka, 2005; Suzuki et al., 2013). We parametrise the non-linear damping mechanism, following the work of Jatenco-Pereira & Opher (1989), by

$$L = L_0 \left(\frac{v_A}{v_{A0}} \right)^4 \frac{\langle \delta v_0^2 \rangle}{\langle \delta v^2 \rangle} (1 + M), \quad (2.4)$$

with an initial length of 10% of stellar radius ($L_0 = 0.1r_0$). Here, $\langle \delta v^2 \rangle$ is the mean quadratic amplitude of the fluctuations in the wave velocity. The amplitude of the velocity fluctuations are connected with the amplitude of magnetic field fluctuations

by energy equipartition

$$\frac{1}{2}\rho\langle\delta v^2\rangle = \frac{\langle\delta B^2\rangle}{8\pi}. \quad (2.5)$$

Finally, the energy density of the wave is related to its flux as

$$\phi_A = \epsilon v_A \left(1 + \frac{3}{2}M\right). \quad (2.6)$$

The thermal conduction flux is

$$F_c = -\kappa T^{5/2} \frac{dT}{dr}, \quad (2.7)$$

where $\kappa = 10^{-6} \text{ erg cm}^{-1} \text{ s}^{-1} \text{ K}^{-1}$ is the Spitzer conductivity. The volumetric heating rate caused by wave dissipation is

$$Q = \frac{\epsilon}{L}(u + v_A), \quad (2.8)$$

and the volumetric radiative cooling rate is

$$P_r = \Lambda n_e n_H, \quad (2.9)$$

where Λ is the cooling function which depends on the metallicity, n_e is the electron density and n_H is the total hydrogen density. In our simulations, we adopt the cooling function from Schure et al. (2009) for solar-like metallicity. Given the high temperatures our winds achieve, our winds are fully ionised through the simulation domain, which implies that $n_H = n_p = n_e$, where n_p is the proton density.

We also numerically solve the mass conservation equation, assuming steady state

$$\frac{d}{dr}(\rho u r^2) = 0. \quad (2.10)$$

We initially perform 134 simulations assuming spherical symmetry with the input parameters presented in Table 2.1. We use the values of mass and radius for an early M dwarf, similar to GJ 436. We adopt an open magnetic field line configuration with magnetic field oscillations induced at the base of the chromosphere. The initial perturbations in the magnetic field lines were set to be 10% of magnetic field, $\sqrt{\langle\delta B_0^2\rangle} = 0.1B_0$. Given our values of input magnetic fields our simulations are more appropriate for an inactive to moderately active star. Our simulations results in wave fluxes ranging from 7.9×10^2 to $1.64 \times 10^6 \text{ erg cm}^{-2} \text{ s}^{-1}$ at the base of the chromosphere.

To solve the set of coupled differential equations, we use a shooting method, in which the only physical solution is the one that passes through the Alfvén point (e.g. Vidotto

2.3 Parametric study of winds of M-dwarfs

Table 2.1: The top part of the table shows the input parameters of our simulations, assumed at the base of the wind (chromosphere). The parameters at the bottom, below the line, are derived from the input parameters.

Physical parameter	Symbol	Value	Unit
Stellar mass	M_\star	0.452	M_\odot
Stellar radius	r_0	0.437	R_\odot
Temperature	T_0	2×10^4	K
Magnetic field	B_0	1 – 10	G
Density	ρ_0	$(1 - 90) \times 10^{-15}$	g cm^{-3}
Magnetic field perturbation	$\sqrt{\langle \delta B_0^2 \rangle}$	0.1	B_0
Damping length	L_0	0.1	r_0
Wave amplitude	$\sqrt{\langle \delta v_0^2 \rangle}$	0.9 – 25.4	km s^{-1}
Wave flux	ϕ_{A0}	$7.9 \times 10^2 - 1.64 \times 10^6$	$\text{erg cm}^{-2} \text{s}^{-1}$
Wave energy density	ϵ_0	$(7.9 - 790) \times 10^{-4}$	erg cm^{-3}
plasma β at base	β	0.005 – 3.7	

& Jatenco-Pereira, 2006). The Alfvén point is the point where the wind velocity is equal to Alfvén velocity, i.e., the distance where the Mach number is unit ($M = u/v_A = 1$). This is an important parameter for calculating the angular momentum-loss rate, which we will discuss in Section 2.3.2 (Weber & Davis, 1967; Kraft, 1967).

2.3 Parametric study of winds of M-dwarfs

2.3.1 The structure of the wind

To understand the wind properties, we analyze how temperature, velocity and density profiles are affected by different input parameters. Fig. 2.1 shows wind profiles for different magnetic field intensities and for two ranges of base density. We separate the base densities in two ranges that we label as ‘low- β ’ for $\rho_0 = (1 - 9) \times 10^{-15} \text{ g cm}^{-3}$ and ‘high- β ’ for $\rho_0 = (1 - 9) \times 10^{-14} \text{ g cm}^{-3}$. The plasma β parameter gives information about the balance between the gas pressure and the magnetic pressure and is given by:

$$\beta = \frac{P}{P_{\text{mag}}} = \frac{8\pi\rho k_B T}{mB^2}, \quad (2.11)$$

where $P_{\text{mag}} = B^2/8\pi$ is the magnetic pressure.

We see an overall higher wind temperature (Fig. 2.1-a) for higher base densities (high- β), and, to a lesser extent, higher temperatures are also seen with higher base magnetic fields. However, the magnetic field does not affect significantly the temperature profiles for high- β , which is seen in the similarities of all distance-profiles. The

temperature profile displays a sudden rise before $\sim 1.5 r_0$ and then reaches a flat profile. This flat profile is caused by conduction – models of red supergiant winds without conductive fluxes, for example, do not show this (Vidotto & Jatenco-Pereira, 2006). The plateau profile can be interpreted as M dwarfs having nearly isothermal winds. We will come back to this in Section 2.5.1, when we compare our results with Parker winds, and the trends with plasma β are discussed in Section 2.3.2.

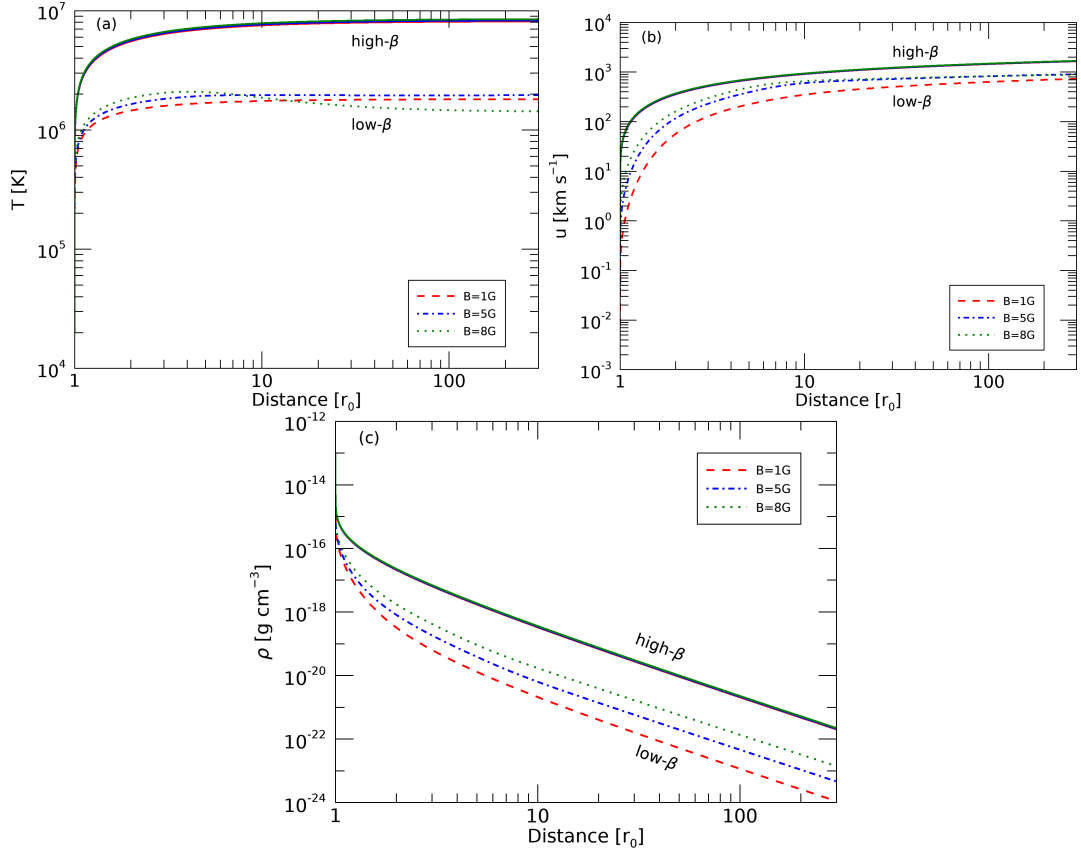


Figure 2.1: Temperature, velocity and density profiles for high- β (solid lines) and low- β (non-solid lines) ranges and magnetic fields 1 (red), 5 (blue) and 8 G (green). The profiles for high- β do not depend significantly on the magnetic field intensity. This is because these winds are thermally dominated. We use $\rho_0 = 9 \times 10^{-15}$ g cm $^{-3}$ for low- β cases and $\rho_0 = 9 \times 10^{-14}$ g cm $^{-3}$ for high- β cases.

The overall velocity profiles (Fig. 2.1-b) are higher for high magnetic field intensities. These profiles show two different behaviours with β parameter. For all our wind models, the terminal velocities vary from around 710 to 3100 km s $^{-1}$. The wind is rapidly accelerated by the transfer of momentum from the waves to the plasma (a consequence of the third term in Equation (2.1)) and then reaches an asymptotic profile. The acceleration process happens closer to the star for high- β cases. For low- β , the velocity

2.3 Parametric study of winds of M-dwarfs

decreases with base density and for high- β the velocity increases with base density. The velocity profile for high- β is not significantly affected by the magnetic field intensity.

The overall density profiles (Fig. 2.1-c) are higher for higher magnetic field intensities and base densities. Further away from the star, the wind is orders of magnitude less dense than at the base, which demonstrates that winds of M dwarfs can be very rarefied, like the solar wind. Similarly to the other profiles studied here, the density profile for high- β is not significantly affected by the intensity of the base magnetic field. At large distances, the density profile falls with r^2 as a consequence of mass conservation (Equation (2.10)) and the asymptotic wind speed. At small distances, the nearly exponential decrease in density is due to the rapid increase observed in the velocity profile.

All profiles show a very clear trend according to base density range. The physical explanation for it lies on the β parameter. Beta smaller than one ($\beta < 1$) indicates that magnetic field plays a major role in the wind and beta greater than one ($\beta > 1$) indicates that the thermal forces dominate. In our simulations, we do not change the temperature at the base, which means that the only parameters influencing β at the base are the base density and magnetic field intensity. Therefore by analyzing the beta profile we can interpret what is happening in our simulations for different input parameters.

Fig. 2.2 shows some selected β profiles for $B_0 = 5$ G and $\rho_0 = 5, 9, 50$ and $90 \times 10^{-15} \text{ g cm}^{-3}$. In this plot, we see that smaller base densities (5 and $9 \times 10^{-15} \text{ g cm}^{-3}$) have $\beta < 1$ for nearly the whole wind. The wind only reaches $\beta > 1$ for $r > 100 r_0$. For higher base densities (50 and $90 \times 10^{-15} \text{ g cm}^{-3}$), $\beta < 1$ only for distances smaller than $10 r_0$. These different profiles are due to a combination of different densities, temperature and magnetic field throughout the wind (see Fig. 2.1). These trends in the beta profiles demonstrate that low base density cases (low- β) are more magnetically dominated (magnetic field plays a major role in the wind) and high base density cases (high- β) are more thermally dominated (winds are thermally driven). This explains why temperature, velocity and density profiles for high- β are not particularly affected by changes in magnetic field intensities.

2.3.2 Global trends of M dwarf winds

Here, we investigate the overall trends found in our simulations. To extract the global quantities of the wind, we use the fact that the values for temperature and velocity are nearly constant at large distance ($\gtrsim 50 r_0$). We group simulations of same base density

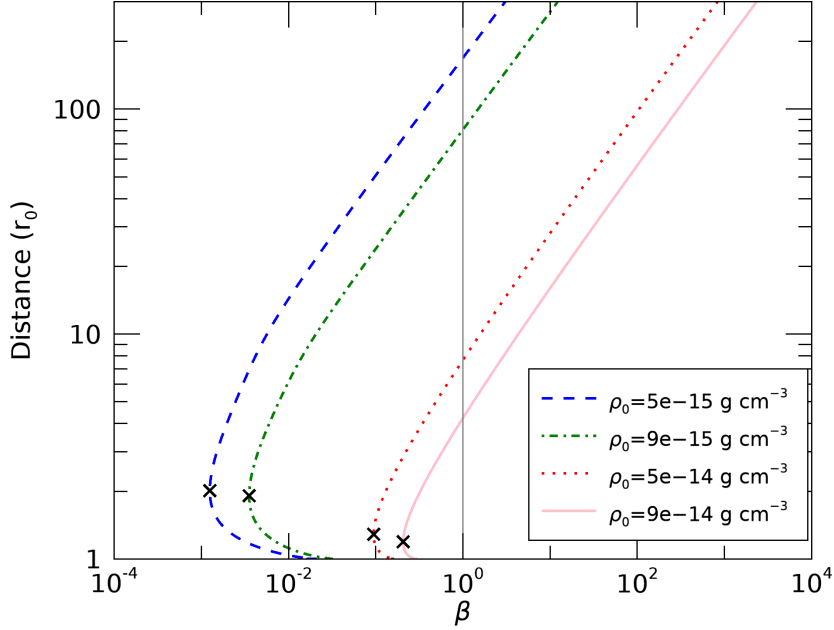


Figure 2.2: Plasma- β as function of the distance for a constant magnetic field of 5 G and different values of base density. The plot shows that the winds with lower densities (green-dash dotted and blue-dashed curves) are more magnetically dominated ($\beta < 1$) and higher density winds (pink-solid and red-dotted curves) are more thermally dominated ($\beta > 1$). The crosses denote the minimum of β , here defined as the base of the corona.

and, for each group, we extract local values of velocity, density and temperature at $r = 300 r_0$, which represent the asymptotic terminal wind velocity (u_∞), the density at large distances (ρ_{300}) and the “isothermal” (plateau) value of the temperature (T_{pl}), respectively. Note that the density profile is not constant, but it continues to fall with r^2 , following mass conservation of a constant-velocity wind. Within each ρ_0 group, there is a range of values of u_∞ , ρ_{300} and T_{pl} , due to different adopted B_0 . To better identify the global trends, we average values of u_∞ , ρ_{300} and T_{pl} for each group with same ρ_0 .

Fig. 2.3 shows the results we found for the general trends of the wind. The red points are the average values of T_{pl} and the solid line is the power-law fit. The shaded area in Fig. 2.3-a shows the range of the temperature plateau for different magnetic field values. The shaded area is larger for low- β values, but overall we see that the averages (red points) are good representation of the different simulation parameters. The temperature plateau (Fig. 2.3-a) depends on the base density and can be described by a power law fit:

$$T_{\text{pl}} = (7.8 \pm 0.2) \times 10^{14} \rho_0^{0.61 \pm 0.01}, \quad (2.12)$$

where T_{pl} is given in K and ρ_0 in g cm^{-3} . The numbers in parentheses in Equation (2.12)

2.3 Parametric study of winds of M-dwarfs

(and also in Equations 2.13 and 2.14) are the 1σ uncertainties for each coefficient of the fit. In our models, winds with higher base densities use a higher fraction of the wave flux to heat the wind, thus we find that an increase in the base density also increases the temperature plateau.

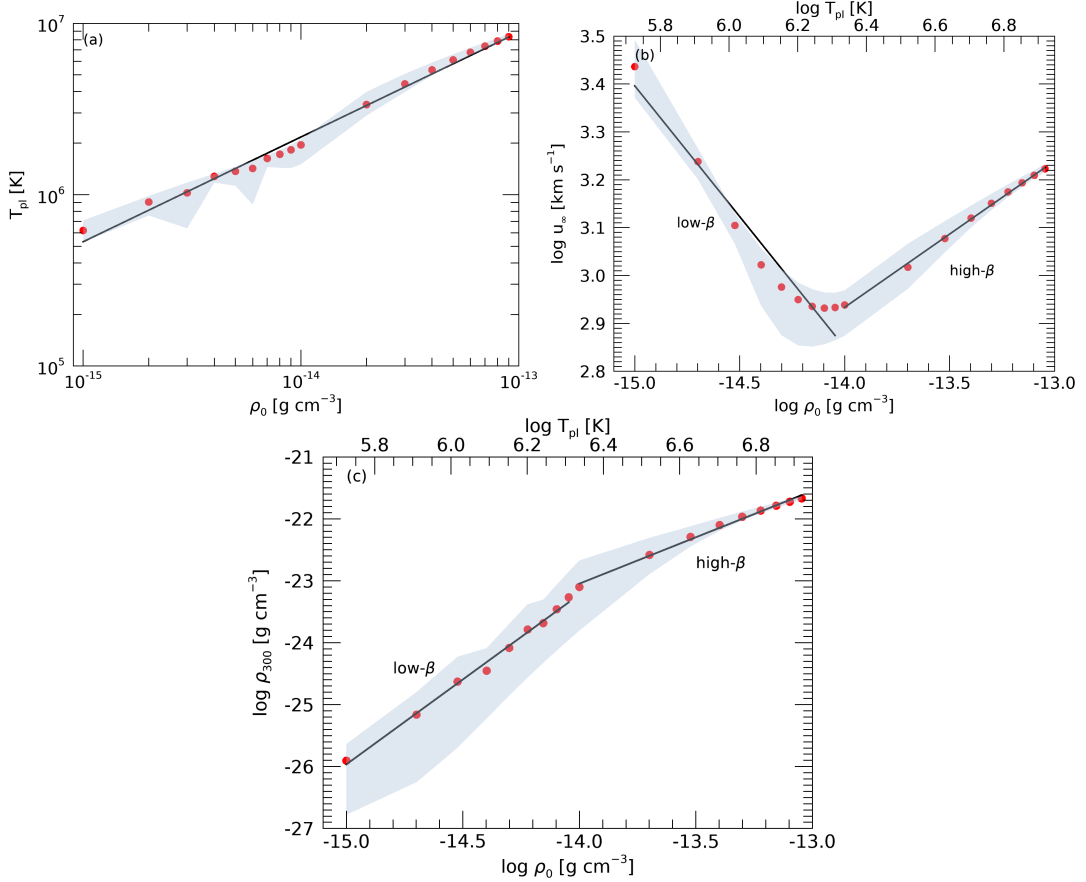


Figure 2.3: Given that for each ρ_0 , there are multiple simulations with different B_0 , we compute an average value (red points) of the (a) temperature plateau, (b) terminal velocity and (c) density at $r = 300 r_0$, for each group of simulations with the same ρ_0 . We see two different regimes for terminal velocity and density at $300 r_0$, according to their values of plasma- β . The shaded areas in all plots represents the extreme values for each plotted quantity, that are due to different assumed B_0 . The black lines are fits (Equations (2.12) to (2.14)).

The terminal velocity (Fig. 2.3-b) exhibits two different trends with base density. For low- β range, the terminal velocity falls off with base density, while for high- β range, the terminal velocity increases with base density. These two tendencies can be described by the power law fits:

$$\begin{cases} u_\infty = (1.59 \pm 0.64) \times 10^{-5} \rho_0^{-0.55 \pm 0.04}, & \text{for low-}\beta \\ u_\infty = (1.64 \pm 0.07) \times 10^7 \rho_0^{0.31 \pm 0.01}, & \text{for high-}\beta \end{cases} \quad (2.13)$$

where u_∞ is given in km s^{-1} and ρ_0 in g cm^{-3} . Here, we define low- β for $\rho_0 < 10^{-14} \text{ g cm}^{-3}$ and high- β for $\rho_0 \geq 10^{-14} \text{ g cm}^{-3}$. The shaded area in Fig. 2.3-b shows the range of the terminal velocity for different magnetic field values. Opposite to what happens with the temperature plateau, the terminal velocity has a slightly large range with magnetic field, except for high- β range. The terminal velocity shows a ‘V’ shape profile with base density, where the average values of terminal velocities vary from approximately $850 - 2700 \text{ km s}^{-1}$. In our simulations we can find the same terminal velocity for distinct values of wind temperature. Due to the fact that high- β cases are thermally driven, the terminal velocity follows a simple Parker wind in where the higher the plateau temperature, the higher the terminal velocity. However, low- β cases are more magnetically dominated and the wind speed becomes smaller with increase in base density for these cases. This occurs because the wind cannot be effectively accelerated due to the large quantity of material to lift up (larger inertia), which results in winds with lower terminal velocities. This is also seen in simulations by Suzuki et al. (2013).

The density at $300 r_0$ (Fig. 2.3-c) also has two different trends with base density, showing two different slopes for low and high- β values. These two trends can be described by the following power laws:

$$\begin{cases} \rho_{300} = (1.44 \pm 1.17) \times 10^{15} \rho_0^{2.74 \pm 0.08}, & \text{for low-}\beta, \\ \rho_{300} = (8.35 \pm 0.62) \times 10^{-3} \rho_0^{1.49 \pm 0.01}, & \text{for high-}\beta, \end{cases} \quad (2.14)$$

where ρ_{300} and ρ_0 are given in g cm^{-3} . Overall, the increase we see in ρ_{300} is affected by the increase in temperature. Stellar wind density profiles can be approximated as an exponential decay closer to the star, with a certain scale height. Higher temperature winds have larger scale heights, thus a slow density decay with distance. This would explain why as we go to higher wind temperatures, the density at $300 r_0$ remains larger (Fig. 2.1-c). The shaded area represents the range on the density at $300 r_0$ for different magnetic field values. Similarly to the other plots, the shaded area is larger for low- β and smaller for high- β cases. The density at $300 r_0$ is one of the most affected properties by the magnetic field variation, showing up to one order magnitude variation for the same ρ_0 in the low- β regime.

Given the relation between T_{pl} and ρ_0 (Fig. 2.1-a), in Panels b and c of Fig. 2.3, we add a top axis indicating T_{pl} values.

The mass-loss rate can be calculated assuming spherical symmetry as

$$\dot{M} = 4\pi r^2 u \rho. \quad (2.15)$$

2.3 Parametric study of winds of M-dwarfs

Since the mass-loss rate depends of the velocity and the density, as a result it is possible to determine the trend of \dot{M} with ρ_0 . Fig. 2.4 presents the relation between mass-loss rate, base density and temperature plateau (grey shaded area). The solid lines are given by the equations:

$$\dot{M} \propto \rho_{300} u_\infty \propto \begin{cases} \rho_0^{2.19}, & \text{for low-}\beta \\ \rho_0^{1.80}, & \text{for high-}\beta \end{cases} \quad (2.16)$$

Equation (2.16) comes from the combination of Equations (2.13) and (2.14). Even though the terminal velocity and the density at $300 r_0$ have two different trends with ρ_0 , the mass-loss rate increases with \sim base density squared. Given the linear dependence of \dot{M} with density (Equation (2.15)), why is $\dot{M} \propto \rho_0^2$? This is because the initial velocity of the wind, i.e., the one that is required for the wind to pass through the Alfvén radius, has a linear relation with base density. I.e., the denser the wind, the larger is its required initial velocity.

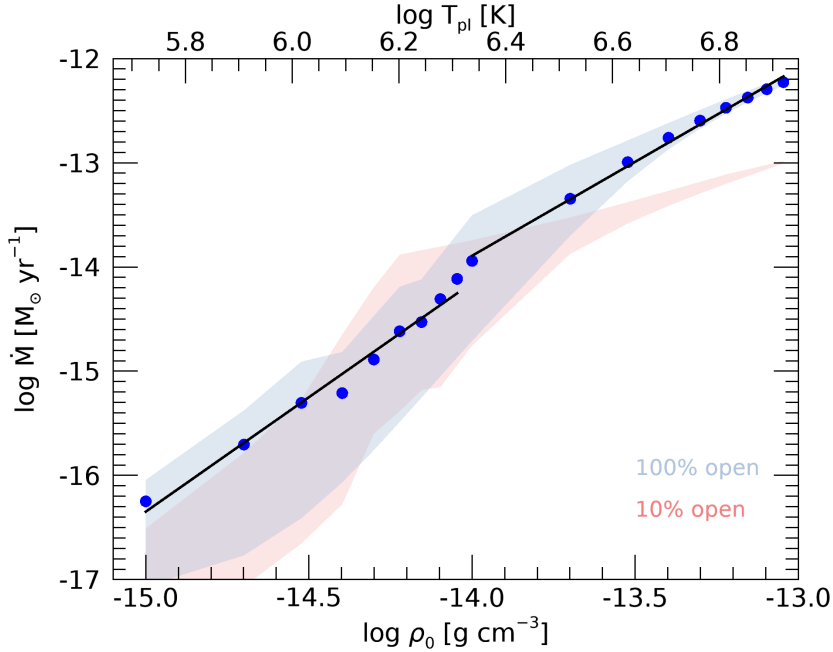


Figure 2.4: Mass-loss rate as function of base density and temperature plateau. The two straight lines are represented by Equation (2.16). The shaded area represents the minimum and maximum values of mass-loss rate for each value of base density. The blue shaded area represents the model with 100% open magnetic field lines and the red shaded area represents the model with only 10% open magnetic field lines (see Section 2.5.2).

The wind achieves the Alfvén velocity at the Alfvén radius r_A . The Alfvén radius determines, along with the mass-loss rate and rotation rate of the star, the amount of

angular momentum that is carried away by the stellar wind. The angular momentum-loss rate is

$$\dot{J} \propto \Omega_\star r_A^2 \dot{M}, \quad (2.17)$$

where Ω_\star is the stellar rotation rate. The angular momentum is important to explain how the observed rotation periods of the stars change as they age (Matt et al., 2015; Johnstone et al., 2015). In our simulations, we do not consider rotation, so in Fig. 2.5, we show $r_A^2 \dot{M}$, a proxy for the angular momentum-loss rate, as a function of base wave flux.

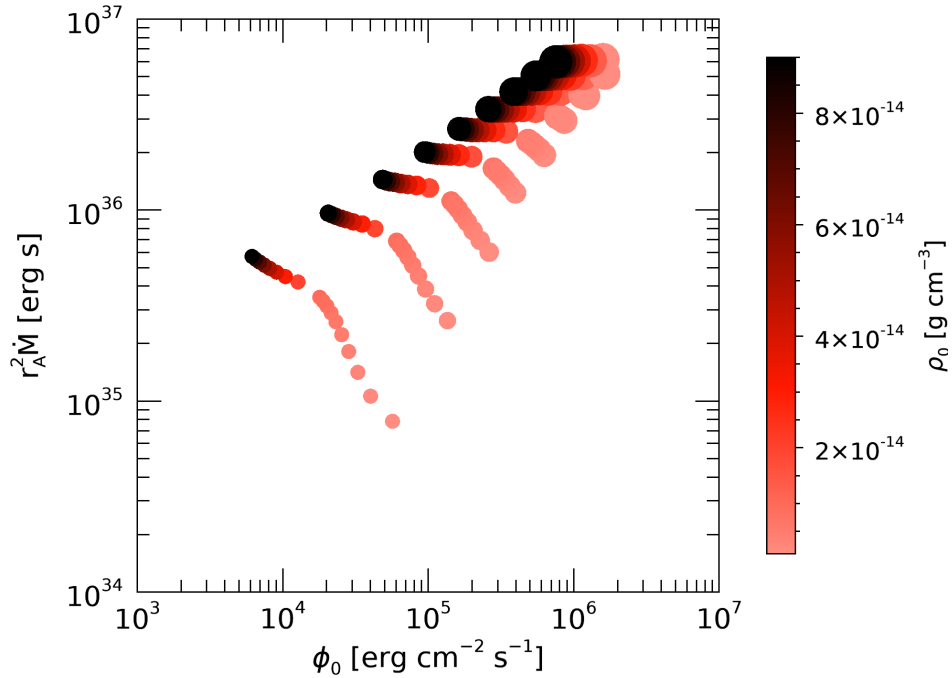


Figure 2.5: The angular momentum-loss rate, given by the proxy $r_A^2 \dot{M}$, as a function of wave flux colour-coded according to base density. The symbol sizes are associated with magnetic field intensity, which varies from 1 (left set of points) to 10 G (top right set of points). Angular momentum loss rates are larger for larger wave fluxes.

Rotation can alter the position of the Alfvén radius and the mass-loss rate, but these parameters are more affected in the case of fast rotation. From Fig. 2.5, we see that for a given value of base density, the angular momentum-loss rate is higher for higher wave fluxes. The magnetic field intensity is represented by the size of the symbols. Given that $\phi_{A,0} \propto \epsilon_0 v_{A,0} \propto (\delta B^2)_0 B_0 / \sqrt{\rho_0}$, higher values of magnetic fields show higher values of wave flux, when the density is kept constant. For a given value of magnetic field, the angular momentum-loss rate decreases with wave fluxes, this trend is more evident for small B_0 . In cases with higher B_0 the angular momentum-loss rate have a, roughly constant value, regardless of $\phi_{A,0}$.

2.4 Applications of our model

2.4.1 The extension of the chromosphere in inactive or moderately active M dwarfs

The chromospheric size of the present Sun is less than 1% of the solar radius (Aschwanden et al., 2001; Suzuki et al., 2013). In contrast, Czesla et al. (2012) showed, by using the Rossiter-McLaughlin effect, that a younger and active sun-like star, CoRoT-2A, could have a larger chromosphere extending to 16% of the stellar radius. Suzuki et al. (2013) also analysed the time evolution of the height of the chromosphere for young solar-like stars and found that the size of the chromosphere is time dependent and varies from 10%–20% of the stellar radius. They define the top of the chromosphere as the distance where the temperature is $T = 2 \times 10^4$ K. We use a different definition here, as we present below.

We start our simulation in the chromospheric region and we assume by simplicity that the top of the chromosphere also defines the base of the corona. In the Sun, the base of the corona starts when the beta parameter (Eq. 2.11) reaches a local minimum (Gary, 2001; Aschwanden et al., 2001). Below this local minimum, the photosphere has a high-plasma β , which reaches values of up to 100 (for a magnetic field of \sim kG). Above this local minimum, the plasma- β increases towards the corona. For the Sun, the minimum of plasma β happens at $\beta \simeq 0.01$, at a height of $\sim 0.003 R_{\odot}$ (Aschwanden et al., 2001).

We use the same idea here to define the top of the chromosphere/base of the corona in our simulations. In Fig. 2.2, the crosses indicate the position of the local minimum (and therefore the base of the corona) for two cases with low base density (dashed and dash dotted curves) and two cases with high base density (dotted and solid curves). In Fig. 2.2, for low- β cases the local minimum of β is around $2r_0$, while for the high- β , the local minimum of β is $\sim 1.2r_0$. Overall, for all our simulations, we find that low- β cases have the base of the corona in between 1.7 and $2.7r_0$, while for high- β cases, the base of the corona is in between 1.2 and $2.2r_0$.

This process to define the base of the corona also gives us an estimate of the size of the chromosphere. Fig. 2.6 shows the extension of the chromosphere as a function of base density where colour represents the magnetic field intensity. The larger the value of base density (high- β range), the smaller is the chromosphere of the star. Winds with higher magnetic field intensities show smaller chromospheres. For low- β range, we observe a large scatter in the chromospheric size.

From our simulations, we estimate that the size of the chromosphere is around 18% – 174% of the stellar radius, depending on our inputs. The extension of the chromosphere has a very wide range of values in our simulations and is considerably larger than that observed by Czesla et al. (2012) and derived by Suzuki et al. (2013) in the context of solar-like stars. The difference between the results of Suzuki et al. (2013) and ours can be due to the different types of stars and/or definitions of the top of the chromosphere used by each work. In our cases, the temperature at the top of the chromosphere vary from 0.6 to 3.5 MK, and, in theirs, it is assumed to be 2×10^4 K. They also have a transition region, which is not defined in our simulations.

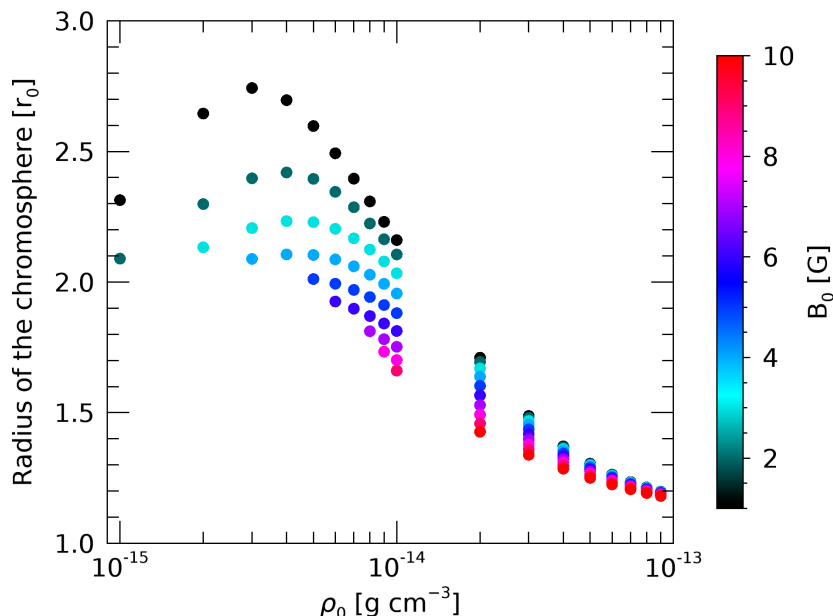


Figure 2.6: Extension of the chromosphere as function base density color-coded according to magnetic field intensity.

2.4.2 The wind of the planet-hosting star GJ 436

Cool dwarf stars, especially when more active, emit in X-rays. Here, we follow the work of Suzuki et al. (2013), and use our wind models to estimate the X-ray emission of the planet-hosting star GJ 436. This star has measurements of both X-ray luminosity and mass-loss rate. GJ 436 is an M2.5 dwarf star, located at 10.14 pc and host to an exoplanet GJ 436b at 0.0287 au (about $14.1 r_0$). Based on XMM-Newton EPIC-pn spectrum of GJ 436, Ehrenreich et al. (2015) reported an X-ray flux of $4.6 \times 10^{-14} \text{ erg s}^{-1} \text{ cm}^{-2}$ in the 0.12 – 2.48 keV band, resulting in an X-ray luminosity of $5.7 \times 10^{26} \text{ erg/s}$.

2.4 Applications of our model

By assuming that the radiative losses in the chromosphere is proportional to the X-ray luminosity, we can estimate the luminosity from the radiative losses (P_r):

$$L_X = \int P_r dV \quad (2.18)$$

where dV is the volume element. Here we perform the integral over $4\pi r^2 dr$, from $1 < r < 300 r_0$, but note that only the inner region of the wind, within $2 r_0$ contribute significantly to L_X . We note however that this underestimates the true X-ray luminosity of the star. Similar to the Sun, we expect that winds of M dwarfs are X-ray dark as they flow along open flux tubes (coronal holes) and are X-ray bright inside closed-field line regions. As in our simulations we only consider open flux tubes (i.e., the wind region), the observed X-ray luminosity is used as an upper limit to rule out certain simulations in our parameter space. With this, we can place an upper limit to the mass-loss rate of GJ 436. This is presented next.

Fig. 2.7 shows our computed X-ray luminosity as a function of the base density (top) or energy $E = k_B T_{\text{pl}}$ (bottom) for all our simulations. We get an X-ray luminosity ranging from $3.5 \times 10^{25} - 9.5 \times 10^{27} \text{ erg s}^{-1}$ and energy range from $0.05 - 0.7 \text{ keV}$ (corresponding to a wavelength ranging from 17 to 234 \AA). The energy bound includes the radiation in the ultraviolet range and also in the X-ray range.

The observed luminosity is marked in Fig. 2.7 by a horizontal line. We see that the models with base densities smaller than $7 \times 10^{-15} \text{ g cm}^{-3}$ would give rise to luminosities similar or smaller to the observed one. These models produce mass-loss rates smaller than $7.6 \times 10^{-15} M_{\odot} \text{ yr}^{-1}$, with Alfvén radius varying from $23 r_0 - 75 r_0$. This puts the planet orbiting at a distance below the Alfvén radius, in a sub-Alfvénic region. Because of the sub-Alfvénic interaction, energy can be transported back to the star, potentially causing star-planet interaction signatures on the star (Saur et al., 2013).

Vidotto & Bourrier (2017) used modelling of stellar wind interactions with upper planetary atmosphere of the warm-neptune GJ 436b to derive the global characteristics of the wind of GJ 436. Using this approach they estimated the mass-loss rate to be $(0.5 - 2.5) \times 10^{-15} M_{\odot} \text{ yr}^{-1}$, which is within our predictions. However, inspite of the mass-loss rate agreement, our models predict a local velocity that do not match with their values. While Bourrier et al. (2016) reported a local velocity of $69 - 91 \text{ km s}^{-1}$ at the orbit of the planet, our models give higher velocities with values $< 800 \text{ km s}^{-1}$. Our local densities are $< 2.8 \times 10^{-21} \text{ g cm}^{-3}$, in agreement with theirs ($1.34 - 7.02$) $\times 10^{-21} \text{ g cm}^{-3}$. Overall, the local wind velocity has a higher value in our work, but density has a similar value, and the combined values give a similar mass-loss rate to

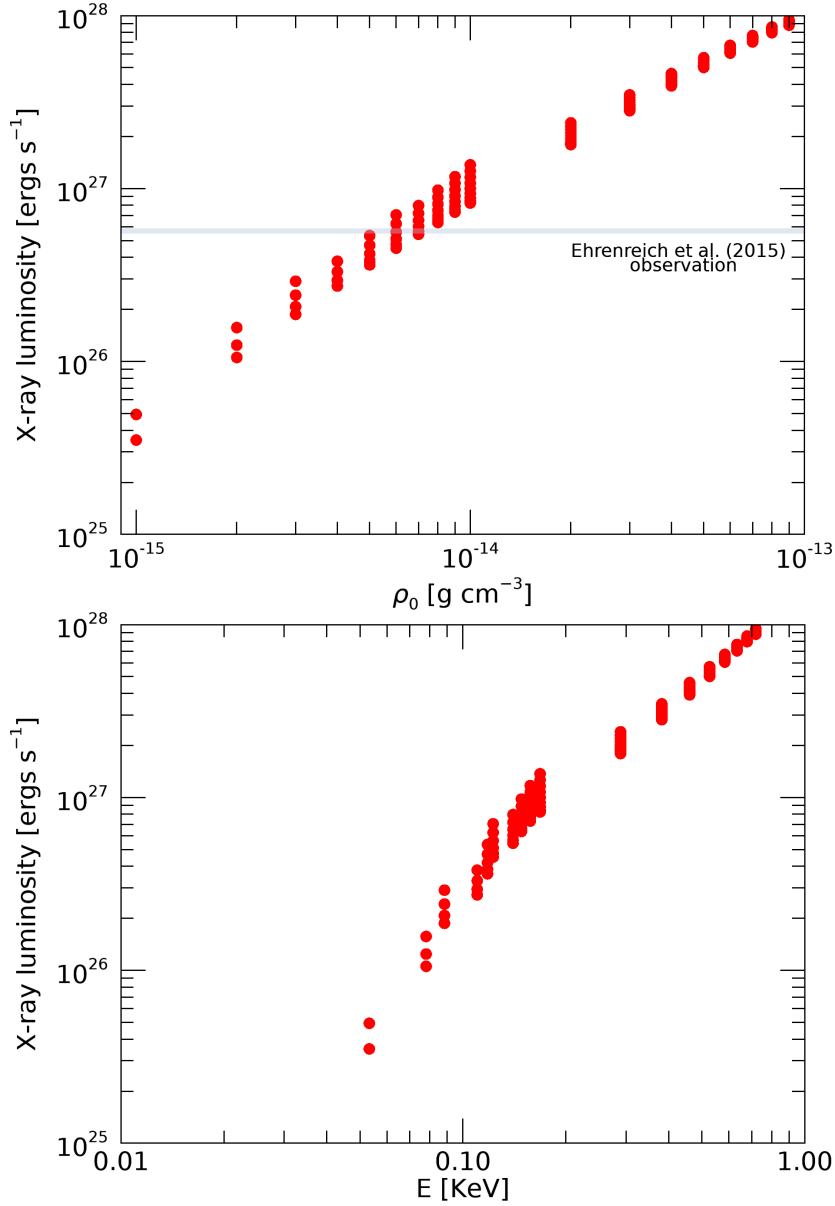


Figure 2.7: X-ray luminosity from radiative losses as function of the base density (top) and energy (bottom). The X-ray luminosity observed for GJ 436 is represented by the shaded area with the respective base density.

Vidotto & Bourrier (2017). By modelling the wind of GJ 436 as an isothermal wind, Vidotto & Bourrier (2017) found that the Parker wind cannot satisfy simultaneously the wind density, temperature and velocity reported in Bourrier et al. (2016). They suggested that this could be due to a different, or additional, acceleration mechanism for the wind (i.e., other than the thermal forces), such as, for example, the Alfvén-wave pressure force. Similar to their findings, our model cannot reproduce simultaneously the wind density, velocity and temperature reported in Bourrier et al. (2016).

2.5 Discussion

By modelling the Lyman- α transits, other works have also derived the properties of the wind of GJ 436, as it interacts with the warm Neptune GJ 436b. All these results are summarised in Table 2.2. It is surprising to see overall agreement between all these different models. All the works have densities of the same order of magnitude. Local wind velocities are also all in the same ballpark, although, except for Villarreal D’Angelo et al. (2021), other models predict a factor of 4 to 8 smaller velocities than ours. Mass-loss rates of all these works are also of similar magnitude, except for Kislyakova et al. (2019), who found \dot{M} higher than the other works. Maybe the largest disagreement is on the temperature values: our values are higher by a factor of a few than the values found by other works.

Table 2.2: Comparison of local stellar wind properties of GJ 436 at the position of GJ 436b for different works.

Velocity (km s ⁻¹)	Density (10 ⁻²¹ g cm ⁻³)	Temperature (MK)	\dot{M} (10 ⁻¹⁵ M_{\odot} yr ⁻¹)	
< 800	< 2.8	< 1.7	< 7.6	this work
69 – 91	1.34 – 7.02	0.36 – 0.46	0.5 – 2.5	Vidotto & Bourrier (2017)
110	3.4	0.41	35	Kislyakova et al. (2019)
170	6.7	0.6	4	set No 8 of Khodachenko et al. (2019)
470	0.5	0.17	2	Villarreal D’Angelo et al. (2021)

Still, the overall agreement indicates that planetary transits can be used as a way to study stellar wind properties, as proposed by Vidotto & Bourrier (2017). We note however, that, different models, like the Alfvén-wave driven wind and Parker wind models, can show similar properties at the orbital distances of exoplanets (Section 2.5.1). As a consequence, by using only planetary transit observations, it is difficult to distinguish between different models. Thus, it is more likely that models would only be able to derive some global characteristics of the wind (like mass-loss rate), but not the detailed physics of wind acceleration.

2.5 Discussion

2.5.1 Comparison between the Alfvén-wave driven wind and the Parker wind models

It is interesting to investigate how our results compare to the most commonly-adopted stellar wind model, namely the isothermal, Parker wind (PW) model. This has been done, for example, for solar wind simulation (Cohen, 2017), although here we use a different comparison method. In our comparison, we calculate the isothermal wind

solution for each of our simulations. One free parameter in the PW is the temperature. Given that our simulations reach a temperature plateau, we use this temperature plateau as an input for our PW simulations. While the base density plays an important role in the temperature profile in the Alfvén-wave driven wind (AWDW) simulations, this is not the case for a PW. Since the isothermal wind equations are independent of the density, the base density itself in a PW is a scaling factor for the mass-loss rate. Below we present a scheme of how we use the outputs of AWDW as a input for the PW.

$$\rho_{0(\text{AWDW})} \Rightarrow \begin{cases} \langle T_{\text{pl}} \rangle \\ \langle \rho_{\text{cor}} \rangle \end{cases} \Rightarrow \text{Parker Wind} \Rightarrow \begin{cases} u_{\infty(\text{PW})} \\ \dot{M}_{(\text{PW})} \end{cases}.$$

For a given set of simulations with same ρ_0 in our AWDW model, we extract values of average temperatures plateau and coronal base densities. These are then used as input for a PW simulation, which results in values of terminal velocity and mass-loss rate.

Unlike the AWDW simulation, the PW simulation starts at the corona, where the temperatures have already reached around a million K, therefore the base density needs to be chosen accordingly. We inspect the results of the AWDW to get the density of the corona for each simulation (see Section 2.4.1 for definition of the corona). This density at the base of the corona was used as the input density for the PW.

Fig. 2.8 shows the mass-loss rates, as calculated by Equation (2.15), for the PW (red dots) and AWDW (blue dots). At the $T_{\text{pl}} \gtrsim 10^{6.34}$ K, both wind mechanisms give similar values for mass-loss rate. This is because the velocity and density at large distances are similar in both models (see section 2.A). In contrast, at the $T_{\text{pl}} < 10^{6.34}$ K, the PW underestimates mass-loss rate by several orders of magnitude. The difference is particularly high ($\geq 10^4$ times) for cases with base density values smaller than $4 \times 10^{-15} \text{ g cm}^{-3}$.

In conclusion, the PW is a good representation of the AWDW for high- β , where the wind is thermally dominated. However, the PW can underestimate the terminal velocity and density, and thus mass-loss rate, for the low- β cases, where the wind is magnetically dominated.

2.5.2 Different parameters of the model

In the AWDW model, we have a considerable number of free parameters: ρ_0 , B_0 , T_0 , L_0 , $\sqrt{\langle \delta B_0^2 \rangle}$, damping type and two parameters to describe the flux tube geometry and coverage; in opposition to PW model which needs only T_0 and ρ_{cor} . We investigate now how these parameters affect the structure of our winds.

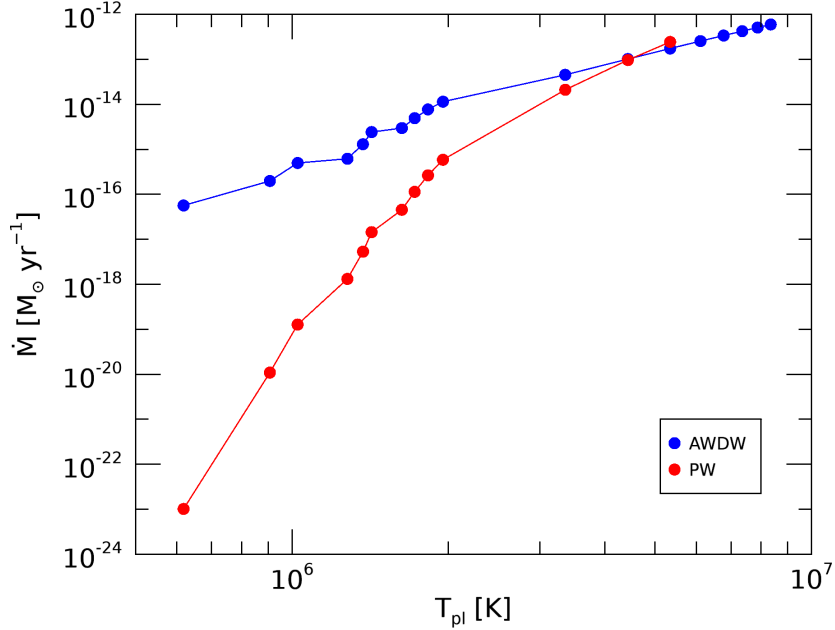


Figure 2.8: Mass-loss rate using Alfvén-wave driven wind (blue dots) and Parker wind (red dots). The PW mass-loss rate is underestimated for winds with low temperature plateau, and it is in good agreement with AWDW for high temperatures. The PW do not extend out to the same temperature range as the AWDW because the solution does not pass through the sonic point for those T_{pl} values.

2.5.2.1 Flux tube geometry

In order to investigate how the flux tube geometry and coverage affect our results, we run a set of 125 simulations with only 10% of open magnetic field line configuration. To implement this configuration we use a filling factor of open flux tubes, defined as $f_0 = \frac{1}{F_0} = 0.1$, which defines the open flux tubes coverage at the stellar surface. The open flux tubes have a super-radial expansion until a distance r_c , which defines the extension of the closed-field lines (Vidotto & Jatenco-Pereira, 2006). See sketch in Fig. 2.9.

For a given $S > 2$, r_c (Kuin & Hearn, 1982; Vidotto & Jatenco-Pereira, 2006) is defined by

$$F_0 = \frac{\Omega_c}{\Omega_0} = \frac{A(r_c)/r_c^2}{A(r_0)/r_0^2} = \left(\frac{r_c}{r_0}\right)^{S-2}, \quad (2.19)$$

where Ω_c and Ω_0 are the solid angle at $r = r_c$ and $r = r_0$, respectively, S the super radial expansion exponent and A is the area. We chose $S = 4.095$ because it gives rise to an extension of the closed field line region of $r_c = 3r_0$, which is similar to the value observed in the solar wind (i.e., above r_c the magnetic field is purely radial). The area

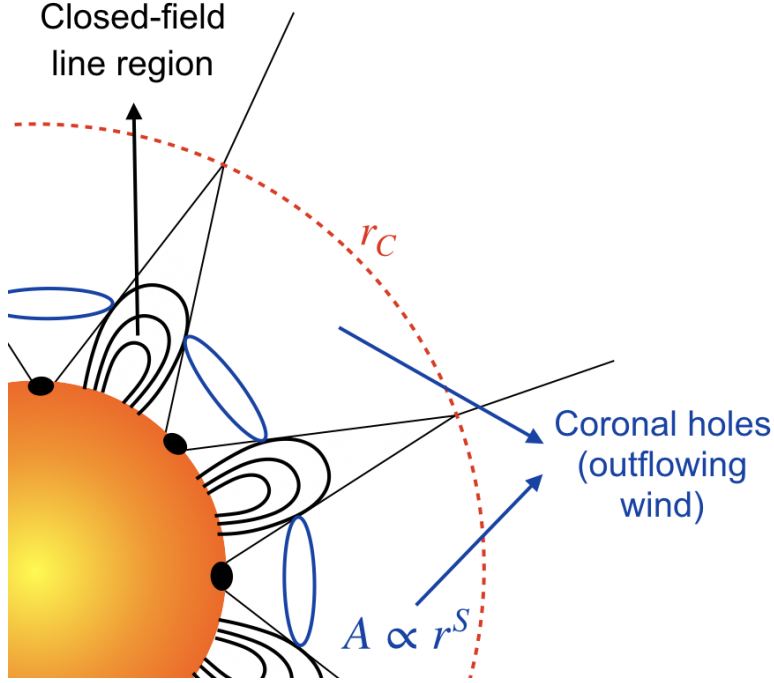


Figure 2.9: Sketch of a stellar atmosphere showing regions with closed-field lines and open-field lines (coronal holes). The coronal holes have super-radial flux tubes (area $A \propto r^S$, where S is the super radial expansion factor) until the point r_C , beyond which the flux tubes become radial.

of the flux tube is defined as

$$A(r) = \begin{cases} A(r_0)(r/r_0)^S, & \text{if } r \leq r_c \\ A(r_0)(r_c/r_0)^S(r/r_c)^2, & \text{if } r > r_c. \end{cases} \quad (2.20)$$

The new configuration (with 10% open magnetic field lines) shows a similar value of temperature plateau when compared with simulations with 100% open magnetic field lines. The density at $300 r_0$ is similar for low- β cases but smaller for high- β cases, around one order of magnitude. The terminal velocity is similar for high- β cases, but for low- β , u_∞ is considerably smaller, around half of the value. This can be understood by using an analogy of a pipe: if the aperture of the pipe is reduced, the velocity of the flow through the pipe increases. Similarly, if the aperture of the pipe is increased, the velocity of the flow goes down (assuming the same flux in both cases). The mass-loss rate have the same main trends as the ρ_{300} , as can be seen in Fig. 2.4 (red shaded area). In spite of changes in density and velocity, overall the mass-loss rates in both set of simulations are comparable.

2.5.2.2 Thermal properties

Back to our original geometry, we also run a set of simulations with a higher base temperature of 5×10^4 K (2.5 times higher than the previous value). Overall, the temperature of the wind increases, but we found that a higher T_0 does not significantly affect the wind velocity profile. However, the mass-loss increases by around one order of magnitude when compared with a lower base temperature. This is the same problem as seen in PW models, namely, that the mass-loss rate is sensitive to the temperature of the wind.

2.5.2.3 Properties of the waves

As discussed before in Section 2.4.2, our velocity values at the orbit of the planet GJ 436b is much higher than the values reported by Bourrier et al. (2016). In order to check if we could reproduce the low wind speed at GJ 436b orbit, we run our simulations with densities $(6 - 7) \times 10^{-15} \text{ g cm}^{-3}$ (which reproduces the luminosity value observed for GJ 436) but changing some properties of the waves, namely L_0 and $\sqrt{\langle \delta B_0^2 \rangle}$.

When we run the simulation with $L_0 = 0.01 r_0$ (one order of magnitude smaller than our main simulations), the temperature profile decreases (the factor depends on the B_0 intensity). The velocity profile also shows a small reduction. For example, if we compare the profiles for $\rho_0 = 6 \times 10^{-15} \text{ g cm}^{-3}$ and $B_0 = 1 \text{ G}$, the velocity at the planet orbit is $u_p = 430 \text{ km s}^{-1}$ using $L_0 = 0.1 r_0$ and $u_p = 402 \text{ km s}^{-1}$ using $L_0 = 0.01 r_0$. As we can see, there is a decrease in the velocity, but it is still much higher than the value observed by Bourrier et al. (2016).

When we run the simulation with $\sqrt{\langle \delta B_0^2 \rangle} = 0.01 B_0$ (one order of magnitude smaller than our main simulations), the density decreases less than one order of magnitude, the temperature also decreases, but to a lesser extent. The velocity, goes down very significantly, with the decrease being stronger for higher B_0 . For instance, for $\rho_0 = 6 \times 10^{-15} \text{ g cm}^{-3}$ and $B_0 = 3 \text{ G}$, the velocity at GJ 436b orbital distance is $u_p = 711 \text{ km s}^{-1}$ using $\sqrt{\langle \delta B_0^2 \rangle} = 0.1 B_0$ and $u_p = 348 \text{ km s}^{-1}$ using $\sqrt{\langle \delta B_0^2 \rangle} = 0.01 B_0$, which is about half of the previous value. The side effect of using a smaller value of $\sqrt{\langle \delta B_0^2 \rangle}$ is that it affects directly the mass-loss rate resulting in a new value smaller by around one order of magnitude.

From the discussion presented in Sections 2.5.2.1 to 2.5.2.3, we conclude that, as a consequence of several free parameters, it might be possible to find a set of inputs that would reproduce the observations by Bourrier et al. (2016). However, this is beyond

the scope of this paper and, in this work, we focus on discussing general trends of our model.

2.6 Conclusions

In this paper, we investigated the general trends of winds of M dwarfs. Our goal was to derive the main properties of the winds, including properties that could be observationally tested (size of the chromosphere and lower limits to X-ray luminosities). For that, we investigated how stellar winds from M dwarfs are affected by variations in the magnetic field and density at the chromosphere. Overall, we performed more than 300 MHD simulations with Alfvén wave energy fluxes spanning 4 orders of magnitude.

We classified our simulations in low- β ($\beta < 1$) and high- β ($\beta > 1$) regimes, which is related to the adopted values of base density (low and high, respectively). When the base density is larger, the temperature and density profiles are larger. The velocity profile has two different regimes: it decreases for low- β and increases for high- β with base density. To a lesser extent, the temperature, velocity and density profiles increase with magnetic field intensity (Fig. 2.1).

We calculated the mass-loss rate using Equation (2.15) and found that our mass-loss rates are proportional to ρ_0^2 . The square dependency with base density is associated to the fact that input velocity, required for the wind to pass through the Alfvén radius, is higher for cases with higher base density. We also calculate $r_A^2 \dot{M}$, which is proportional to the angular-momentum loss rate \dot{J} (Equation (2.17)). We found that \dot{J} increases overall with wave base flux (Fig. 2.5).

When compared to the Parker wind (PW), we showed that Alfvén-wave driven wind (AWDW) model accelerates more quickly but both wind mechanisms reach a similar terminal velocity for high- β . The PW can underestimate density by several orders of magnitude when compared with the AWDW – this feature is more accentuated for the low- β regime and is a consequence of both the large-distance density (ρ_{300}) and terminal velocity (u_∞) being underestimated in the PW model (Fig. 2.8). On the contrary, for high- β , both wind mechanisms give a similar mass-loss rate. This is due to the fact that the high- β regime is thermally dominated. We conclude that, the PW is a good representation of the AWDW for high- β , where the wind is thermally dominated. However, the PW can underestimate the terminal velocity and density, and thus mass-loss rate, for the low- β cases, where the wind is magnetically dominated.

As applications of our model, we use the local minimum of the plasma beta parameter to define the transition between the chromosphere and corona. We found that the

size of the chromosphere for M dwarf stars is more extended than that of our present-day Sun. We found that M dwarfs can have a very wide chromosphere extending to 18% – 174% of the stellar radius and is larger for the low- β regime.

Assuming that the X-ray luminosity is proportional to the radiative losses in the chromosphere, we estimated the X-ray luminosity from our stellar wind models. We compared our results with the observed X-ray luminosity of GJ 436 to constrain its mass-loss rate to be $\dot{M} < 7.6 \times 10^{-15} M_{\odot} \text{ yr}^{-1}$, with local velocities smaller than 800 km s^{-1} , local densities smaller than $2.8 \times 10^{-21} \text{ g cm}^{-3}$ and local temperatures $1.4 - 1.7 \text{ MK}$. Overall, our results are in good agreement with works that use Lyman- α transits to constrain the properties of the stellar wind (Vidotto & Bourrier, 2017; Kislyakova et al., 2019; Khodachenko et al., 2019; Villarreal D’Angelo et al., 2021). This indicates that transmission spectroscopy of planetary transits coupled with models can be used as a way to study stellar wind properties (Vidotto & Bourrier, 2017).

Acknowledgements

The authors acknowledge funding from the Provost’s PhD Project Awards, without which this work would not have been possible. AAV acknowledges funding from the Irish Research Council Consolidator Laureate Award 2018. This project has received funding from the European Research Council (ERC) under the European Union’s Horizon 2020 research and innovation programme (grant agreement No 817540, AS-TROFLOW).

2.A Further comparison between our wind models and a Parker wind

Here we present further comparison between the AWDW and the PW, following Section 2.5.1. We show in details the differences in the density and velocity profiles and the ratio of u_{∞} and ρ_{300} . Fig. 2.10 shows the comparison between the AWDW simulations and the PW simulations for a few selected cases: $\rho_0 = 9 \times 10^{-15} \text{ g cm}^{-3}$ and $B_0 = 1 \text{ G}$ (red-solid line) and 8 G (green-dashed line). The main difference is that the AWDW accelerates more quickly than the PW, but both methods reach a similar terminal velocity. This is due to the fact that once the AWDW reaches T_{pl} , and thus most of the wave energy has been deposited in the wind, the wind becomes thermally driven, similar to a PW. Fig. 2.10-a shows the velocity profile for both methods. It is interesting to note the similar decay of the three curves at large distance: this is the

r^{-2} decay of the density that is seen in all models. The density profile (Fig. 2.10-b) for the PW displays a more rarefied wind. Here, the coronal density of the PW was defined as the average density for all the cases with $\rho_0 = 9 \times 10^{-15} \text{ g cm}^{-3}$. We could, in principle, have scaled the dashed-dot blue curve of the PW to match either the 1-G or the 8-G model, given that the density in the PW is a scaling factor. This would force the density at large distances to be the same in the AWDW and PW models, but then they would deviate from each other at small distances.

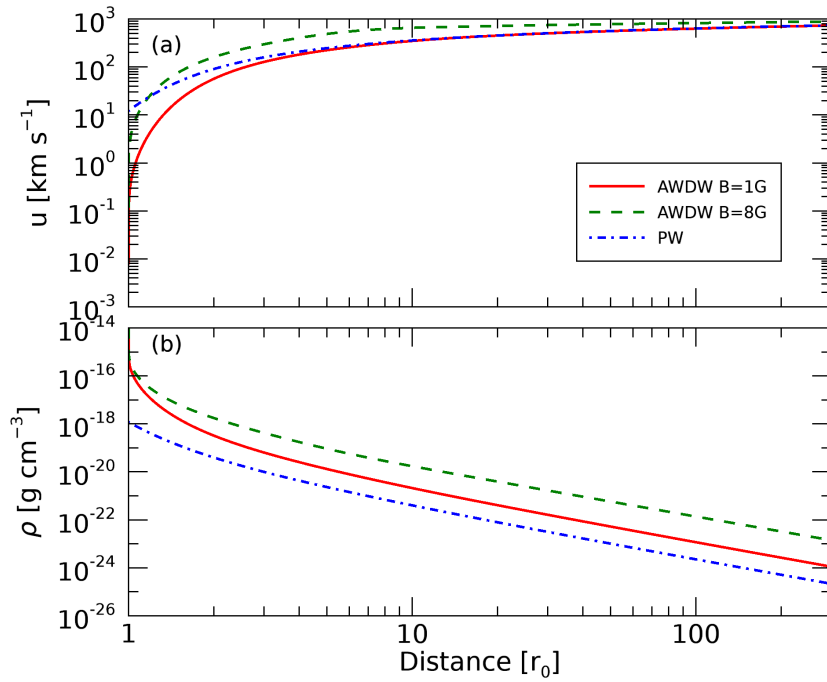


Figure 2.10: Comparison between the profiles for Parker wind (blue-dash dotted curve) and Alfvén-wave driven wind with $B=1 \text{ G}$ (red-solid curve) and with $B=8 \text{ G}$ (green-dashed curve). (a) velocity profile and (b) density profile.

Fig. 2.11 compares the results from the AWDW and the PW, for u_∞ (Fig. 2.11-a) and ρ_{300} (Fig. 2.11-b). We see that, for the high base density (high- β), the ratios are ~ 1 , showing that both methods reach similar results. In contrast, for the low base density regime (low- β), u_∞ can be nearly one order of magnitude larger for AWDW and ρ_{300} several orders of magnitude larger. Together, these two Figures explain why the PW deviates from the AWDW solution at low- β (Fig. 2.8).

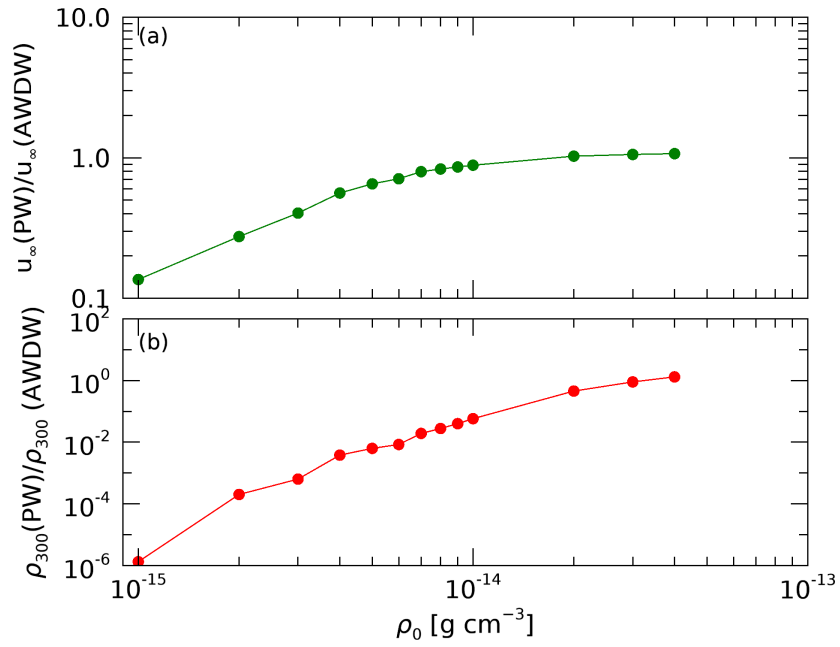


Figure 2.11: Ratio between the PW and the AWDW as function of base density, for (a) u_∞ and (b) ρ_{300} . For low density range, the PW shows smaller values for u_∞ and underestimated ρ_{300} while for higher densities the two models produce the same result for u_∞ and ρ_{300} .

The Earth-like Galactic cosmic ray intensity in the habitable zone of the M dwarf GJ 436

Amanda L. Mesquita, Donna Rodgers-Lee, & Aline A. Vidotto.
2021, MNRAS, 505, 1817–1826

Abstract

Galactic cosmic rays are energetic particles important in the context of life. Many works have investigated the propagation of Galactic cosmic rays through the Sun’s heliosphere. However, the cosmic ray fluxes in M dwarf systems are still poorly known. Studying the propagation of Galactic cosmic rays through the astrospheres of M dwarfs is important to understand the effect on their orbiting planets. Here, we focus on the planetary system GJ 436. We perform simulations using a combined 1D cosmic ray transport model and 1D Alfvén-wave-driven stellar wind model. We use two stellar wind set-ups: one more magnetically-dominated and the other more thermally-dominated. Although our stellar winds have similar magnetic field and velocity profiles, they have mass-loss rates two orders of magnitude different. Because of this, they give rise to two different astrosphere sizes, one ten times larger than the other. The magnetically-dominated wind modulates the Galactic cosmic rays more at distances < 0.2 au than the thermally-dominated wind due to a higher local wind velocity. Between 0.2 and 1 au the fluxes for both cases start to converge. However, for distances > 10 au, spatial diffusion dominates, and the flux of GeV cosmic rays is almost unmodulated. We find, irrespective of the wind regime, that the flux of Galactic cosmic rays in the habitable zone of GJ 436 (0.2–0.4 au) is comparable with intensities observed at Earth. On the other hand, around GJ 436 b (0.028 au), both wind regimes predict Galactic cosmic ray fluxes that are approximately 10^4 times smaller than the values observed at Earth.

3.1 Introduction

Galactic cosmic rays are energetic particles originating from explosive events such as the acceleration of charged particles in supernova remnants (Enomoto et al., 2002; Aharonian et al., 2004; Brose et al., 2020). These particles are constantly present in the interstellar medium (ISM), and in particular, Galactic cosmic rays are produced within our own Galaxy. There are extra-galactic sources of cosmic rays, but they are only relevant at much higher particle energies (Blasi, 2014). These sources are not being considered in the context of this work.

As Galactic cosmic rays travel through the heliosphere, they interact with the magnetised solar wind, which is known to cause global and temporal variations in the intensity and energy of the cosmic rays (see review by Potgieter, 2013). This phenomenon is known as *the modulation of Galactic cosmic rays*. The modulation of Galactic cosmic rays has been studied extensively in the context of the Sun and Sun-like stars. In this context, several works have investigated the modulation of Galactic cosmic rays at Earth’s orbit for different ages (Scherer et al., 2002, 2008; Müller et al., 2006; Svensmark, 2006; Cohen et al., 2012; Rodgers-Lee et al., 2020) to understand the possible effects of the cosmic rays during the Earth’s lifetime.

The size of the astrosphere¹ determines how far the Galactic cosmic rays must travel through a magnetised stellar wind. The astrospheric size is determined by the balance between the ISM and stellar wind ram pressures. Thus, the ISM ram pressure (i.e. the ISM properties, such as the density, velocity and ionization fraction) indirectly influences the propagation of Galactic cosmic rays. Some works modelled the response of the astrosphere under different configurations for the ISM conditions around the heliosphere (Scherer et al., 2002, 2008; Müller et al., 2006) and other astrospheres (Jasinski et al., 2020). Müller et al. (2006) found that the heliospheric structure and size changed and found a wide range of possible heliopause locations varying from 12 to 402 au. They also showed that the Galactic cosmic ray spectrum at the Earth’s orbit is significantly affected by the ISM conditions, where larger astrospheres cause more modulation of Galactic cosmic rays. From the extreme sizes of the heliosphere, they found approximately three orders of magnitude difference in the Galactic cosmic ray fluxes at the Earth’s orbit.

More recently, some works have also studied the modulation of Galactic cosmic rays for a number of M dwarf stars (Sadowski et al., 2018; Herbst et al., 2020). M dwarfs are low mass, low luminous and cool stars. They are especially interesting

¹An astrosphere is the equivalent of the heliosphere for other stars.

because their habitable zone, the region where a planet can sustain liquid water on its surface, is closer to the star (Kasting et al., 1993; Selsis et al., 2007). This makes M dwarf systems the perfect candidates for transit observations of potentially habitable planets. As a result, exoplanets around M dwarfs are currently the main targets in searching for life outside our solar system (Scalo et al., 2007; Tarter et al., 2007). Close-in exoplanets around low mass stars, such as M dwarfs, are currently easiest to observe due to observation bias in our present-day detection technology.

However, a large fraction of M dwarfs remain magnetically active for a longer period of their lives compared to solar-mass stars (West et al., 2004; Scalo et al., 2007; West et al., 2015; Guinan et al., 2016), with the fraction of active M dwarfs being larger for later spectral types (see, e.g., West et al., 2008). M dwarfs can generate strong magnetic fields (Morin et al., 2010; Shulyak et al., 2019). Strong stellar activity means that the star could have stronger flares (Vida et al., 2017; Tilley et al., 2019) and coronal mass ejections (Lammer et al., 2007; Khodachenko et al., 2007), more high energetic particles (Gri  meier et al., 2005) and it could affect the stellar wind (Vidotto et al., 2014a). All of these phenomena can affect planet habitability (Khodachenko et al., 2007; Vida et al., 2017; Tilley et al., 2019). The longer exposure time to stellar radiation and stellar energetic particles could also affect the planetary atmosphere (Rimmer & Helling, 2013; Rimmer et al., 2014; Tabataba-Vakili et al., 2016; Scheucher et al., 2018) and climate (Grenfell et al., 2013).

Active M dwarfs generate strong magnetic fields and have higher levels of magnetic activity. These stars should be efficient at accelerating stellar cosmic rays (energetic particles generated by the star). In addition, they have close-in habitable zones and many observed close-in exoplanets. For this reason, stellar cosmic ray fluxes can be expected to dominate over Galactic cosmic rays up to a given energy around these stars. Some works have investigate the effects of stellar cosmic rays on exoplanets' magnetospheres and atmospheres (Segura et al., 2010; Grenfell et al., 2012; Tabataba-Vakili et al., 2016; Scheucher et al., 2020), in the habitable zone of M dwarfs (Fraschetti et al., 2019) and at Earth's orbit for different ages (Rodgers-Lee et al., 2021a). Here, we do not focus on very magnetically active stars. Additionally, we do not consider stellar cosmic rays in this work.

In exoplanet atmospheres, cosmic rays can drive the production of prebiotic molecules (Airapetian et al., 2016; Barth et al., 2021) which are thought to be important for the origin of life. Cosmic rays may have been relevant for the origin of life on Earth and could potentially be relevant for the origin of life on other planets as well (Airapetian et al., 2016; Atri, 2016). On the other hand, large fluxes of cosmic rays

3.1 Introduction

can be extremely harmful for life as we know it (Shea & Smart, 2000), as they can damage the DNA in cells (Sridharan et al., 2016) and possibly cause cellular mutation (Dartnell, 2011). However, the majority of cosmic rays do not interact directly with the planet’s surface as the surface is protected by an atmosphere and potentially a magnetosphere as well. Works have shown that the flux of cosmic rays at the planetary surface can be reduced by the existence of a magnetosphere (Grenfell et al., 2007; Grießmeier et al., 2009, 2015) and an atmosphere (Grießmeier et al., 2016; Atri, 2020). Grießmeier et al. (2015) found that the flux of cosmic rays reaching the planetary atmosphere can be enhanced by more than three orders of magnitude if the planet does not have a protecting magnetic field. Additionally, Atri (2020) found that the radiation dose on the planet surface can be reduced by increasing the depth of its atmospheric column density (Atri et al., 2013; Atri, 2017). Some works also suggest that cosmic rays could affect the Earth’s climate through cloud cover (Svensmark & Friis-Christensen, 1997; Shaviv, 2002, 2003; Kirkby et al., 2011; Svensmark et al., 2017).

In our present work, we investigate how the winds of M dwarfs can affect the flux of Galactic cosmic rays that penetrate the astrospheres of these stars. In particular, we use results from Mesquita & Vidotto (2020) who modelled the wind of GJ 436, a moderately active planet-hosting star. In their work the stellar wind was heated and driven by the presence of Alfvén waves originating from the base of the chromosphere. The advantage of the Alfvén-wave-driven stellar wind model is that it gives a detailed structure of the wind energetics, such as heating (see Section 3.2.2 for more details). At the same time, it is particularly difficult to observe the winds of M dwarfs, since they have a rarefied wind. Some methods have been proposed to measure the winds of low-mass stars (see review by Vidotto, 2021), such as through astrospheric Lyman- α absorption (Wood, 2004; Wood et al., 2014, and references therein), radio emission (Panagia & Felli, 1975; Lim & White, 1996; Fichtinger et al., 2017; Vidotto & Donati, 2017), X-ray emission (Wargelin & Drake, 2001, 2002), slingshot prominences (Jardine & Collier Cameron, 2019) and exoplanet atmospheric escape (Vidotto & Bourrier, 2017; Kislyakova et al., 2019). These works help to give some constraints on the mass-loss rate for a number of low-mass stars. However, for the majority of objects, some stellar wind parameters are still not fully known, such as the mass-loss rate and terminal wind velocity. For this reason, in our previous work, we varied a number of input parameters. Here, we selected two wind regimes from Mesquita & Vidotto (2020), a more magnetically-dominated wind and a thermally-dominated wind, to investigate if the wind regime could affect the flux of Galactic cosmic rays in the habitable zone of

GJ 436 and at GJ 436 b. The most important difference between the two wind regimes is that they have mass-loss rates which differ by two orders of magnitude.

GJ 436 is a very well studied M2.5 dwarf star due to its close proximity at 10.14 pc (Turnbull, 2015). It has a mass of $0.45 M_{\odot}$, a radius of $R_{\star} = 0.437 R_{\odot}$ (Knutson et al., 2011) and a rotation period of 44 days (Bourrier et al., 2018). Chromospheric activity indicates that GJ 436 has modest stellar magnetic activity compatible with an old M dwarf (Butler et al., 2004). GJ 436 hosts at least one known exoplanet, GJ 436 b, at 0.028 au (about $14.1 R_{\star}$), first discovered by Butler et al. (2004). GJ 436 b is a warm-Neptune planet with an orbital period of 2.64 days (Butler et al., 2004). The system itself is very interesting, with the planet being observed to lose a substantial amount of its atmosphere (Kulow et al., 2014; Bourrier et al., 2015; Ehrenreich et al., 2015; Bourrier et al., 2016).

Here, we investigate the intensity of Galactic cosmic rays in the stellar system GJ 436. We use the one-dimensional model of cosmic rays transport from Rodgers-Lee et al. (2020) to calculate the spectrum of Galactic cosmic rays at different orbital distances in GJ 436’s astrosphere. The model is based on the transport equation of Parker (1965). This paper consists of the following sections: in Section 3.2, we describe the transport equation that is used to describe the propagation of the Galactic cosmic rays as they travel inside the astrosphere. We also include information about the stellar wind used as an input parameter in our simulations. Our results on the size of GJ 436’s astrosphere for the two different stellar wind regimes, the flux of Galactic cosmic rays in the habitable zone and around the planet’s orbit are given in Section 3.3. Finally, we discuss the important parameters used in our simulations and compare our results with other works in Section 3.4, followed by our conclusions in Section 3.5.

3.2 Galactic Cosmic ray propagation

Galactic cosmic rays travel throughout the ISM. They interact with stellar winds and penetrate the astrospheres of stars, the region of space around stars dominated by the outflow of their magnetised stellar winds. Fig. 3.1 shows a schematic of Galactic cosmic rays propagating inside the astrosphere region. The stellar wind is able to modulate the cosmic rays as they progress inside the astrosphere. Here, we recall that modulation refers to the global variations in the intensity and energy of the cosmic rays as they travel through the stellar wind. In our work, we do not consider the temporal variations. This modulation can be described by the diffusive transport equation of

3.2 Galactic Cosmic ray propagation

Parker (1965). The model used in this work is based on the model used in Rodgers-Lee et al. (2020) which solves the diffusive transport equation which we describe next.

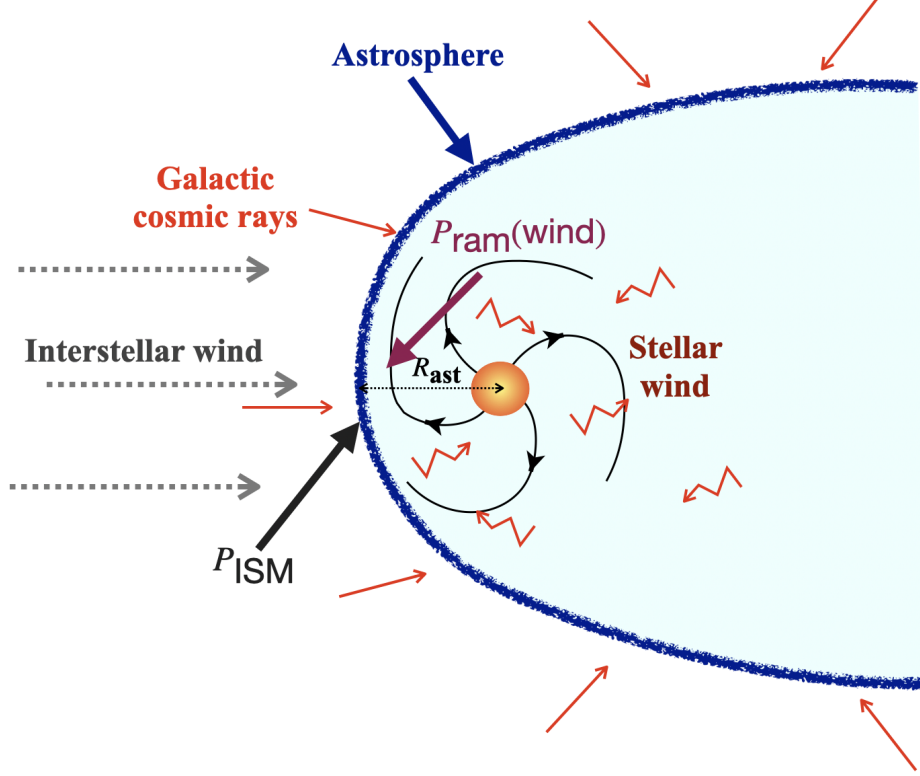


Figure 3.1: Sketch showing the region dominated by the stellar wind environment (the astrosphere) surrounded by the interaction with the ISM in the inertial frame of the star. The red arrows depict the Galactic cosmic rays propagating into the astrosphere. In red we show the propagation of Galactic cosmic rays as they diffuse through the astrosphere. P_{ram} is the stellar wind ram pressure and P_{ISM} is the ISM ram pressure.

Here, we numerically solve the one dimensional time-dependent, spherically symmetric transport equation for cosmic rays, given by

$$\frac{\partial f}{\partial t} = \nabla \cdot (\kappa \nabla f) - u \cdot (\nabla f) + \frac{1}{3} (\nabla \cdot u) \frac{\partial f}{\partial \ln p}, \quad (3.1)$$

where $f(r, p, t)$ is the cosmic ray phase space density, $u(r)$ is the stellar wind velocity, $\kappa(r, p)$ is the spatial diffusion coefficient, p is the momentum of the cosmic rays and r is the radial distance from the star. The terms on the right-hand side of Equation (3.1) are the spatial diffusion of cosmic rays through the stellar wind, spatial advection and momentum advection, respectively. The spatial advection impedes the propagation of cosmic rays inside the astrosphere and the momentum advection drives the cosmic rays to lower energies, also known as adiabatic losses.

The propagation of cosmic rays through the stellar wind is a diffusive process which depends on the level of turbulence and strength of the magnetic field of the stellar wind. The particles undergo a random walk through the magnetic field lines. From quasi-linear theory (Jokipii, 1966; Schlickeiser, 1989), the diffusion coefficient of the cosmic rays can be expressed as

$$\frac{\kappa(r, p)}{\tilde{\beta}c} = \eta_0 \left(\frac{p}{p_0} \right)^{1-\gamma} r_L, \quad (3.2)$$

where $\tilde{\beta} = v/c$ is the particle speed as a fraction of the speed of light, $p_0 = 3 \text{ GeV}/c$, $r_L = p/eB(r)$ is the Larmor radius of the protons and

$$\eta_0 = \left(\frac{B}{\delta B_{\text{turbulence}}} \right)^2, \quad (3.3)$$

where B^2 is connected with the energy density of the stellar wind large-scale magnetic field and $\delta B_{\text{turbulence}}^2$ to the total energy density in the smaller scale magnetic field turbulent modes. η_0 represents the level of turbulence in the magnetic field and here we adopted $\eta_0 = 1$ which sets the maximum value for the turbulence. γ is related to the turbulence power spectrum and it defines how the diffusion coefficient changes with energy. Here, we adopt $\gamma = 1$ which corresponds to Bohm diffusion and is the same value used by Svensmark (2006), Cohen et al. (2012) and Rodgers-Lee et al. (2020). With these values, the present day observations of the cosmic ray flux at 1 au are well reproduced (see Figure A1 from Rodgers-Lee et al., 2020). We used logarithmically spaced spatial and momentum grids with 60 grid zones each. The outer spatial boundary for case A is 33 au and for case B, it is 363 au (see Section 3.2.3). The inner spatial boundary for both cases is 0.01 au. The minimum momenta, used in our simulations, is $p_{\text{min}} = 0.15 \text{ GeV}/c$ and maximum momenta $p_{\text{max}} = 100 \text{ GeV}/c$.

In our model, the key parameters necessary for solving the Galactic cosmic ray modulation are: the Galactic cosmic ray spectrum outside the astrosphere, the stellar wind parameters and the size of the astrosphere (which depends on the ISM parameters combined with the stellar wind parameters), which we will detail in the next subsections. We describe the local interstellar spectrum for Galactic cosmic rays and the fit used in this work in Section 3.2.1. In Section 3.2.2 we summarise the stellar wind parameters and the wind driving mechanism used. In Section 3.2.3 we demonstrate how we calculated the size of GJ 436's astrosphere.

3.2.1 Local Interstellar Spectrum (LIS)

Outside of the astrosphere Galactic cosmic rays are unmodulated by the stellar wind. For our simulations an unmodulated Galactic cosmic ray spectrum is needed at the outer spatial boundary condition. For this unmodulated boundary condition, we adopt the local interstellar spectrum (LIS).

After crossing the heliopause (the boundary that separates the solar wind and the ISM), Voyager 1 made Galactic cosmic ray observations, which are thought to be unaffected by the solar modulation (Stone et al., 2013; Cummings et al., 2016). Using observations of Voyager 1, Vos & Potgieter (2015) developed a model fit to describe the differential intensity of the LIS, j_{LIS} , given by

$$j_{\text{LIS}}(T) = 2.70 \frac{T^{1.12}}{\tilde{\beta}^2} \left(\frac{T + 0.67}{1.67} \right)^{-3.93} \text{ m}^{-2} \text{ s}^{-1} \text{ sr}^{-1} \text{ MeV}^{-1}, \quad (3.4)$$

where T is the kinetic energy of the cosmic rays in GeV. The differential intensity of cosmic rays can be expressed in terms of the phase space density as $j(T) = p^2 f(p)$. In our simulations the LIS is considered to be constant as a function of time.

Equation (3.4) describes, by construction, the amount of Galactic cosmic rays at the heliopause at 122 au and is valid for the solar case. Unfortunately, we do not have observations of the Galactic cosmic ray spectrum outside GJ 436's astrosphere. In-situ measurements of Galactic cosmic rays in locations other than the solar system is not possible. On the other hand, γ -ray observations of nearby molecular clouds have been used to infer the cosmic ray spectrum for other locations in the Galaxy (Neronov et al., 2017; Aharonian et al., 2020; Baghmanyany et al., 2020). γ -ray emission is generated when cosmic rays interact with matter as they travel in the Galaxy. According to Neronov et al. (2017) the inferred cosmic ray spectrum from γ -ray observations across a region of 1 kpc in the local Galaxy is in agreement with Voyager measurements at 122 au. For this reason, it is reasonable to use the LIS measured by Voyager 1 as the outer spatial boundary condition for the simulations of the GJ 436 stellar system.

3.2.2 Stellar wind parameters

The key parameters for our Galactic cosmic ray propagation model are the physical properties of the stellar wind, such as the magnetic field and velocity. To derive such parameters, we use the results of wind simulations from Mesquita & Vidotto (2020). In their simulations, the wind of GJ436 is heated and accelerated by the dissipation of Alfvén waves, analogous to similar processes occurring in the the solar wind (e.g.,

Cranmer & Winebarger 2019; for other Alfvén-wave-driven wind models in the context of M dwarfs, see Garraffo et al. 2016; Mesquita & Vidotto 2020; Sakaue & Shibata 2021; Kavanagh et al. 2021). In Mesquita & Vidotto (2020), the Alfvén waves are generated at the base of the wind due to perturbations induced on the magnetic field. The wind is launched at the chromosphere and extends until 0.6 au ($300 R_\star$), where the wind has reached its terminal velocity. In their models, the increase in temperature from the chromosphere to the corona occurs naturally. Other models, such as thermally-driven wind models, for instance, cannot model this temperature rise and instead already assume a million Kelvin-temperature wind (e.g., Vidotto et al. 2014a. See Vidotto 2021 for a recent review on the winds of low-mass stars).

To investigate the modulation of Galactic cosmic rays around GJ 436 we choose two sets of wind parameters from Mesquita & Vidotto (2020), which had more than 134 simulations. Note that the different wind models can affect the results of the cosmic ray simulations, we discuss these effects further in Section 3.4. Two sets of wind parameters were selected in particular because one is more magnetically-dominated, further referred as ‘case A’, and the other is more thermally-dominated, further referred as ‘case B’. Although both sets assume the same magnetic field strength at the wind base ($B_0 = 4$ G), they have different base densities, which implies that the energy fluxes of the Alfvén waves at the wind base are different for each case, resulting in different radial profiles for the velocity and density, as well as different mass-loss rates.

The first stellar wind, ‘case A’, has a terminal velocity of $u_\infty = 1250 \text{ km s}^{-1}$, a density at the chromosphere of $\rho_0 = 4 \times 10^{-14} \text{ g cm}^{-3}$ and a density at 0.6 au of $\rho_{0.6 \text{ au}} \sim 6 \times 10^{-25} \text{ g cm}^{-3}$. The second stellar wind, ‘case B’, has a terminal velocity $u_\infty = 1290 \text{ km s}^{-1}$, a density at the chromosphere of $\rho_0 = 3 \times 10^{-15} \text{ g cm}^{-3}$ and a much higher density at 0.6 au of $\rho_{0.6 \text{ au}} \sim 7 \times 10^{-23} \text{ g cm}^{-3}$. The mass-loss rate for Case B is a factor of 125 higher than for case A. Table 3.1 summarises the relevant physical properties of the planet-hosting stellar system, GJ 436. Table 3.2 shows the stellar wind parameters, the astrosphere sizes and the derived parameters for the modified force field approximation in the habitable zone and at GJ 436 b orbital distance for each case (see Section 3.3.3).

In Mesquita & Vidotto (2020), case A is one of the models in the group called ‘low- β cases’ and case B is one of the models in the group called ‘high- β cases’, where β here refers to the plasma β parameter, which is the ratio between the thermal and magnetic pressures. As discussed in Mesquita & Vidotto (2020), case A is our preferred model for this star, as it predicts an X-ray luminosity that is consistent with that observed for GJ 436 (Ehrenreich et al., 2015).

3.2 Galactic Cosmic ray propagation

Table 3.1: Properties of the planet-hosting stellar system GJ 436 relevant for this work.

Physical parameter	Symbol	Value	Unit
Stellar mass ^a	M_{\star}	0.452	M_{\odot}
Stellar radius ^a	R_{\star}	0.437	R_{\odot}
Stellar rotation period ^b	P_{rot}	44	days
Stellar angular speed	Ω	1.65×10^{-6}	rad s^{-1}
ISM velocity ^c	ν_{ISM}	81	km s^{-1}
ISM column density ^d	N_{ISM}	1×10^{18}	cm^{-2}
ISM average H density ^c	n_{ISM}	0.03	cm^{-3}
ISM ram pressure ^c	P_{ISM}	3.3×10^{-12}	dyn cm^{-2}
Habitable zone		0.2 – 0.4	au
Semi-major axis ^e	a	0.028	au

^aKnutson et al. (2011).

^bBourrier et al. (2018).

^cVidotto & Bourrier (2017).

^dBourrier et al. (2015).

^eButler et al. (2004).

Table 3.2: Important parameters of each case studied here. We used two Alfvén-wave-driven stellar wind models from Mesquita & Vidotto (2020) consisting of a magnetically-dominated wind (case A) and a thermally-dominated wind (case B). The columns are, respectively, the case ID, the terminal velocity, the magnetic field strength and density at the stellar wind base, the magnetic field strength and density at 0.6 au, the wind mass-loss rate, the Alfvén radius, the astrosphere size and the modified force field approximation parameter ϕ (see Section 3.3.3) at the habitable zone (0.2 – 0.4 au) and at the orbital distance of GJ 436 b (0.028 au).

Case	u_{∞} [km s ⁻¹]	B_0 [G]	ρ_0 [g cm ⁻³]	$B_{0.6 \text{ au}}$ [G]	$\rho_{0.6 \text{ au}}$ [g cm ⁻³]	\dot{M} [$10^{-15} M_{\odot} \text{ yr}^{-1}$]	R_A [au]	R_{ast} [au]	ϕ_{HZ} [GeV]	$\phi_{\text{GJ 436 b}}$ [GeV]
A	1250	4	3×10^{-15}	3.85×10^{-5}	6×10^{-25}	1.2	0.08	33	0.38 - 0.15 ^a	2.70 ^b
B	1290	4	4×10^{-14}	3.85×10^{-5}	7×10^{-23}	150	0.01	363	0.40 - 0.18 ^a	2.20 ^b

^a The values of ϕ in the habitable zone are only well-defined for particle energies above $\gtrsim 200$ MeV. At lower energies, the analytical expression can overestimate the flux considerably, see Section 3.3.3.

^b The values of ϕ for GJ 436 b are only well-defined for particle energies above $\gtrsim 1$ GeV. At lower energies, the analytical expression can overestimate the flux considerably, see Section 3.3.3.

The stellar wind models from Mesquita & Vidotto (2020) end at 0.6 au (where the wind has reached its terminal velocity) but the astrosphere extends much further out. Thus, we extrapolate the values of u_r , B_r and B_{ϕ} beyond 0.6 au to the astrosphere edge as

$$u_r(r > 0.6 \text{ au}) = u_{r, 0.6 \text{ au}} = u_{\infty}, \quad (3.5)$$

$$B_r(r > 0.6 \text{ au}) = B_{r, 0.6 \text{ au}} \left(\frac{0.6 \text{ au}}{r} \right)^2, \quad (3.6)$$

$$B_\phi(r > 0.6 \text{ au}) = B_{\phi, 0.6 \text{ au}} \left(\frac{0.6 \text{ au}}{r} \right). \quad (3.7)$$

The velocity is assumed to be constant because the wind already reached its terminal velocity. The radial component of the magnetic field falls with r^2 and the azimuthal component falls with r , which generates the Parker spiral (Parker, 1958).

Fig. 3.2 shows the wind parameters as a function of distance for the two selected cases. The stellar wind parameter for case A is shown in Fig. 3.2-a and for case B in Fig. 3.2-b. The dashed lines are the outputs from the Alfvén-wave-driven wind simulations and the solid lines are the inputs for the Galactic cosmic ray simulations. The radial velocity profiles are shown in magenta, the radial magnetic field in green, the azimuthal magnetic field in blue and the total magnetic field in red.

In Mesquita & Vidotto (2020), the Alfvén-wave-driven wind is a 1D MHD simulation which does not take into account rotation, for this reason we do not have a B_ϕ profile from the stellar wind simulation. Given that at large distances the azimuthal field should dominate, we use the Parker spiral (Parker, 1958) equation to produce an azimuthal magnetic field component:

$$\frac{B_\phi}{B_r} = \frac{u_\phi - r\Omega}{u_r}, \quad (3.8)$$

where u_ϕ is the azimuthal component of the velocity and Ω is the angular speed of the star. The azimuthal component of the magnetic field only becomes relevant at large distances. Additionally, further out in radius, $u_\phi \ll r\Omega$, and we see from Equation (3.8) that

$$|B_\phi| \simeq \frac{r\Omega}{u_r} B_r. \quad (3.9)$$

We use Equation (3.9) to produce an azimuthal magnetic field for distances beyond the Alfvén radius $r > R_A$ (given in Table 3.2). The total magnetic field profiles for our simulations consist of the vectorial sum of the radial and azimuthal magnetic field components (see red curves of Fig. 3.2).

3.2.3 What is the size of the astrosphere of GJ 436?

The outer boundary of the astrosphere is set by the equilibrium between the pressure of the ISM and the stellar wind ram pressure. The size of the astrosphere is relevant in the context of the interaction of Galactic cosmic rays with a stellar wind (Scherer

3.2 Galactic Cosmic ray propagation

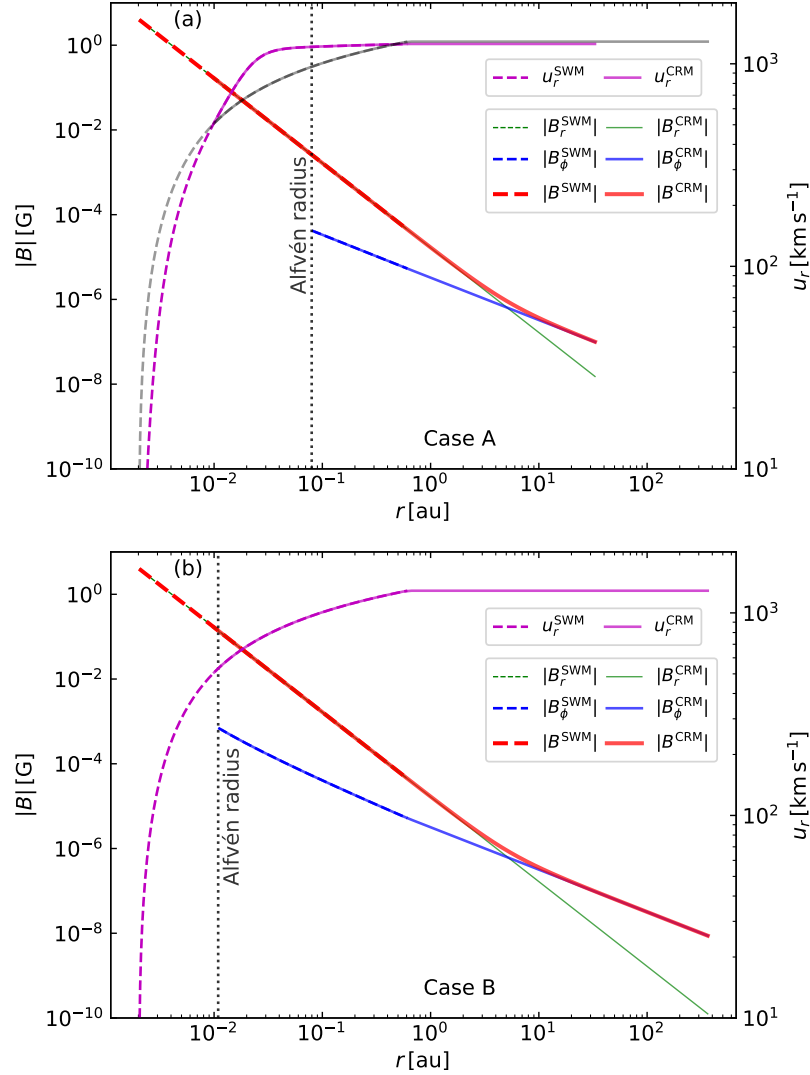


Figure 3.2: Wind parameters as a function of distance for: a) case A (magnetically-dominated) and b) case B (thermally-dominated). The dashed lines are the output from the Alfvén-wave-driven wind simulation and the solid lines are the inputs for the Galactic cosmic ray simulations. The radial velocity profiles are shown in magenta, the radial magnetic field in green, the azimuthal magnetic field in blue and the total magnetic field in red. The grey line on top panel is the velocity profile of case B for comparison. SWM stands for stellar wind model and CRM stands for cosmic ray model.

et al., 2002, 2008; Müller et al., 2006). This is due to the fact that depending on the size of the astrosphere the Galactic cosmic rays will potentially need to travel a further distance through the magnetised stellar wind and may result in higher levels of modulation, depending on the stellar wind properties.

To calculate the size of an astrosphere, we find the point where the ram pressure of the stellar wind balances the ram pressure of the ISM. The stellar wind ram pressure

is given by:

$$P_{\text{ram}} = \rho u^2, \quad (3.10)$$

where ρ is the mass density and u is the velocity of the wind. At large distances, where the wind has reached terminal speed, the density of the stellar wind falls with r^2 and the stellar wind ram pressure follows the same trend. The distance to the astropause can be estimated as

$$R_{\text{ast}} = \left(\frac{P_{\text{ram}}(r = R_{\text{ref}})}{P_{\text{ISM}}} \right)^{1/2} R_{\text{ref}} = \left(\frac{P_{\text{ram}}(r = R_{\text{ref}})}{m_p n_{\text{ISM}} \nu_{\text{ISM}}^2} \right)^{1/2} R_{\text{ref}}, \quad (3.11)$$

where $R_{\text{ref}} = 0.6 \text{ au}$ is the reference distance adopted in our work where P_{ram} already falls with r^2 , n_{ISM} is the ISM number density of neutral hydrogen, ν_{ISM} is the ISM velocity as seen by the star and m_p is the proton mass.

The ISM ram pressure around GJ 436 can be estimated using observations of the ISM column density towards GJ 436 (Bourrier et al., 2015). We follow the same approach as Vidotto & Bourrier (2017), in the case of GJ 436: we assume the ISM is homogeneous along the line-of-sight of the star and purely neutral. In this way, the ISM density can be estimated as $n_{\text{ISM}} = N_{\text{ISM}}/d = 0.03 \text{ cm}^{-3}$ (Vidotto & Bourrier, 2017), where $N_{\text{ISM}} = 10^{18} \text{ cm}^{-2}$ is the ISM column density (derived by Bourrier et al., 2015) and the distance to GJ 436 is $d = 10.14 \text{ pc}$. The density in Equation (3.11) is the total density. If we assume the ISM is purely neutral, then the neutral density and the total density are the same. However, if the ISM is partially ionised (which is the more likely scenario, see, e.g., Table 1 in Jasinski et al., 2020), this means that the total density is larger than the neutral density. As a result, the size of the astrosphere given here (for a purely neutral ISM) is an upper limit. We will discuss the effect of the astrospheric size on the cosmic ray flux further in Section 3.3.1. Using Lyman- α reconstruction, Bourrier et al. (2015) found that the ISM absorption towards the line-of-sight of GJ 436, among different possibilities, has a heliocentric radial velocity for the ISM hydrogen most likely associated with the Local Interstellar Cloud (LIC)¹. Using the ISM Kinematic Calculator (Redfield & Linsky, 2008) and the LIC radial velocity from Bourrier et al. (2015), Bourrier et al. (2015) estimate the heliocentric LIC velocity in the direction of GJ 436. With GJ 436 Hipparcos proper motion (van Leeuwen, 2007) and radial velocity (Bourrier et al., 2015), the heliocentric velocity can be calculated. From these assumptions, Vidotto & Bourrier (2017) derive the ISM velocity as seen

¹The LIC is the interstellar cloud surrounding the Sun roughly 5–7 pc across (Redfield & Linsky, 2000).

3.3 Galactic Cosmic Rays in M dwarf systems

by GJ 436 to be $v_{\text{ISM}} = 81 \text{ km s}^{-1}$ and thus we find an ISM ram pressure of $P_{\text{ISM}} \sim 3.3 \times 10^{-12} \text{ dyn cm}^{-2}$.

Using Equation (3.10) and the input parameters (Table 3.1 and Table 3.2) we calculate the stellar wind ram pressure to be $P_{\text{ram A}}(r = 0.6 \text{ au}) \sim 9.3 \times 10^{-9} \text{ dyn cm}^{-2}$ for case A and $P_{\text{ram B}}(r = 0.6 \text{ au}) \sim 1.2 \times 10^{-6} \text{ dyn cm}^{-2}$ for case B.

Using the values of the ISM ram pressure and the stellar wind ram pressure, we estimate the size of the astrosphere of GJ 436 to be 33 au for case A and 363 au for case B. The difference between the size of the astrosphere for the two different cases is due to the wind density for case A being two orders of magnitude smaller than case B. We note that the value calculated in Vidotto & Bourrier (2017) using an isothermal wind model is more similar to the value we calculate for case A.

3.3 Galactic Cosmic Rays in M dwarf systems

3.3.1 Intensity of cosmic rays as a function of the particle's kinetic energy

Here we investigate how the modulation of Galactic cosmic rays around GJ 436 is affected by different stellar wind properties. Fig. 3.3 shows the intensity of Galactic cosmic rays as a function of the particle's kinetic energy for case A (solid lines) and case B (dotted lines) for different distances. The solid black curve is the LIS given by Equation (3.4). Case B has a larger astrosphere which means that the differential intensity of cosmic rays at a given distance will be smaller than for a system with the same wind parameters and a smaller astrosphere. This is noticeable in Fig. 3.3 when we analyse the differential intensity of cosmic rays at 30 au (light blue curves) and 1 au (green curves) for both cases (at large orbital distances the stellar wind properties for case A and B are nearly identical). In these situations the differential intensity of cosmic rays of case A is higher than case B. 30 au is close to the outer boundary for case A, which is why we chose this specific distance. After travelling a short interval, $\sim 3 \text{ au}$ (solid light blue curve of Fig. 3.3), the cosmic rays have almost the same flux as the LIS for case A. On the other hand, for case B after travelling a larger distance, $\sim 333 \text{ au}$ (dotted light blue curve of Fig. 3.3), the cosmic rays lose energy but less than an order of magnitude compared with the LIS. This shows that the size of the astrosphere has a small contribution to the modulation of cosmic rays in the case of GJ 436.

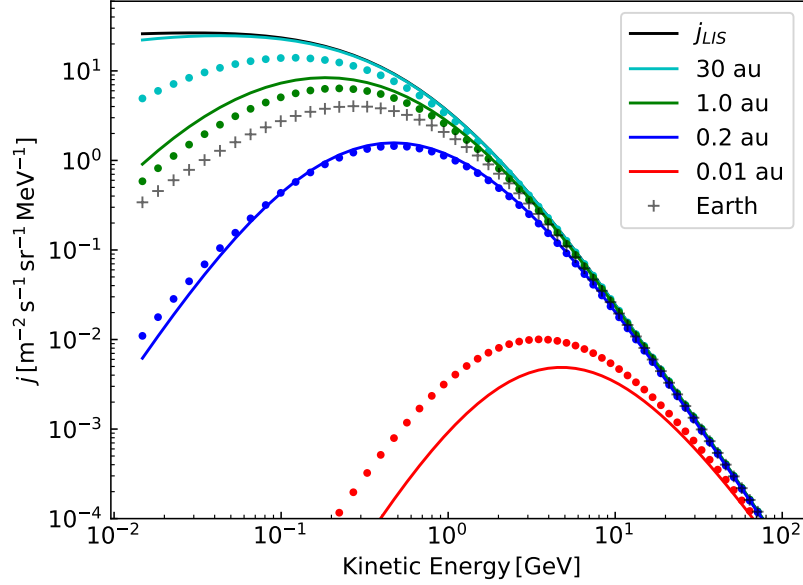


Figure 3.3: Differential intensity of Galactic cosmic rays at different orbital distances for case A (solid lines) and case B (dotted lines). Smaller orbital distances have a much lower intensity of Galactic cosmic rays compared with larger distances. The black solid line is the LIS and grey crosses are representative of the intensity of Galactic cosmic rays observed at Earth at solar minimum (Rodgers-Lee et al., 2020).

The radial velocity profile of case A is slightly higher (by a factor $\lesssim 1.4$) than case B for distances smaller than 0.45 au (compare the grey and pink lines in Fig. 3.2-a). Due to the combination of the velocity profile and the size of the astrosphere, at around 0.2 au the intensity of cosmic rays is equivalent for both cases (see Fig. 3.3 blue lines). For smaller distances (< 0.2 au), case A modulates the cosmic rays more than case B because of the higher velocity of the wind for case A. If the stellar wind velocity is larger it suppresses the flux of Galactic cosmic rays more.

3.3.2 Advective and diffusive timescales

The modulation of Galactic cosmic rays in the system can be understood by analysing the advective and diffusive timescales. The timescales are defined as:

$$\tau_{\text{adv}} = \frac{r}{u}, \quad \tau_{\text{dif}} = \frac{r^2}{\kappa} \propto \frac{r^2}{p/B}. \quad (3.12)$$

The advective timescale depends only on the stellar wind velocity while the diffusion timescale depends on the momentum of the cosmic rays and the magnetic field profile of the stellar wind. Fig. 3.4 presents the ratio between the advective and the diffusive timescales as a function of distance for case A (solid lines) and case B (dotted lines)

3.3 Galactic Cosmic Rays in M dwarf systems

for different values of cosmic ray kinetic energy. The pink shaded area ($\tau_{\text{adv}}/\tau_{\text{dif}} < 1$) indicates the region where advection dominates and the blue shaded area ($\tau_{\text{adv}}/\tau_{\text{dif}} > 1$) indicates the area where diffusion dominates. If diffusion strongly dominates the Galactic cosmic rays experience little (if any) modulation. When timescales are comparable ($\tau_{\text{adv}}/\tau_{\text{dif}} \sim 1$) both effects start to compete and the Galactic cosmic rays start to experience modulation. On the other hand, if advection dominates the Galactic cosmic rays are strongly modulated by the stellar wind.

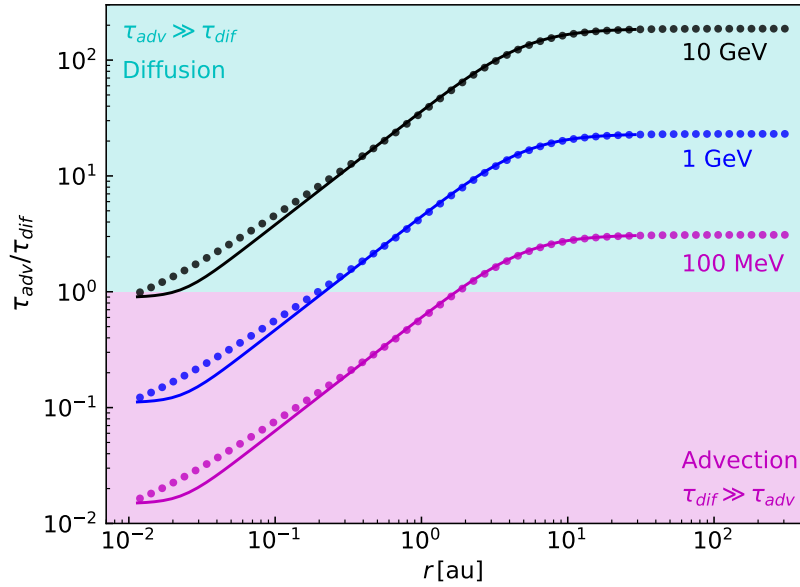


Figure 3.4: Ratio between advective timescale and diffusive timescale as a function of distance from the star for case A (solid lines) and case B (dotted lines). In the blue region, the dominate physical process is diffusion. In the pink region, Galactic cosmic rays are strongly modulated by advection.

The diffusion timescales have the same values for both cases because they have the same magnetic field profile. On the other hand, the advective timescale is slightly different due to the difference in the wind velocity profile of each case. Consequently, the ratio between the timescales is different between both cases which is only noticeable for smaller radii ($r < 0.45$ au).

The timescale ratio can be written as

$$\frac{\tau_{\text{adv}}}{\tau_{\text{dif}}} \propto \frac{p}{ruB} \propto \frac{p}{u} \frac{r^\alpha}{r},$$

where r^α comes from the magnetic field profile as $B \propto 1/r^\alpha$. The radial component of the magnetic field falls with r^2 , hence is best represented by $\alpha \sim 2$. The azimuthal component of the magnetic field falls with r and it is best represented by $\alpha \sim 1$. For

distances $r \leq 10$ au, $\alpha \sim 2$ (see Fig. 3.2 green and red curves) and the timescale ratio is $\propto pr/u$. For distances $r \geq 10$ au, $\alpha \sim 1$ (see Fig. 3.2 blue and red curves) and the timescale ratio is $\propto p/u$. Both trends can be observed in Fig. 3.4, where the timescale ratio increases with distance for $r \leq 10$ au and it becomes constant for $r \geq 10$ au.

For distances smaller than 0.2 au the timescale ratio of case B is higher than case A, for a given energy. When $r < 0.2$ au, we have $u_A > u_B$ and consequently $\tau_{\text{adv B}} > \tau_{\text{adv A}}$. Consequently case A modulates the Galactic cosmic rays more than case B in this region. For distances larger than 0.2 au both cases show a similar value for the timescales.

From Fig. 3.4 we observe that higher energy (10 GeV, black lines) cosmic rays are unmodulated because their diffusive timescale is much smaller than the advective timescale. In other words, they can diffuse faster in the stellar system than the advective processes can act to suppress them. Low energy cosmic rays (100 MeV, magenta lines) are more modulated by the stellar wind because their diffusive timescale is much larger than the advective timescale. This means that stellar winds are more effective at modulating low energy Galactic cosmic rays than high energy ones.

The modulation of Galactic cosmic rays is stronger for low energy cosmic rays (< 1 GeV) and less effective for high energy cosmic rays (> 1 GeV) because the diffusive timescale depends inversely on the momentum of the cosmic rays. The more energetic cosmic rays are not modulated by the stellar wind which can be observed by the fact that all curves (except red curves) in Fig. 3.3 are the same as the LIS (the LIS spectrum is by definition unmodulated) for energies greater than 5 GeV. In contrast, high energy cosmic rays begin to be modulated at small orbital distances as can be observed by the red curves in Fig. 3.3. In fact, Galactic cosmic rays of all energies that we consider are strongly modulated for small distances which can be explained by the fact that the stellar wind magnetic field is much stronger close to the star leading to large diffusion timescales in combination with a small advective timescale.

3.3.3 The intensity of Galactic cosmic rays in the habitable zone and at GJ 436 b

The region around a star where it is possible for a planet to have liquid water on its surface is called the habitable zone (Kasting et al., 1993; Selsis et al., 2007). The differential intensity of Galactic cosmic rays in the habitable zone of GJ 436 (0.2–0.4 au)¹ is shown in Fig. 3.5 as a function of cosmic ray kinetic energy, where blue is

¹The habitable zone was calculated based on Kasting et al. (1993) and Selsis et al. (2007) by assuming an Earth-like exoplanet with the same albedo and the same greenhouse effect as the Earth.

3.3 Galactic Cosmic Rays in M dwarf systems

for case A and red for case B. The black line is the LIS and the green points are the flux of Galactic cosmic rays observed at Earth (Rodgers-Lee et al., 2020).

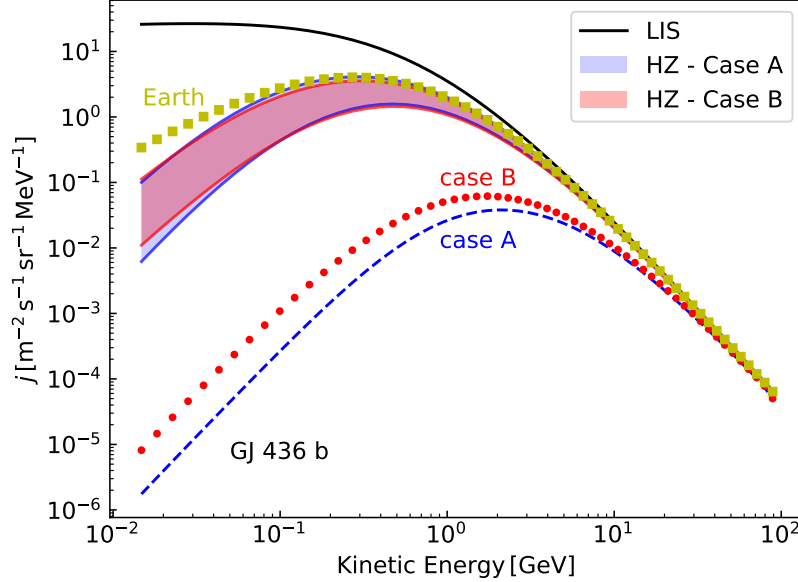


Figure 3.5: Differential intensity of Galactic cosmic rays in the habitable zone of GJ 436 using case A (blue shaded area) and case B (red shaded area) and at the orbital distance of GJ 436 b (0.028 au) for case A (dashed line) and case B (dotted line). The yellow squares is representative of the intensity of Galactic cosmic rays observed at Earth at solar minimum (Rodgers-Lee et al., 2020).

Overall, the flux of cosmic rays in the habitable zone of GJ 436 is very similar for both cases, with case B presenting a slightly higher level of modulation than case A. This result is due to a combination of the velocity profile and the astrosphere size of the cases studied here. The similar results we found here is possibly a coincidence, which would not happen if we choose another stellar wind model (see Section 3.4 for further discussion). In addition, the flux of Galactic cosmic rays in the habitable zone is comparable with values observed at Earth for both cases studied here, even though the habitable zone around GJ 436 is at much smaller distances than the solar habitable zone.

Since GJ 436 hosts a planet, we further investigate the differential intensity of cosmic rays reaching the orbital distance of GJ 436 b (0.028 au). The results are shown in Fig. 3.5 as a function of cosmic ray kinetic energy. Because the planet orbits at such a close distance, case A (blue dashed line) shows a higher modulation of cosmic rays when compared with case B (red dotted line). The difference is more pronounced when we analyse low energy particles (< 1 GeV). We also present in Fig. 3.5 the flux

of Galactic cosmic rays at Earth’s orbit (green solid line) as a function of cosmic ray kinetic energy for comparison (see Figure A1 from Rodgers-Lee et al., 2020). When compared with the Earth, GJ 436 b is exposed to far fewer Galactic cosmic rays than the present-day Earth.

We provide here an analytical expression for the Galactic cosmic ray intensity at the habitable zone of GJ 436 and at the orbit of GJ 436 b. This analytical expression can be used in other works where the flux of cosmic rays is considered an input (e.g., calculating the flux of cosmic rays through planetary magnetospheres and atmospheres). The force field approximation (Gleeson & Axford, 1968) is a theory-based, analytic expression that can be used to describe the modulation of Galactic cosmic rays. This expression depends only on a modulation potential ϕ . Here, we use a modified force field approximation (Rodgers-Lee et al., 2020) for the differential intensity of Galactic cosmic rays in the habitable zone of GJ 436, given by:

$$\frac{j(T)}{E^2 - E_p^2} = \tilde{\beta} \left(\frac{j_{\text{LIS}}(T + \phi)}{(E + \phi)^2 + E_p^2} \right), \quad (3.13)$$

where $E = \sqrt{(pc)^2 + E_p^2}$ is the total proton energy, $E_p = 0.938$ GeV is the proton rest energy and ϕ is the average energy lost by a cosmic ray coming from infinity, i.e. the ISM. The modified force field approximation (Equation (3.13)) has an extra factor of $\tilde{\beta}$ in comparison to the force field approximation which acts to suppress low energy cosmic rays more. The values of ϕ which fit our data well are given in Table 3.2. The modified force field approximation can be used to easily reproduce the Galactic cosmic ray spectrum in the habitable zone of GJ 436 and at the orbit of GJ 436 b. For the former, the modified force field approximation is only appropriate for energies above 200 MeV, as it overestimated the low energy cosmic ray fluxes by 10 times at 0.015 GeV, while for the latter, the approximation should only be used above 1 GeV, as it can overestimate the flux by a factor of up to ~ 2 orders of magnitude at 0.015 GeV.

3.4 Discussion

When modelling the propagation of Galactic cosmic rays inside a stellar astrosphere there are some key parameters that influence the modulation of Galactic cosmic rays. Here, we discuss how the parameters used in our simulations could possibly affect the Galactic cosmic ray propagation and how our work compares with other work in the literature. We also suggest possible future plans.

3.4 Discussion

From the many stellar wind models available from Mesquita & Vidotto (2020), there is a set which is compatible with X-ray observations of GJ 436. This set has stellar wind base densities $< 7 \times 10^{-15} \text{ g cm}^{-3}$ and stellar magnetic fields varying from 1 to 10 G, resulting in $\dot{M} < 7.6 \times 10^{-15} M_{\odot}/\text{yr}$. From their models, we chose only two with similar velocity and magnetic field profiles but that are in a different wind regime and thus have very distinct mass-loss rates (and stellar wind densities). The magnetically-dominated wind (case A) is one of the models that is compatible with observations, as it predicts X-ray luminosities that are below values observed for GJ 436 (Ehrenreich et al., 2015), and gives rise to a mass-loss rate more compatible with other calculated values (see discussion in Mesquita & Vidotto, 2020). Case B, on other hand, is not compatible with such observations. In spite of substantial differences in wind mass-loss rates, our two selected wind models gave rise to a similar modulation of Galactic cosmic rays in the habitable zone of GJ 436 which may indicate that our lack of knowledge on the stellar wind regime is not important for this study.

However, there is still the question of whether our choice of models *coincidentally* led to similar results. If we had selected another stellar wind model, would it have resulted in a different modulation of Galactic cosmic rays? For instance, a stronger stellar magnetic field leads to longer diffusive timescales, which allows the advective processes to dominate (for a given fixed velocity profile), thus, generating more modulation. A higher stellar wind velocity would also modulate the Galactic cosmic rays further. Additionally, the stellar wind density profile would affect the size of the astrosphere which also affects the modulation of the cosmic rays. Mesquita & Vidotto (2020) gave an upper limit for the mass-loss rate and density for GJ 436, but the magnetic field profile remains unconstrained. One way to constrain the magnetic field of a star is through spectropolarimetric observations (e.g. Morin et al., 2010). However, an observationally-derived magnetic map of GJ 436 is currently not available. A magnetic map would allow us to model the stellar wind in 3D (e.g., Kavanagh et al., 2019) and with that the influence of the magnetic field geometry on the cosmic ray propagation could be studied.

The properties of the ISM (such as density, velocity, temperature and ionisation fraction) are also important for the modulation of Galactic cosmic rays, since it is directly connected with the astrosphere size. Jasinski et al. (2020), following the methodology of Müller et al. (2006), demonstrated the importance of the ISM conditions by showing how it can affect the Galactic cosmic ray propagation around two stellar systems, Kepler-20 and Kepler-88. Using the ISM density and velocity constrained by Jasinski et al. (2020), these authors calculated the ISM ram pressure and found that

the astrosphere sizes for Kepler-20 and Kepler-88 could be in the range 2–63 au and 10–270 au, respectively. Jasinski et al. (2020) found at the orbital distances of Kepler-20f and Kepler-88c that the Galactic cosmic ray fluxes at ~ 100 MeV energies could be ≥ 2 orders of magnitude different due to the astrosphere size variation. Here, we found that the size of the astrosphere did not strongly affect the modulation of Galactic cosmic rays. Our astrosphere size varied due to the different stellar wind conditions rather than the ISM conditions. In our work, an astrosphere ten times larger does not significantly affect the flux of cosmic rays for most radii. At 30 au, for instance, case B has less than half of the flux of cosmic rays with energy of 0.15 GeV in comparison with case A at the same distance. The reason for the discrepancy between the work presented in Jasinski et al. (2020) and our work is related to a different formulation of the diffusion coefficient for the cosmic rays. In contrast with our work, Jasinski et al. (2020) use a spatially constant diffusion coefficient. In our work, the diffusion coefficient scales inversely with the magnetic field, similar to Herbst et al. (2020). We cannot point out which formulation for the diffusion coefficient is more appropriate for GJ 436, or the systems considered in Jasinski et al. (2020), because the spatial variation of the turbulence in these systems is unknown. Our prescription for the diffusion coefficient is based on observations in the solar system. When applying it to the GJ 436 system, we assume that the spatial variation of the turbulence is similar in both systems.

Herbst et al. (2020) calculated the flux of Galactic cosmic rays throughout the astrosphere of three M dwarf stars (V374 Peg, Proxima Centauri and LHS 1140). They found at the orbital distances of Proxima b and LHS 1140 b that the Galactic cosmic rays were not significantly modulated. On the other hand, the Galactic cosmic rays are strongly modulated in the V374 Peg system¹. Our values for GJ 436 b lie between these two extremes. LHS 1140 has a very small astrosphere of 11.3 au, a slow stellar wind and a weak magnetic field which all contribute to the lack of significant Galactic cosmic ray modulation in this stellar system. Proxima Centauri has a weak magnetic field at 1 au in comparison to the solar value at the same distance which leads to larger diffusion coefficients resulting in less modulation of the Galactic cosmic rays. In comparison, V374 Peg has an astrosphere 8500 au in size and a strong magnetic field which leads to the strong modulation of Galactic cosmic rays. These results show the variety between the different M dwarfs when studying the propagation of Galactic cosmic rays. One important point to highlight is that Herbst et al. (2020) used a different prescription for the diffusion coefficients with $\gamma = 5/3$ (corresponding to Kolmogorov-type turbulence),

¹In Fig. 3 of Herbst et al. (2020) the units should read as $\text{m}^{-2} \text{s}^{-1} \text{sr}^{-1} \text{MeV}^{-1}$, instead of $\text{m}^{-2} \text{s}^{-1} \text{sr}^{-1} \text{GeV}^{-1}$ (Herbst, private communication).

normalised at 1 GeV/c. This γ value affects the modulation at all energies. Cosmic rays with momentum < 1 GeV/c are less modulated, in comparison with our adopted value of $\gamma = 1$. Cosmic rays with momenta > 1 GeV/c suffers less modulation, in comparison with $\gamma = 1$ (due to the normalisation occurring at 1 GeV/c). An additional point to note is that Herbst et al. (2020) used the ISM properties from outside the heliosphere as a proxy for the ISM properties of the three M dwarf stars in their study. If we had used the ISM values around the Sun ($v_{\text{ISM}} = 25.7 \text{ km s}^{-1}$ and $n_{\text{ISM}} = 0.1 \text{ cm}^{-3}$), GJ 436's astrosphere would be about 75% larger. Therefore, the values of Herbst et al. (2020) could be different depending on the ISM properties around each star.

Another parameter that may vary is the LIS. In our work we used the LIS values from observations outside the heliosphere made by Voyager. Our assumption comes from the fact that the LIS conditions are believed to be similar throughout the Galactic disk (Strong et al., 2007; Neronov et al., 2017; Prokhorov & Colafrancesco, 2018; Aharonian et al., 2020; Baghmanyant et al., 2020) and that it provides a homogeneous Galactic cosmic ray background. However, the spectrum of cosmic rays could have variations locally (Baghmanyant et al., 2020). Stars close to cosmic ray acceleration regions, such as supernova remnants, can show local variations in cosmic ray spectra and have a larger flux of cosmic rays (Fatuzzo et al., 2006). According to Baghmanyant et al. (2020), the LIS spectrum is representative of the cosmic ray spectrum throughout the Galaxy, except within 100 pc of a cosmic ray accelerator. Since GJ 436 is 10.14 pc away from the solar system, and the Sun is not near any cosmic ray accelerator region, any variation of the LIS is not relevant in the context of this work.

Finally, the list of M dwarf stars which host a planet is quite large (Vidotto et al., 2019) and it opens up the possibility to further investigate the propagation of Galactic cosmic rays through their astrospheres. Since we are most interested in possible habitable planets, a possible future work would be the study of Galactic cosmic rays propagation around M dwarfs with exoplanets in the habitable zone. In addition, M dwarfs with magnetic field measurements would also be good targets since it would give further constraints on the stellar wind properties. Knowing the ISM properties around the star is another important factor which was one of the strengths of choosing GJ 436 as a target.

Since M dwarfs can have strong magnetic fields and have a much closer-in habitable zone it is important to investigate the flux of stellar cosmic rays, which are energetic particles generated by the star. Also, the strong magnetic fields and higher levels of magnetic activity in M dwarfs indicate that they should be efficient at accelerating stellar cosmic rays. Potentially habitable planets would therefore be located closer to

the stellar cosmic ray source. Stellar cosmic rays could play a more important role for close-in planets than Galactic cosmic rays (Segura et al., 2010; Grenfell et al., 2012; Tabataba-Vakili et al., 2016; Fraschetti et al., 2019; Scheucher et al., 2020; Rodgers-Lee et al., 2021a) and should be further investigated in future work. In the context of GJ 436, because it is not very magnetically active, stellar cosmic rays may not be as important as for other stars with stronger activity.

3.5 Conclusions

In this paper we investigated the propagation of Galactic cosmic rays through the astrosphere of the planet-hosting M dwarf system GJ 436. Galactic cosmic ray fluxes are suppressed in an energy-dependent way as they travel through magnetised stellar winds, known as the modulation of Galactic cosmic rays. Our main goal was to calculate the intensity of Galactic cosmic rays in the habitable zone of GJ 436 and at the orbital distance of GJ 436 b and compare it with observations at the Earth. For that, we used a 1D cosmic ray diffusive transport equation to model the modulation of Galactic cosmic rays, including spatial and momentum advection of Galactic cosmic rays by the stellar wind. Given that the stellar wind of GJ 436 is not well constrained, we used two Alfvén-wave-driven stellar wind models from Mesquita & Vidotto (2020) consisting of a magnetically-dominated wind (case A) and a thermally-dominated wind (case B). With this, we were also able to investigate how the stellar wind regime could affect the propagation of Galactic cosmic rays.

The wind models selected for this work have similar velocity and magnetic field profiles but with mass-loss rates two orders of magnitude different. Because of this difference, one model (case B) produced an astrosphere ten times larger than the other model (case A). The two wind cases show different fluxes of Galactic cosmic rays for the same distance. This difference in fluxes, however, is not that large, being less than half an order of magnitude different between cases A and B for the same orbital distance. The difference in both cases only occurs for energies lower than 1 GeV – the fluxes are more similar for higher energies.

For distances larger than 10 au diffusion is the main physical process dominating the cosmic ray propagation, which leads to little modulation of cosmic rays at \sim GeV energies. For these distances, a larger astrosphere results in only slightly lower Galactic cosmic ray fluxes in comparison with a smaller one (comparing the same orbital distance). Between \sim 0.2 au and 1 au the fluxes for the two wind cases begin to converge.

At 0.2 au the fluxes of Galactic cosmic rays are nearly identical for both wind setups. At this orbital distance, we noticed a change in behaviour in the propagation of cosmic rays. For distances larger than 0.2 au, the velocity and magnetic field of the stellar winds are very similar, leading to similar levels of modulation (with slightly lower fluxes for the larger astrosphere system). On the other side, for distances smaller than 0.2 au, the magnetically-dominated wind modulates the Galactic cosmic rays more due to a higher local wind velocity (which leads to a smaller advective timescale).

In the habitable zone of GJ 436 (0.2–0.4 au) the flux of Galactic cosmic rays are comparable to the intensities observed at Earth and are approximately the same for both of our wind setups. We provide an analytical fit to our spectra in the habitable zone of the star in Equation (3.13). This fit can be used to reproduce the Galactic cosmic ray spectrum found in our work. We also analysed the flux of Galactic around GJ 436 b (0.028 au) and found that both wind regimes show a strong modulation of cosmic rays, with values four orders of magnitude smaller than intensities observed at the present-day Earth. The thermally-dominated wind (case B) shows intensities of Galactic cosmic rays twice as high as magnetically-dominated wind (case A). The results found here could be further used to investigate the propagation of Galactic cosmic rays through the magnetosphere and atmosphere of GJ 436 b.

The stellar wind properties such as magnetic field and velocity are very important for cosmic ray propagation. In the case of GJ 436, in particular, our lack of knowledge on the wind regime (more thermally-dominated versus more magnetically-dominated), and consequently on the astrosphere size, do not strongly affect the propagation of Galactic cosmic rays on this system (for our choice of diffusion coefficients).

Acknowledgements

This project has received funding from the European Research Council (ERC) under the European Union’s Horizon 2020 research and innovation programme (grant agreement No 817540, ASTROFLOW). The authors wish to acknowledge the SFI/HEA Irish Centre for High-End Computing (ICHEC) for the provision of computational facilities and support. The authors acknowledge funding from the Provost’s PhD Project award. We thank the anonymous reviewer for their careful reading of our paper and constructive comments.

Galactic cosmic ray propagation through M dwarf planetary systems

Amanda L. Mesquita, Donna Rodgers-Lee, Aline A. Vidotto, Dimitra Atri, & Brian E. Wood.

2022, MNRAS, 509, 2091–2101

Abstract

Quantifying the flux of cosmic rays reaching exoplanets around M dwarfs is essential to understand their possible effects on exoplanet habitability. Here, we investigate the propagation of Galactic cosmic rays as they travel through the stellar winds (astrospheres) of five nearby M dwarfs, namely: GJ 15A, GJ 273, GJ 338B, GJ 411 and GJ 887. Our selected stars each have 1 or 2 detected exoplanets and they all have wind mass-loss rates constrained by Lyman- α observations. Our simulations use a combined 1D magnetohydrodynamic (MHD) Alfvén-wave-driven stellar wind model and 1D cosmic ray transport model. We find that GJ 411 and GJ 887 have Galactic cosmic ray fluxes comparable with Earth’s at their habitable zones. On the other hand, GJ 15A, GJ 273 and GJ 338B receive a lower Galactic cosmic ray flux in their habitable zones. All exoplanets in our sample, with exception of GJ 15A c and GJ 411 c, have a significantly lower flux of Galactic cosmic rays than values observed at the Earth because they orbit closer-in. The fluxes found here can be further used for chemical modelling of planetary atmospheres. Finally, we calculate the radiation dose at the surface of the habitable-zone planet GJ 273 b, assuming it has an Earth-like atmosphere. This planet receives up to 209 times less 15 MeV energy cosmic ray fluxes than values observed at Earth. However, for high-energy cosmic rays (\sim GeV), the difference in flux is only 2.3 times smaller, which contributes to GJ 273 b receiving a significant surface radiation dose of 0.13 mSv/yr (40% of the annual dose on Earth’s surface).

4.1 Introduction

With more than 4,300 exoplanets discovered and confirmed (as of 30 September 2021 on NASA’s exoplanet archive¹) in the last few decades, there is a lot of interest in discovering/determining if any of these exoplanets are habitable. There are many factors affecting the habitability of an exoplanet (see, e.g., Meadows & Barnes, 2018). One key factor is the presence of liquid water on the exoplanet surface. Many factors can influence the presence of surface liquid water on a planet, such as the planet and stellar system properties. The habitable zone is defined as the orbital distances from a star where liquid water can exist on a planet’s surface (Kasting et al., 1993; Selsis et al., 2007). This region is close-in for M dwarfs and further out for F and G dwarfs. Although being in the habitable zone does not necessarily mean that a planet is habitable, this is the first condition thought to be important for habitability.

Currently M dwarfs are the main targets in the search for potential habitable exoplanets. This is because M dwarfs are small, they have low brightness, and consequently, they have a close-in habitable zone. This combination, due to current observational capabilities, makes M dwarfs the best candidates to observe exoplanets in the habitable zone. Additionally, they constitute the majority of stars in our Galaxy (Henry et al., 2006; Winters et al., 2015; Henry et al., 2018). However, the stellar environment of M dwarfs can be very harmful for close-in exoplanets. M dwarfs can produce strong magnetic fields (Morin et al., 2010; Shulyak et al., 2019), and compared with solar-mass stars, they stay magnetically active for a longer duration of their lives (West et al., 2004; Scalo et al., 2007; West et al., 2015; Guinan et al., 2016). Exoplanet habitability can be affected by strong stellar activity (Khodachenko et al., 2007; Vida et al., 2017; Tilley et al., 2019). This is because, strong stellar activity leads to stronger stellar winds (Vidotto et al., 2014a), generates more stellar energetic particles (Griekmeier et al., 2005), stronger flares (Vida et al., 2017; Tilley et al., 2019) and coronal mass ejections (Lammer et al., 2007; Khodachenko et al., 2007), all of which can affect planetary atmospheres and thus their potential to generate life.

In particular, the stellar wind plays an important role in stellar evolution (Johnstone et al., 2015; Matt et al., 2015) and interacts with planets (Vidotto et al., 2011, 2013; Vidotto & Cleary, 2020). For this reason, it is important to understand the properties of stellar winds. M dwarfs, however, have rarefied coronal winds analogous to the solar wind, which makes it difficult to observe them. Fortunately, novel techniques have been developed to characterise the winds of low-mass stars (see review by Vidotto, 2021)

¹<https://exoplanetarchive.ipac.caltech.edu>

providing some constraints on the wind properties, such as, the stellar wind mass-loss rate. These methods include Lyman- α absorption observations (Wood, 2004; Wood et al., 2021, and references therein), X-ray emission (Wargelin & Drake, 2001, 2002), radio emission (Panagia & Felli, 1975; Lim & White, 1996; Fichtinger et al., 2017; Vidotto & Donati, 2017), exoplanet atmospheric escape (Vidotto & Bourrier, 2017; Kislyakova et al., 2019) and slingshot prominences (Jardine & Collier Cameron, 2019). Despite all of these methods being able to provide constraints for a few tens of low-mass stars there are still unknowns related to the stellar wind properties.

In our work, we study the properties of M dwarf winds using numerical simulations and observational constraints from Lyman- α measurements. Here, we assume the M dwarf winds are heated and accelerated by the dissipation of Alfvén waves. We use an Alfvén-wave-driven stellar wind model to understand the stellar wind and calculate its properties, such as, the velocity profile and mass-loss rate (Mesquita & Vidotto, 2020).

One particular aspect of interest in our work is that stellar winds affect the propagation of cosmic rays, which are an important factor that could affect exoplanet habitability. On the one hand, cosmic rays may have been important for the origin of life on Earth and for other exoplanets (Airapetian et al., 2016; Atri, 2016), as they can drive the production of prebiotic molecules (Rimmer et al., 2014; Airapetian et al., 2016; Barth et al., 2021). In contrast, for developed life-forms cosmic rays can damage DNA in cells (Sridharan et al., 2016) and cause cellular mutation (Dartnell, 2011). Thus, large cosmic ray fluxes are harmful for life as we know it (Shea & Smart, 2000). A way to quantify the impact of cosmic rays on life-forms is by calculating the radiation dose on the surface of a planet (Atri, 2020; Atri et al., 2020). In addition to this, cosmic rays can also affect cloud coverage which could affect Earth’s climate (Svensmark & Friis-Christensen, 1997; Shaviv, 2002, 2003; Kirkby et al., 2011; Svensmark et al., 2017). All of these aspects about cosmic rays makes it important to investigate their effects on exoplanets.

There are two populations of cosmic rays: Galactic cosmic rays and stellar cosmic rays generated by the host star. Many works have focused on the impact of stellar cosmic rays fluxes at the Earth (Rodgers-Lee et al., 2021a), on M dwarfs (Fraschetti et al., 2019), on young T-tauri systems (Rab et al., 2017; Rodgers-Lee et al., 2017), on exoplanets’ magnetospheres and atmospheres (Segura et al., 2010; Grenfell et al., 2012; Tabataba-Vakili et al., 2016; Scheucher et al., 2020) and also in the context of star-forming regions (see review by Padovani et al., 2020). In this work, we only consider the effects of Galactic cosmic rays originating from our own Galaxy.

4.2 The stars in our sample

Many studies have investigated the Galactic cosmic ray fluxes at Earth focusing on different ages of the solar system (Scherer et al., 2002, 2008; Müller et al., 2006; Svensmark, 2006; Cohen et al., 2012; Rodgers-Lee et al., 2020) to understand their possible effects on Earth. More recently, Rodgers-Lee et al. (2021b) studied the Galactic cosmic rays fluxes for a well-constrained sample of five Sun-like stars with magnetic field measurements and Lyman- α observations. Some works (Sadovskii et al., 2018; Herbst et al., 2020; Mesquita et al., 2021) have also analysed the Galactic cosmic ray fluxes at exoplanets orbiting M dwarfs.

The interaction between the stellar wind and the interstellar wind forms a bubble shaped region around the star which is dominated by its stellar wind (see Fig. 4.1). This region is called the astrosphere, analogous to the Sun’s heliosphere. When studying the propagation of Galactic cosmic rays, the astrosphere becomes especially relevant – outside this region, the cosmic ray flux has its background level. The astrosphere acts as a barrier to the cosmic rays due to the presence of a magnetised stellar wind. Within the astrosphere, the flux of Galactic cosmic rays is modulated/suppressed in an energy-dependent way by the stellar wind.

In this paper, we investigate the propagation of Galactic cosmic rays through a sample of five M dwarf astrospheres. We focus on M dwarfs that host known exoplanets and have mass-loss rates constrained by Lyman- α observations recently presented in Wood et al. (2021). We perform 1D MHD simulations, using an Alfvén-wave-driven stellar wind model to derive the properties of the winds of the M dwarfs (Mesquita & Vidotto, 2020). We use a 1D model of cosmic ray transport (from Rodgers-Lee et al., 2020) to calculate the spectrum of Galactic cosmic rays within M dwarf astrospheres. This paper is organised as follows: in Section 4.2 we describe the stars in our sample. The stellar wind model and the astrospheric sizes are presented in Section 4.3. The transport model for the cosmic rays is described in Section 4.4. Our results on the Galactic cosmic ray fluxes in the habitable zone and at the exoplanets’ orbits, together with the radiation dose at GJ 273 b’s surface are shown in Section 4.5, followed by our discussion and conclusions in Section 4.6.

4.2 The stars in our sample

We select stars with well-constrained stellar wind ram pressure values from recent Lyman- α observations presented in Wood et al. (2021). Our main targets are M dwarfs because they have been identified as prime targets in the search for bio-signatures from exoplanets (Meadows et al., 2018). Additionally, our sample only contains M dwarfs

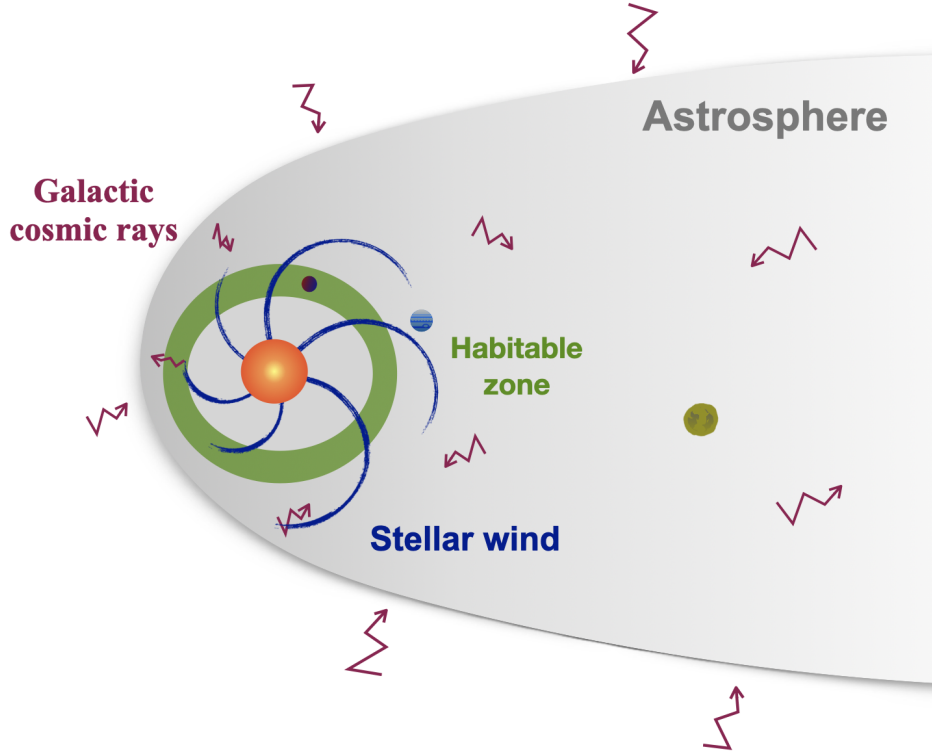


Figure 4.1: Schematic of the stellar system environment studied in this work. The wind generated by the star (large yellow circle) interacts with the interstellar medium (ISM) and creates a “bubble” region called the astrosphere (grey region). The Galactic cosmic rays propagate inside the astrosphere and can interact with the host planets (small circles).

with at least one known orbiting exoplanet. Using these criteria we select five M dwarfs, namely: GJ 15A, GJ 273, GJ 338B, GJ 411 and GJ 887. All of these stars are in close proximity to the solar system, within 7 pc. Table 4.1 presents the stellar properties relevant for our stellar wind simulations, such as radius, mass, distance, rotation period and X-ray luminosity. Table 4.2 summarises the list of known exoplanets in our sample of stars and their properties.

GJ 15A and GJ 338B are wide-orbit binary systems with a second M dwarf. Their orbital separations are 146 au (Pinamonti et al., 2018) and 110 au (González-Álvarez et al., 2020), respectively. However, this is still close enough for each pair to reside within a common astrosphere, meaning the measured wind strength represents the combined wind of both stars (Wood et al., 2021). For the purposes of our work, when simulating the wind and the cosmic ray transport we assume that the wind is being produced by GJ 15A and GJ 338B, because they are the companions with planets.

4.3 The stellar wind environment

Table 4.1: Sample of stars studied in our work. The parameters are from Wood et al. (2021) unless explicitly stated otherwise. The columns are, respectively, star ID, stellar mass, radius, stellar spectral type, rotation period, X-ray luminosity, ISM velocity as seen by the star, mass-loss rate, wind ram pressure, ISM ram pressure and habitable zone boundaries. The last two columns are quantities calculated in our work.

Star	Mass [M_{\odot}]	Radius [R_{\odot}]	Spectral type	P_{rot} [days]	$\log L_X$ [erg s $^{-1}$]	v_{ISM} [km s $^{-1}$]	\dot{M}_{wood} [M_{\odot} yr $^{-1}$]	$P_{\text{ram, wood}}(300 R_{\star})$ [dyn cm $^{-2}$]	P_{ISM} [dyn cm $^{-2}$]	Habitable zone [au]
GJ 15A	0.38 ^a	0.38 ^a	M2 V	44 ^b	27.37	28	2×10^{-13}	6.4×10^{-7}	3.2×10^{-12}	0.12 – 0.31
GJ 273	0.29 ^c	0.293 ^c	M3.5 V	99 ^c	26.54	75	$< 4 \times 10^{-15}$	$< 2.2 \times 10^{-8}$	2.4×10^{-11}	0.08 – 0.20
GJ 338B	0.64 ^d	0.58 ^d	M0 V	16.6 ^d	27.92	29	1×10^{-14}	1.4×10^{-8}	3.4×10^{-12}	0.23 – 0.58
GJ 411	0.386 ^e	0.389 ^e	M2 V	56.2 ^e	26.89	110	$< 2 \times 10^{-15}$	$< 6.1 \times 10^{-9}$	4.7×10^{-11}	0.12 – 0.31
GJ 887	0.489 ^f	0.471 ^f	M2 V	> 200 ^f	27.03	85	1×10^{-14}	2.1×10^{-8}	2.9×10^{-11}	0.16 – 0.40

^aPinamonti et al. (2018); ^bHoward et al. (2014); ^cAstudillo-Defru et al. (2017);

^dGonzález-Álvarez et al. (2020); ^eDíaz et al. (2019); ^fJeffers et al. (2020).

Table 4.2: Properties of the known exoplanets in our sample of stars. The columns are, respectively, planet name, semi-major axis, mass, orbital period and references for the properties.

Planet	a [au]	M_p [M_{\oplus}]	P [days]	References
GJ 15A b	0.072	3.03	11.44	1
GJ 15A c	5.4	36	7600	1
GJ 273 b	0.091	2.89	18.65	2
GJ 273 c	0.036	1.18	4.72	2
GJ 338B b	0.141	10.27	24.45	3
GJ 411 b	0.079	2.69	12.95	4
GJ 411 c	3.10	18.1	3190	5
GJ 887 b	0.068	4.2	9.26	6
GJ 887 c	0.12	7.6	21.79	6

Note. 1 - Pinamonti et al. (2018); 2 - Astudillo-Defru et al. (2017); 3 - González-Álvarez et al. (2020); 4 - Stock et al. (2020); 5 - Rosenthal et al. (2021); 6 - Jeffers et al. (2020).

4.3 The stellar wind environment

4.3.1 The Alfvén-wave-driven wind simulation

To investigate the stellar wind properties for each star in our sample we use 1D time-independent MHD simulations. Similar to the solar wind, we assume the winds of M dwarfs are heated by magnetic processes. Here, the stellar wind is heated and accelerated by the dissipation of Alfvén waves. These waves are generated due to perturbations of the magnetic field lines at the base of the wind. The wind is launched at the base of the chromosphere and the grid extends until $300 R_{\star}$. Note that all the

stars in our sample have reached their terminal velocities by this distance. The model used here is based on the model presented in Mesquita & Vidotto (2020) (see also Vidotto & Jatenco-Pereira, 2010).

The time-independent MHD equations are given as follows:

$$\frac{d}{dr} (\rho u r^2) = 0, \quad (4.1)$$

$$u \frac{du}{dr} = -\frac{GM_\star}{r^2} - \frac{1}{\rho} \frac{dP}{dr} - \frac{1}{2\rho} \frac{d\epsilon}{dr}, \quad (4.2)$$

$$\rho u \frac{d}{dr} \left(\frac{u^2}{2} + \frac{5}{2} \frac{k_B T}{m} - \frac{GM_\star}{r} \right) + \rho u \frac{d}{dr} \left(\frac{F_c}{\rho u} \right) + \frac{u}{2} \frac{d\epsilon}{dr} = Q - P_r, \quad (4.3)$$

where r is the radial coordinate, ρ the wind mass density, u the wind velocity, G the gravitational constant, M_\star the stellar mass, $P = \rho k_B T / m$ the gas pressure, m the average mass of the wind particles, T the wind temperature, ϵ the energy density of the Alfvén waves, F_c the thermal conduction, Q the heating term and P_r is the radiative cooling term. Equations (4.1) to (4.3) are the mass, momentum and energy conservation equations, respectively. The terms on the right-hand side of Equation (4.2) are the gravitational, thermal and mechanical forces, respectively. The terms inside the first parentheses on the left-hand side of Equation (4.3) are the kinetic, enthalpy and gravitational energies per unit mass which are associated with the wind energy. The second term is the conductive energy and the third is the wave energy.

The parameters required in our model are the magnetic field strength and geometry, damping type and length, stellar wind density, temperature and magnetic field perturbation intensity. All the input parameters in our simulations are defined at the base of the chromosphere. We refer the reader to Mesquita & Vidotto (2020), who investigated how these parameters influence the properties of the stellar wind, such as density, velocity, temperature and mass-loss rate. Here, we use a fully radial magnetic field line configuration. We use the same temperature of 10^4 K at the base of the chromosphere for all of the stars. We adopt a non-linear damping mechanism in which the amplitude of the MHD waves decreases with the quadratic amplitude of the fluctuations in the wave velocity, using the approach by Jatenco-Pereira & Opher (1989). We adopt an initial damping length of $0.1 R_\star$ (Mesquita & Vidotto, 2020). The non-linear damping mechanism for the waves has been used in solar wind models (e.g., Suzuki & Inutsuka, 2005; Suzuki et al., 2013). The magnetic field perturbations are taken at the base of the wind as $0.1 B_0$, where B_0 is the magnetic field strength at the base of the wind. The magnetic field perturbation at the base of the wind is a

4.3 The stellar wind environment

free parameter in our simulation that can affect the properties of the stellar wind (see discussion in Mesquita & Vidotto, 2020). The amplitude of the magnetic field fluctuations is connected with the amplitude of velocity fluctuations by energy equipartition (see Equation 5 in Mesquita & Vidotto, 2020). van Holst et al. (2014) used the velocity fluctuations value of 15 km s^{-1} at the chromosphere for a 3D MHD solar simulation. This value agrees with Hinode observations of the 15 km s^{-1} turbulent velocities for the solar wind (De Pontieu et al., 2007). In our simulations, the velocity fluctuations at the base of the wind vary from $9\text{--}23 \text{ km s}^{-1}$ (using the magnetic field perturbations at the base of the stellar wind equal to $0.1 B_0$) which is in good agreement with the works mentioned for the solar wind. We use observations to constrain the magnetic field strength and the density at the base of the stellar wind in our model. The approach used here is explained below.

4.3.1.1 Stellar surface magnetic field

In order to constrain the input magnetic field strength at the base of the chromosphere we use the observed correlation between X-ray luminosity and large scale magnetic flux, $L_X \approx 10^{-13.7} \Phi_V^{1.80 \pm 0.20}$, from Vidotto et al. (2014a). We use the X-ray luminosity given in Table 4.1 to infer the large scale magnetic flux using this relation. Then, we use the relation $\Phi_V = 4\pi R_\star^2 B_0$ to get the average large scale magnetic field strength. This value of B_0 is used as the input magnetic field strength for the stellar wind simulations. The value used for each star is presented in Table 4.3. The stars in our sample are old and not very active, which explains the relatively low magnetic field strength values ($3.1\text{--}7.5 \text{ G}$) found in our work (consistent with recent spectropolarimetric results from Moutou et al., 2017). More active M dwarfs can have kilo Gauss magnetic field strengths (e.g. review by Morin, 2012).

Table 4.3: Stellar wind properties. The columns are, respectively, the star ID, the magnetic field strength and density at the base of the wind (input model parameters), terminal velocity, mass-loss rate, stellar wind ram pressure, Alfvén radius and astrosphere size (output model parameters).

Star	B_0 [G]	ρ_0 [g cm $^{-3}$]	u_∞ [km s $^{-1}$]	\dot{M} [M_\odot yr $^{-1}$]	$P_{\text{ram}}(300 R_\star)$ [dyn cm $^{-2}$]	R_A [au]	R_{ast} [au]
GJ 15A	7.5	2.6×10^{-14}	1100	6.8×10^{-14}	6.2×10^{-7}	0.02	240
GJ 273	4.3	9.8×10^{-15}	880	$< 1.8 \times 10^{-15}$	$< 2.2 \times 10^{-8}$	0.06	12
GJ 338B	6.0	5.5×10^{-15}	940	1.1×10^{-14}	3.6×10^{-8}	0.06	52
GJ 411	3.5	2.4×10^{-15}	1400	$< 6.1 \times 10^{-16}$	$< 6.4 \times 10^{-9}$	0.08	6
GJ 887	3.1	9.6×10^{-15}	850	4.8×10^{-15}	2.1×10^{-8}	0.05	18

4.3.1.2 The base density of the stellar wind

One successful technique used to detect stellar winds of low-mass stars is the detection of Lyman- α absorption (Wood et al., 2021, and references therein). Lyman- α absorption is generated when stellar photons travel through the stellar astrosphere, the ISM and the heliosphere and is detected in UV spectra. With the detection of astrospheric absorption it is possible to determine the ram pressure of the stellar wind, P_{ram} . By knowing the stellar wind asymptotic velocity, u_{∞} , it is possible to determine the mass-loss rate, \dot{M} , using the relation

$$\dot{M} = \frac{4\pi R_{\star}^2 P_{\text{ram}}}{u_{\infty}}. \quad (4.4)$$

On the other hand, if astrospheric absorption is not detected only an upper limit for P_{ram} is obtained. In both cases, the Lyman- α observations are essential to constrain the density at the base of the chromosphere that we use in our stellar wind model.

For that, we vary the value of the density at the base of the wind to reproduce the stellar wind ram pressure inferred from the Lyman- α observations. We match the stellar wind ram pressure, rather than the mass-loss rates presented in Wood et al. (2021), because Wood et al. (2021) assumes the Sun’s terminal wind velocity of 400 km s^{-1} for all the stars. In our simulations, the values we find for u_{∞} are larger. The ram pressures derived from the observationally-inferred mass-loss rates and $u_{\infty} = 400 \text{ km s}^{-1}$ are shown in column ten of Table 4.1 ($P_{\text{ram, wood}}$) – these values are calculated at a reference radius of $300 R_{\star}$. For comparison, we show the ram pressure values that our models produce in Table 4.3 (calculated at the same reference radius). As it can be seen, our values are reasonably similar (i.e., within a factor of 2.6) from the observationally-derived ones. In terms of mass-loss rates, our approach gives lower values than those found in Wood et al. (2021) (see \dot{M}_{wood} in Table 4.1) due to our higher stellar wind terminal velocities. The value of the base density, ρ_0 , used for each simulation is shown in Table 4.3.

4.3.2 Stellar wind density, velocity and magnetic field profiles

The stellar wind properties, such as the magnetic field and velocity profiles, are needed to calculate the Galactic cosmic ray flux reaching an exoplanet. From our Alfvén-wave-driven wind simulations we have the stellar wind velocity profile. However, only the radial component of the magnetic field, B_r , is calculated from our 1D MHD simulations. Thus, to determine the azimuthal component of the magnetic field, B_{ϕ} , we use the

4.3 The stellar wind environment

Parker spiral relation (Parker, 1958):

$$\frac{B_\phi}{B_r} = \frac{u_\phi - r\Omega}{u_r}, \quad (4.5)$$

where u_ϕ is the azimuthal velocity component, $\Omega = 2\pi/P_{\text{rot}}$ is the angular speed of the star and P_{rot} is the stellar rotation period. B_ϕ only dominates at large distances and at these distances, $u_\phi \ll r\Omega$. Thus, Equation (4.5) can be expressed as

$$|B_\phi| \simeq \frac{r\Omega}{u_r} B_r. \quad (4.6)$$

The total magnetic field strength is $B = \sqrt{B_r^2 + B_\phi^2}$, where B_ϕ is given by Equation (4.6) for distances beyond the Alfvén radius, $r > R_A$. The Alfvén radius is defined as the distance where the wind has reached the Alfvén velocity which is given by $v_A = B/\sqrt{4\pi\rho}$.

The outer boundary of the Alfvén-wave-driven wind simulations is at $300 R_\star$, where the wind has already reached its terminal velocity. However, the astrosphere extends further out and we extrapolate the quantities u_r , B_r and B_ϕ to take into account the profiles for the whole astrosphere. Since the velocity reaches its asymptotic value by $300 R_\star$, beyond this distance it has a constant profile. The radial magnetic field component continues to fall with r^2 and the azimuthal component with r , generating the Parker spiral (Parker, 1958).

Fig. 4.2 shows a summary of the stellar wind properties for GJ 273 (left) and GJ 338B (right) to show the different contributions of the magnetic field components. In both panels, the black curve is the velocity profile, the red curve is the total magnetic field, the green curve is the radial magnetic field strength and the blue curve is the azimuthal magnetic field strength. The dotted curves are the results from the Alfvén-wave-driven wind simulations and the solid curves are the profiles used as an input for the cosmic ray simulations. Two planets in our simulations, GJ 273 c and GJ 411 b, lie within the Alfvén radius, in a sub-Alfvénic region.

4.3.3 The size of the M dwarf astrospheres

The outer boundary of the cosmic ray simulation is set to be the astrospheric radius, which varies for the stars in our sample. The size of the astrosphere can be calculated by finding the balance between the stellar wind ram pressure and the ISM ram pressure.

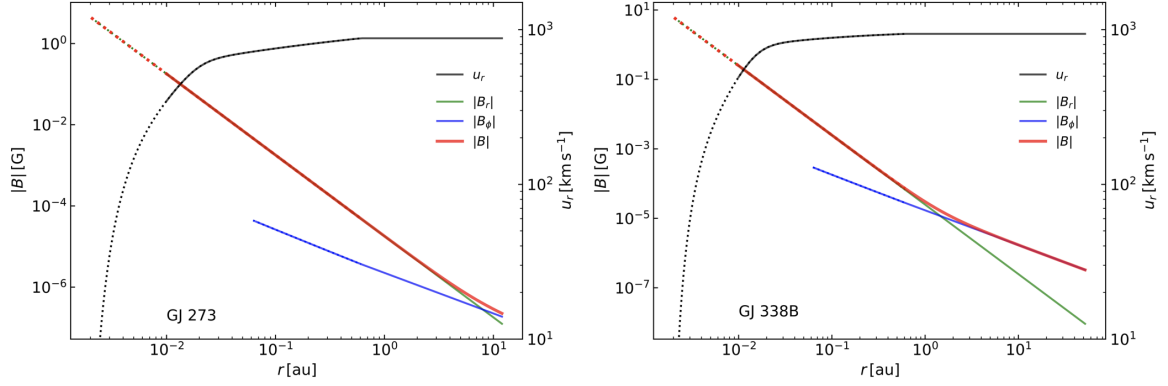


Figure 4.2: Stellar wind properties, such as, velocity (black curves) and magnetic field (total magnetic field red curves, radial magnetic field strength green curves and azimuthal magnetic field blue curves) profiles of left: GJ 273 and right: GJ 338B. The dotted lines are the results obtained from the stellar wind model and the solid lines are the profiles used as input in the cosmic ray model.

The wind ram pressure is given by:

$$P_{\text{ram}} = \rho u^2. \quad (4.7)$$

The ISM ram pressure is given by:

$$P_{\text{ISM}} = m_p n_{\text{ISM}} \nu_{\text{ISM}}^2, \quad (4.8)$$

where m_p is the proton mass, n_{ISM} is the total ISM number density of hydrogen and ν_{ISM} is the ISM velocity as seen by the star.

The ISM ram pressure was calculated using ν_{ISM} for each star as given in Table 4.1. The total ISM number density of hydrogen is given by the sum of neutral hydrogen number density and the ionised hydrogen number density ($n_{\text{ISM}} = n_n + n_i$). We assume that the ISM is partially ionised and we use the values from Wood et al. (2000) that successfully reproduces heliospheric absorption, e.g., Model 10 of Wood et al. (2000), which are $n_n = 0.14 \text{ cm}^{-3}$ and $n_i = 0.1 \text{ cm}^{-3}$, giving $n_{\text{ISM}} = 0.24 \text{ cm}^{-3}$ for all stars in our sample. Using Equation (4.8) we calculate P_{ISM} for each star in our sample, the results are shown in Table 4.1.

The astrospheric size is calculated as:

$$R_{\text{ast}} = \sqrt{\frac{P_{\text{ram}}(R)}{P_{\text{ISM}}}} R, \quad (4.9)$$

where R is a given reference distance where the wind has reached its terminal velocity.

4.4 Cosmic ray transport

The stellar wind ram pressure calculated at $R = 300 R_\star$ is shown in Table 4.3. In general, M dwarfs tend to be an older stellar population due to their long lifetimes (see review by Shields et al., 2016), and consequently, they will on average have higher ν_{ISM} values because as stars pick up more gravitational perturbations with time they acquire larger deviations from the Local Standard of Rest. For this reason, M dwarfs tend to have small astrospheres.

Using Equation (4.9) we calculate the astrospheric size of each star in our sample, the values are shown in Table 4.3. The size of the astrospheres in our sample vary from 6 to 240 au. GJ 411 has the smallest astrospheric size and is a very compact system. In contrast, GJ 15A has a very large astrosphere being almost as twice as large as the present-day heliosphere (~ 122 au, Stone et al., 2013, 2019). Note that for GJ 338B, we obtain a larger astrosphere size of 83 au instead of the 52 au using $P_{\text{ram, wood}}$. This is because our value for P_{ram} is around 2.6 times larger than the value $P_{\text{ram, wood}}$ ¹.

4.4 Cosmic ray transport

As Galactic cosmic rays propagate through a magnetised stellar wind they suffer global variations in their intensity and energy which is known as the modulation (or suppression) of cosmic rays. The modulation of cosmic rays can be obtained by solving the diffusion-advection transport equation of Parker (1965). The model we use was presented in Rodgers-Lee et al. (2020) and was previously applied to the M dwarf, GJ 436 (Mesquita et al., 2021). We numerically solve the time-dependent transport equation

$$\frac{\partial f}{\partial t} = \nabla \cdot (\kappa \nabla f) - u \cdot (\nabla f) + \frac{1}{3}(\nabla \cdot u) \frac{\partial f}{\partial \ln p}, \quad (4.10)$$

where $f(r, p, t)$ is the cosmic ray space phase density, r is the radial distance, p is the cosmic ray momentum and u is the stellar wind velocity. The first term on the right-hand side of Equation (4.10) represents the diffusion of the cosmic rays which depends on the diffusion coefficient, $\kappa(r, p)$. The second term is the advection of the cosmic rays which depends on the stellar wind velocity, u , and acts against the inward diffusion of the cosmic rays. The third term is the adiabatic losses due to the stellar wind expansion².

¹We found that this difference in the astrospheric size of GJ 338B does not strongly affect the Galactic cosmic ray fluxes for the system. A similar situation was also observed in the GJ 436 stellar system (discussed in Mesquita et al., 2021).

²Here, we do not take into account ionisation losses because the cosmic rays do not have a lot of material to cross when travelling in the astrosphere of the M dwarfs in our sample. This is because the column density of stellar wind material is small. For instance, for GJ 436 we calculated, using the

Stellar wind magnetic field (via the diffusion coefficient) and velocity profiles are key ingredients for the modulation of Galactic cosmic rays, as given by Equation (4.10). The stellar wind density profile is relevant to define the size of the astrosphere. However, it does not lead to any significant attenuation of the cosmic rays, as the stellar wind density is very low.

Our spatial and momentum grids are logarithmically spaced with 60 grid zones each. The spatial inner boundary is 0.01 au and the outer boundary is set as the astrospheric size of each star in our sample (see Table 4.3). The momentum range that we consider for our simulations is $p_{\min} = 0.15 \text{ GeV}/c$ and $p_{\max} = 100 \text{ GeV}/c$. The upper limit for the momentum was selected because particles with energies above this limit are very infrequent and are not relevant in the context of planetary atmosphere chemistry (Rimmer & Helling, 2013). The lower limit was selected because particles with low energies ($\lesssim 290 \text{ MeV}$, i.e. the pion threshold energy) do not reach the planetary surface (Atri, 2017) and do not contribute to the radiation dose calculated there (this will be calculated in Section 4.5.2). However, the low-energy particles are important in the context of planetary atmospheres because they deposit all of their energy there (Rodgers-Lee et al., 2020) and could be included in future chemical modelling studies.

4.4.1 Diffusion coefficient

As Galactic cosmic rays penetrate a stellar astrosphere their intensity is reduced due the presence of a magnetised stellar wind. The diffusion of the cosmic rays depends on the turbulence level of the magnetic field. The presence of magnetic field irregularities makes the cosmic ray undergo a random walk in the system. The diffusion coefficient of the cosmic rays, from quasi-linear theory (Jokipii, 1966; Schlickeiser, 1989), can be expressed as

$$\frac{\kappa(r, p)}{\beta c} = \eta_0 \left(\frac{p}{p_0} \right)^{1-\gamma} r_L, \quad (4.11)$$

where $\beta = v/c$ is the ratio between the particle velocity and the speed of light, $p_0 = 3 \text{ GeV}/c$, $r_L = p/eB(r)$ is the Larmor radius of the protons. η_0 depends on the level of turbulence in the magnetic field. We adopt $\eta_0 = 1$ which represents the maximum level of turbulence for the magnetic field. γ determines how the diffusion coefficient varies with momentum. We adopt $\gamma = 1$, which corresponds to Bohm diffusion. This value is commonly used in other works (Svensmark, 2006; Cohen et al., 2012; Rodgers-Lee et al., 2020) and is in good agreement with observations at Earth. There are different

stellar wind density, that the column density of stellar wind material is $2.8 \times 10^{-7} \text{ g cm}^{-2}$.

prescriptions for γ , such as, the Kolmogorov-type turbulence ($\gamma = 5/3$, as in Herbst et al., 2020) and magnetohydrodynamic-driven turbulence ($\gamma = 3/2$). The type of turbulence for M dwarf systems is currently unknown. The turbulence type can affect the cosmic ray spectrum for all energies. For instance, for Kolmogorov-type turbulence normalised at 1 GeV/c, Mesquita et al. (2021) found that cosmic rays with momentum <1 GeV/c are less modulated when compared with Bohm-type turbulence. On the other hand, cosmic rays with momentum >1 GeV/c are more modulated.

4.4.2 Local Interstellar Spectrum (LIS)

In the ISM there is a “sea” of Galactic cosmic rays, unaffected by the presence of the magnetised stellar wind. This value sets the background flux of Galactic cosmic rays that can penetrate the stellar systems.

The unaffected background spectrum of Galactic cosmic rays was observed by *Voyager 1*, after it crossed the heliopause (Stone et al., 2013; Cummings et al., 2016). In our simulations, we use the fit to the local interstellar spectrum (LIS) from Vos & Potgieter (2015) to describe the unaffected spectrum of Galactic cosmic rays that can be injected in our system. Using *Voyager 1* observations, Vos & Potgieter (2015) developed a model fit to describe the LIS:

$$j_{\text{LIS}}(T) = 2.70 \frac{T^{1.12}}{\beta^2} \left(\frac{T + 0.67}{1.67} \right)^{-3.93} \text{ m}^{-2} \text{ s}^{-1} \text{ sr}^{-1} \text{ MeV}^{-1}, \quad (4.12)$$

where j is the differential intensity of cosmic rays and T is the kinetic energy of the cosmic rays in GeV. In our simulations, the LIS is considered constant as a function of time. Note, the differential intensity can be expressed in terms of the phase space density, f in Equation (4.10), as $j(T) = p^2 f(p)$.

γ -ray observations, which trace $\sim 10 - 10^4$ GeV cosmic rays, within 1 kpc in the local Galaxy inferred the Galactic cosmic ray spectrum to be in a good agreement with *Voyager* measurements in the local ISM (Neronov et al., 2017). However, ionisation rates inferred from observations of diffuse molecular clouds (see discussion in Recchia et al., 2019; Padovani et al., 2020), which trace lower energy cosmic rays (\lesssim GeV), indicate that there are more low-energy cosmic rays present in these clouds than is measured by *Voyager* in the local interstellar medium. This could be due to low-energy cosmic rays from young stars close to the molecular clouds. However, the stars in our sample are all nearby stars within 7 pc of the solar system. Thus, adopting the LIS for our sample is a good assumption.

We also note that, if low energy cosmic rays were more abundant than the LIS it is unlikely to affect the radiation dose calculated in our paper for the surface of GJ 273 b (see Section 4.5.2). In addition, close-in exoplanets (such as the ones we have in our sample) would not be affected by low energy cosmic rays because they are suppressed strongly by advective processes. This might not be the case for planets that orbit further out.

4.5 Galactic cosmic ray fluxes around M dwarfs

4.5.1 The flux of Galactic cosmic rays at the habitable zone and at planetary orbits

The habitable zone depends on the planetary mass and atmospheric conditions. In this work we calculate the habitable zone size using the prescription of Kopparapu et al. (2014), where the distance in au is given by

$$d = \sqrt{\frac{L/L_{\odot}}{S_{\text{eff}}}}, \quad (4.13)$$

where L/L_{\odot} is the stellar bolometric luminosity compared with the solar luminosity and S_{eff} is the stellar effective flux incident on the top of the planet's atmosphere, given by

$$S_{\text{eff}} = S_{\text{eff}\odot} + aT_{\star} + bT_{\star}^2 + cT_{\star}^3 + dT_{\star}^4, \quad (4.14)$$

where $T_{\star} = T_{\text{eff}} - 5780 \text{ K}$. The coefficients in Equation (4.14) are given by the recent Venus and early Mars limits in Table 1 of Kopparapu et al. (2014) for planets with $0.1 M_{\oplus} \leq M_{\text{planet}} \leq 5 M_{\oplus}$. The habitable zone boundaries that we calculate are given in Table 4.1. With this prescription, only one exoplanet (GJ 273 b) lies in the habitable zone, with GJ 887 c lying very close (at 0.12 au) to the inner edge of the habitable zone (at 0.16 au).

Fig. 4.3 shows the differential intensity of cosmic rays as a function of kinetic energy in the habitable zone (green shaded areas), at planet b orbit (blue curves) and at planet c orbit (yellow curves) for each star in our sample and GJ 436 (case A from Mesquita et al., 2021). For each panel, the solid black line is the LIS and the grey dots are representative of the Galactic cosmic ray spectrum observed at Earth's orbit, representative of solar minimum values (taken from a model from Rodgers-Lee et al., 2020). With the exception of GJ 15A c and GJ 411 c all the planets in our sample receive a lower flux of cosmic rays in comparison with Earth (see Fig. 4.3) for all kinetic

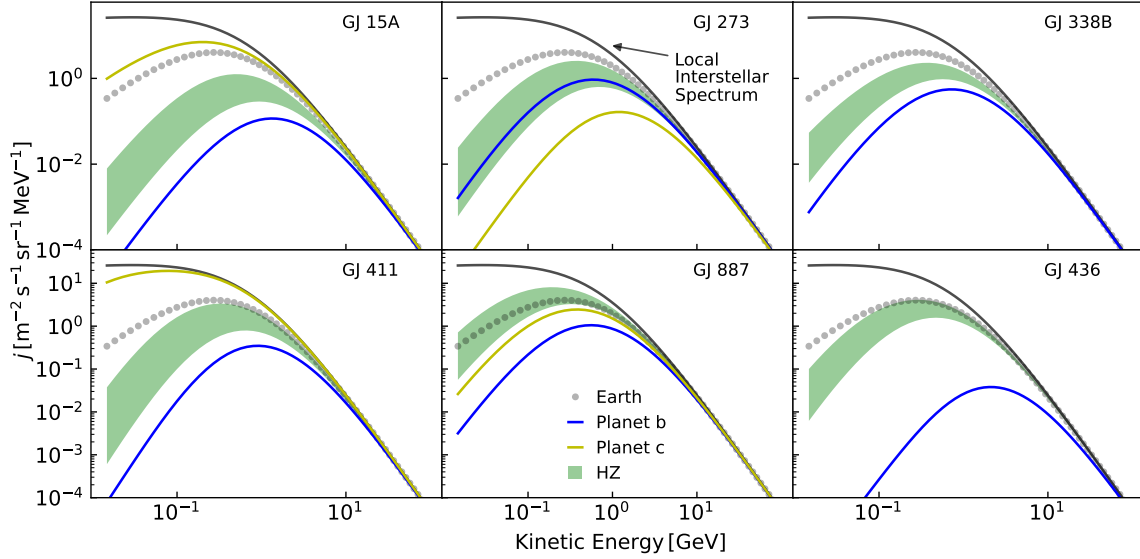


Figure 4.3: Differential intensity of Galactic cosmic rays as a function of kinetic energy for six M dwarfs. The green shaded areas are the flux of cosmic rays in the habitable zone of each star. The blue and yellow lines are the fluxes of cosmic rays at planets b and c orbital distances, respectively. The grey dots in each panel is the Galactic cosmic rays fluxes observed at Earth and the black line is the LIS.

energies because they orbit close-in. In particular, we observe a strong suppression of low-energy cosmic rays at the majority of exoplanets orbit. Galactic cosmic ray fluxes are seen to continue decreasing for close-in distances for the Sun as well (during solar minimum observations from Marquardt & Heber, 2019). However, the solar observations also capture temporal variations that we do not take into account in our work. For example, our model neglects velocity drift terms and is most applicable to solar minimum conditions (when the velocity drift term is minimal).

The bottom panels of Fig. 4.3 show that two stars in our sample have Earth-like Galactic cosmic ray fluxes in their habitable zones, namely GJ 887 and GJ 411, although GJ 411 is only comparable for cosmic rays with energies above 0.4 GeV energies. GJ 436 also has comparable Galactic cosmic ray fluxes at its habitable zone for energies larger than 0.1 GeV. Interestingly, GJ 273 b, which is the only exoplanet in our sample in the habitable zone, receives a much lower (up to two orders of magnitude) flux of Galactic cosmic rays when compared with the values at Earth. We will come back to this planet when we calculate the biological surface radiation dose in the next subsection.

Fig. 4.4 shows the flux of GeV energy Galactic cosmic rays as a function of semi-major axis for each planet in our sample and the Earth. We chose 1 GeV energy cosmic

rays because particles with this energy can penetrate exoplanetary atmospheres, as they do not lose as much energy as low-energy cosmic rays. Almost all the planets in our sample have a very small semi-major axis, with exception of GJ 15A c and GJ 411 c. For a given star, the Galactic cosmic ray fluxes decrease with decreasing orbital distance. Thus, a closer-in planet receives lower Galactic cosmic rays fluxes in comparison to a planet with a larger semi-major axis. We identify that different wind parameters may coincidentally lead to similar levels of Galactic cosmic rays for different planetary systems (see Fig. 4.4 planets GJ 273 b (D) and GJ 887 b (H), for instance).

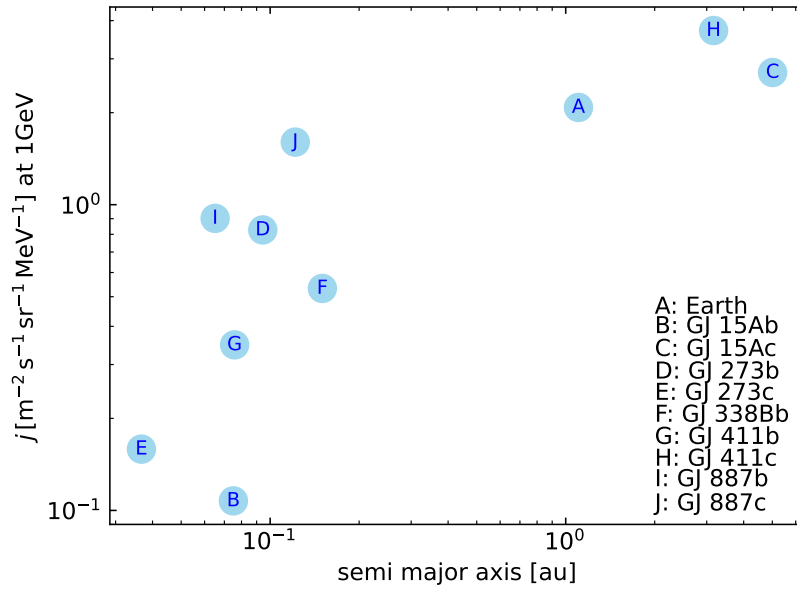


Figure 4.4: Galactic cosmic ray flux at semi-major axis of each planet for particles with 1 GeV kinetic energy. Most of the planets orbiting the M dwarfs studied here have a very small semi-major axis with exception of GJ 15Ac and GJ 411 c.

Here, we focused only on Galactic cosmic rays but active stars with strong magnetic fields should be efficient in accelerating energetic particles or stellar cosmic rays (Rodgers-Lee et al., 2021a). Similarly to Galactic cosmic rays, stellar energetic particles can also interact/affect exoplanets' magnetospheres, atmospheres and surface (Segura et al., 2010; Grenfell et al., 2012; Tabataba-Vakili et al., 2016; Frascchetti et al., 2019; Scheucher et al., 2020). In addition, because M dwarfs have close-in habitable zones and several observed close-in exoplanets, it is expected that at those distances the stellar cosmic rays may dominate up to a given energy.

4.5.2 GJ 273 b’s surface radiation dose

GJ 273 b is a super-Earth orbiting in the habitable zone at a distance of 0.091 au. Its mass is $2.89 M_{\oplus}$ and it has an orbital period of 18.6 days (Astudillo-Defru et al., 2017). It receives an incident bolometric flux of 1.06 times that received at Earth (Astudillo-Defru et al., 2017). In addition to the presence of surface liquid water, GJ 273 b could be potentially habitable if an atmosphere is present. Here, assuming an Earth-like atmosphere, we investigate the biological radiation dose that reaches GJ 273 b’s surface.

The biological radiation dose is modelled using the GEANT4 package (Agostinelli et al., 2003). It is a Monte Carlo code developed at CERN to model charged particle interactions with matter and is extensively calibrated and used worldwide. For simplicity, we assume that GJ 273 b has an Earth-like atmosphere and has no global magnetic field. We use the standard Earth’s atmosphere as used in the earlier studies (Atri, 2017, 2020) incident with isotropic flux of particles ranging from energies corresponding to our assumed p_{\min} and p_{\max} values. The radiation dose is calculated on an ICRU (International Commission on Radiation Units and Measurements) sphere-equivalent of 15 cm radius on the surface of the planet consisting of 100% water, assuming that life if it exists on the planet it is likely to be water-based. We obtain a dose equivalent rate of 4.12×10^{-12} Sv/s, which is 0.13 mSv/yr. For comparison, the annual dose equivalent on the Earth’s surface is around 0.33 mSv (according to the National Council on Radiation Protection and Measurements report No 160). Even though the 15 MeV Galactic cosmic ray flux at GJ 273 b is about 200 times smaller than at Earth, the difference in flux is smaller at energies of a few 100 MeV and above, which is the part that contributes most to the radiation dose at the surface. Lower energy particles deposit energy in the top of the atmosphere, and do not contribute to the radiation dose on the surface.

As mentioned in the Section 4.5.1, active stars can also generate stellar cosmic rays. Stellar cosmic rays with energies $\gtrsim 100$ MeV may also contribute to the radiation dose at the planetary surface and particles with energies $\lesssim 100$ MeV can ionise the planet’s atmosphere.

4.5.3 How are Galactic cosmic rays modulated by the magnetised wind of M dwarfs?

Here we investigate how Galactic cosmic rays are modulated by the stellar winds of different M dwarfs. We divided our sample of stars in two main group according to their

radial magnetic field/rotation period. Group 1 includes: GJ 273, GJ 411 and GJ 887 which have longer rotation periods and smaller radial magnetic field strengths. Group 2 includes: GJ 15A and GJ 338B which have shorter rotation periods and larger radial magnetic field strengths when compared with group 1. Fig. 4.5 shows the differential intensity of Galactic cosmic rays as a function of cosmic ray kinetic energy for group 1 (Fig. 4.5a) and group 2 (Fig. 4.5b).

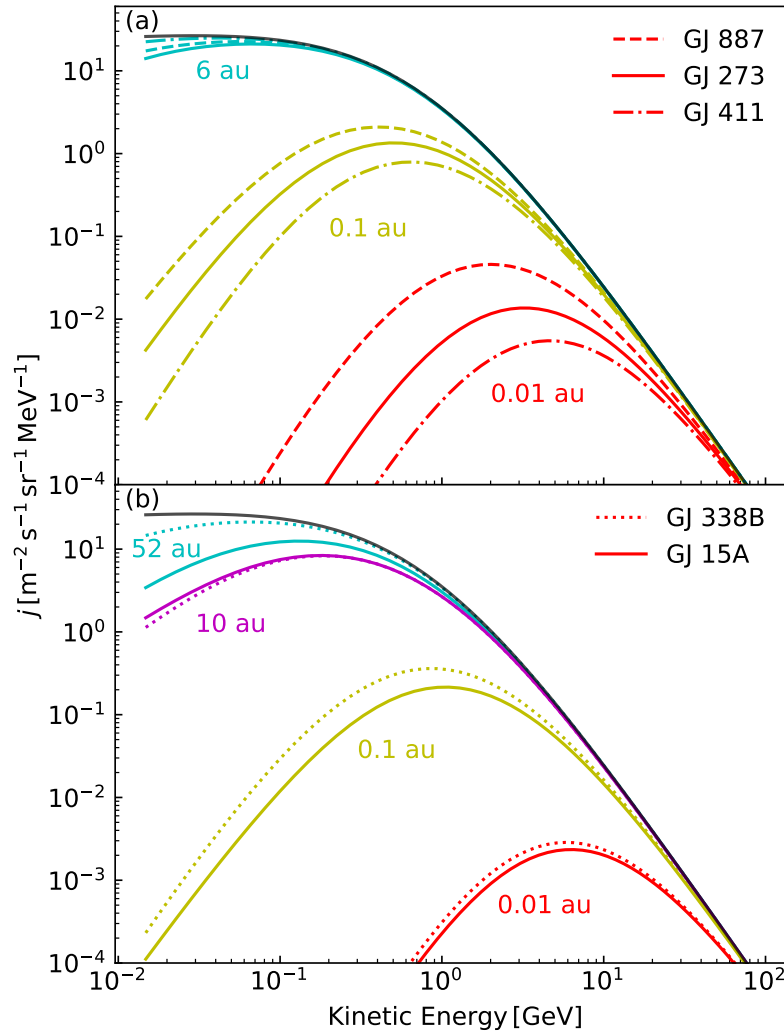


Figure 4.5: Differential intensity of Galactic cosmic rays as a function of kinetic energy. a) Group 1: solid lines GJ 273, dash-dotted GJ 411 and dashed GJ 887. b) Group 2: solid lines GJ 15A and dotted lines GJ 338B. The colours represent the same distances in each plot and the solid black line is the LIS.

The magnetic field and velocity properties of the stellar wind are important for the propagation of Galactic cosmic rays. In general, a stellar wind with a strong magnetic field can strongly suppress the flux of cosmic rays. This is because a strong magnetic

4.5 Galactic cosmic ray fluxes around M dwarfs

field results in a small diffusion coefficient which leads to the Galactic cosmic rays being strongly suppressed. To a lesser extent, a stellar wind with higher velocity is also efficient in suppressing the propagation of Galactic cosmic rays.

Fig. 4.5a shows that GJ 887 (dashed lines) has larger cosmic ray fluxes for the same distance in comparison to the other stars in group 1. This occurs because GJ 887 has the weakest magnetic field and, as a consequence, the cosmic rays are not suppressed significantly by its stellar wind. From group 1, GJ 273 (solid lines) has the strongest magnetic field, however, it modulates the Galactic cosmic rays less than GJ 411 (dash-dotted lines) with a smaller magnetic field. This is explained by the higher velocity wind of GJ 411, around 1.6 times higher than GJ 273. This behaviour, however, is not observed at all radii. At around 1 au for GJ 273 and GJ 411 the fluxes become comparable. The distance where it happens is due to a combination of magnetic field strength, the wind velocity and the size of the astrosphere.

In relation to group 2, GJ 15A (solid lines in Fig. 4.5b) is the one with the strongest radial magnetic field and the largest astrosphere. Naively, one might expect, since GJ 15A has a strong radial magnetic field, a stronger suppression of Galactic cosmic rays in comparison with all other stars for any given distance. However, when compared with GJ 338B (dotted lines), GJ 15A (solid lines) does not always modulate the cosmic rays more as can be observed in Fig. 4.5b at 10 au, for instance. The explanation for this behaviour lies in the total magnetic field profile of GJ 338B. Because GJ 338B rotates faster (compared with other stars in the sample), its azimuthal magnetic field profile (blue curve of Fig. 4.2 right panel) has a larger contribution than the radial magnetic field (green curve of Fig. 4.2 right panel) for distances greater than 2 au. As a consequence, the flux of cosmic rays becomes comparable for both stars at about 10 au (pink lines of Fig. 4.5b).

A way to understand the modulation of cosmic rays is by investigating the time-scales of the physical process involved in the cosmic ray propagation. The advective and diffusive time-scales are defined as:

$$\tau_{\text{adv}} = \frac{r}{u}, \quad \tau_{\text{dif}} = \frac{r^2}{\kappa(r, p)} \propto \frac{r^2}{p/B}. \quad (4.15)$$

Fig. 4.6 shows the ratio between the advective and diffusive time-scale as a function of the distance for group 1 (Fig. 4.6a) and group 2 (Fig. 4.6b) for different values of cosmic ray kinetic energy. The red shaded area is where advection dominates ($\tau_{\text{adv}}/\tau_{\text{dif}} < 1$) and the cosmic rays are strongly modulated by the stellar wind. The green shaded

area is where diffusion dominates ($\tau_{\text{adv}}/\tau_{\text{dif}} > 1$) and the cosmic rays experience little to no modulation.

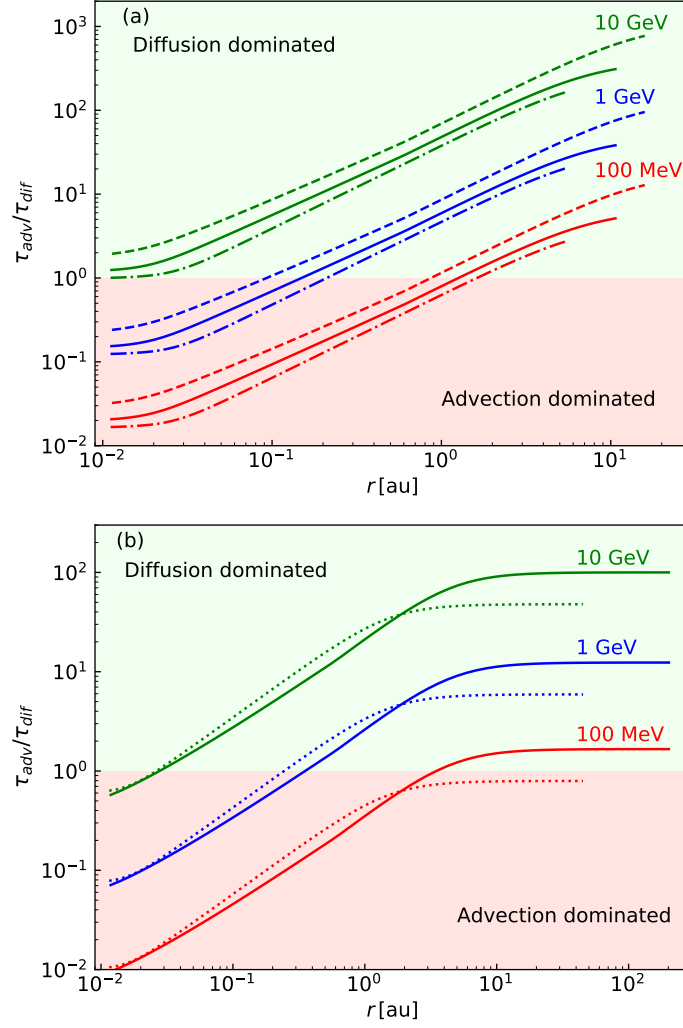


Figure 4.6: Ratio between advective and diffusive time-scale as a function of distance. The green shaded area is where diffusion dominates and the red shaded area is advection dominated. a) Group 1: solid lines GJ 273, dash-dotted GJ 411 and dashed GJ 887. b) Group 2: solid lines GJ 15A and dotted lines GJ 338B.

From group 1 (Fig. 4.6a), GJ 411 (dash-dotted lines) has the smallest time-scale ratio for all energies and distances and is followed by GJ 273 (solid lines) and GJ 887 (dashed lines). For this reason, GJ 411 modulates the cosmic rays more than the other two stars in group 1. From group 2 (Fig. 4.6b), GJ 15A (solid lines) has the smallest time-scale for $r < 2$ au, and as a consequence, it has lower cosmic ray fluxes. For $r > 2$ au, GJ 338B (dotted lines) has the smallest time-scale but at these distances, diffusion dominates and the cosmic rays suffer little (or no) modulation.

For 1 GeV energy cosmic rays (Fig. 4.6 blue curves), the region where the cosmic rays transition from the advection-dominated regime to the diffusive-dominated regime happens at $\lesssim 0.3$ au for all stars in our sample. This means that for $r \gtrsim 0.3$ au diffusion dominates and the cosmic rays are not strongly modulated. Rodgers-Lee et al. (2021b) proposed that if diffusion dominates at larger orbital distances varying the size of the astrosphere have almost no effect on the flux of Galactic cosmic rays. This implies that the Galactic cosmic ray spectrum for the stars in our sample should not be strongly affected by variations in astrosphere size as was observed for the case of GJ 338B and GJ 436 (Mesquita et al., 2021).

4.6 Discussion & Conclusions

In this paper, we investigated the differential intensity of Galactic cosmic rays within the astrospheres of M dwarfs. We focus on the habitable zones and at the planets orbit. We also investigate the wind properties of the M dwarfs in our sample. Our sample of stars were specially selected to include only M dwarfs with known planets and mass-loss rate measurements from Lyman- α observations. We selected five M dwarfs, namely: GJ 15A, GJ 273, GJ 338B, GJ 411 and GJ 887. These stars each have one or two known exoplanets and in total our sample contains 9 exoplanets including super-Earths and super-Neptunes.

In our simulations, the orbits of GJ 273 c and GJ 411 b lie within the Alfvén radius, in a sub-Alfvénic region. This configuration can potentially cause a star-planet interaction signature on the star as energy can be transported back to the star (Ip et al., 2004; Saur et al., 2013). Signatures of such interactions include anomalous CaII H&K emission (Shkolnik et al., 2008; Cauley et al., 2019) and planet-induced radio emission (Vedantham et al., 2020; Kavanagh et al., 2021).

The stellar wind velocity and magnetic field profiles play an important role in the propagation of Galactic cosmic rays. A stronger stellar magnetic field profile results in a lower flux of Galactic cosmic rays in the astrosphere when compared with a smaller magnetic field strength. To a lesser extend, a stronger stellar wind velocity also results in a lower Galactic cosmic ray fluxes in the astrosphere in comparison with a weak stellar wind velocity.

The mass-loss rate estimate from Lyman- α observations of the two binary systems in our sample is a combination of the two stars. When simulating the stellar wind we assume that the total mass-loss rate is the individual contribution of a single star in the binary system. This assumption may not be the best approach but how much it

would affect the results of the Galactic cosmic ray propagation? If for instance, the mass-loss rate is a contribution of 80% star A and 20% star B it probably means that the stellar properties of star A and B are different. If the magnetic field and the stellar wind velocity are different for star A and B it would probably cause an effect on the Galactic cosmic ray fluxes in each astrosphere.

Two stars in our sample have an Earth-like level of Galactic cosmic rays in their habitable zone, namely GJ 411 and GJ 887 (similar to what was found for GJ 436 by Mesquita et al., 2021). GJ 15A, GJ 273 and GJ 338B have lower Galactic cosmic rays fluxes in their habitable zone in comparison with Earth.

GJ 273 b is the only known exoplanet in the habitable zone in our sample. However, it receives a much lower Galactic cosmic ray flux than Earth, up to two orders of magnitude for 15 MeV energy cosmic rays. In addition, GJ 887 c lies close to the inner edge of the habitable zone, and its Galactic cosmic ray flux is around 10 times lower than Earth’s value at 15 MeV cosmic ray energies. The other planets in our sample, with the exception of GJ 15A c and GJ 411 c, show a higher suppression of Galactic cosmic rays when compared with Earth because they orbit much closer-in. Opposite to the other planets in our sample, GJ 15A c, has a larger semi-major axis and it receives slightly higher Galactic cosmic ray fluxes than Earth. GJ 411 c, which has also a larger semi-major axis, receives a much higher flux of cosmic rays (comparable with the LIS values) as it orbits close to the outer edge of GJ 411’s astrosphere. Interestingly, due to its close proximity to the astrosphere edge, GJ 411 c atmosphere could be affected by an enhancement of low energy cosmic rays in the LIS. Depending on the temperature of the planet, GJ 411 c may be a good candidate to study the impact of Galactic cosmic rays on atmospheric chemistry. Spectroscopic observations of molecular features from ions, such as H_3O^+ and NH_4^+ (Helling et al., 2016; Barth et al., 2021), with the James Webb Space Telescope (JWST, Gardner et al., 2006) and the Atmospheric Remote-sensing Infrared Exoplanet Large-survey (Ariel, Tinetti et al., 2021) could possibly constrain the incident cosmic ray spectrum and detect the existence of a possible excess of low-energy particles.

In our sample, the propagation of Galactic cosmic rays at large radii is dominated by diffusion, and according to Rodgers-Lee et al. (2021b) a change in the astrosphere size for this type of system does not strongly affects the spectrum of Galactic cosmic rays. This is what we observe for GJ 338B when we increased the astrosphere by 60%. For systems dominated by diffusion, thus, our lack of knowledge for the ISM properties does not strongly affect the Galactic cosmic ray propagation. To determine if the propagation of Galactic cosmic rays in a system is dominated by diffusion or advection

it is necessary to know the stellar wind velocity and magnetic field. However, it does not require knowledge of the ISM properties.

It is possible to quantify the impact of cosmic rays on life-forms by calculating the radiation dose a planet receives on its surface. Assuming GJ 273 b has an Earth-like atmosphere and no magnetic field we estimated that it receives an equivalent dose of 0.13 mSv/yr. This value is around 40% of the annual dose on Earth’s surface. Although GJ 273 b receives two orders of magnitude less 15 MeV energy cosmic rays than Earth, for high energy particles (\sim GeV) the difference in fluxes are much smaller (2.3 times less). That is the reason why the radiation dose on GJ 273 b’s surface is quite significant, because high-energy particles (\gtrsim 100 MeV) contribute most to the radiation dose at the planet’s surface.

What are the implications of a star having a similar Galactic cosmic ray flux as observed at Earth in their habitable zone? The level of Galactic cosmic rays Earth receives is not harmful for life as we know it. In comparison, the propagation of Galactic cosmic rays to Earth when life is thought to have started results in a significant reduction of Galactic cosmic rays in comparison with the present-day Earth values (Cohen et al., 2012; Rodgers-Lee et al., 2020). If life already exists on those planets it would not be negatively affected by the effects of Galactic cosmic rays. These assumptions also depend on whether the planet has an atmosphere and/or a magnetic field. If life still does not exist on those planets the Galactic cosmic ray fluxes may be important for the start of life (Rimmer et al., 2014; Airapetian et al., 2016).

The Parker Solar Probe will be able to measure the Galactic cosmic ray spectrum in the inner heliosphere (Marquardt & Heber, 2019), which will help to better characterise cosmic ray models for close-in exoplanets. A 2D (or 3D) cosmic ray transport model could be used in the future to more accurately model Galactic cosmic ray propagation, as is commonly used for the solar system (Potgieter et al., 2015a). However, given the lack of observational constraints for the type and level of turbulence in M dwarf winds 1D models seem well-motivated currently. The results found here can be further used to investigate the Galactic cosmic ray fluxes at the magnetospheres and atmospheres of the exoplanets in our sample.

Acknowledgements

This project has received funding from the European Research Council (ERC) under the European Union’s Horizon 2020 research and innovation programme (grant agreement No 817540, ASTROFLOW). The authors wish to acknowledge the SFI/HEA

Irish Centre for High-End Computing (ICHEC) for the provision of computational facilities and support. ALM and AAV acknowledge funding from the Provost's PhD Project award. DA acknowledges support from the New York University Abu Dhabi (NYUAD) Institute research grant G1502.

4.6 Discussion & Conclusions

The strong suppression of Galactic cosmic rays reaching AU Mic b, c and Prox Cen b

Amanda L. Mesquita, Donna Rodgers-Lee, Aline A. Vidotto, & Robert D. Kavanagh.
2022, MNRAS, 515, 1218–1227

Abstract

The propagation of Galactic cosmic rays is well understood in the context of the solar system but is poorly studied for M dwarf systems. Quantifying the flux of cosmic rays reaching exoplanets is important since cosmic rays are relevant in the context of life. Here, we calculate the Galactic cosmic ray fluxes in AU Mic and Prox Cen planetary systems. We propagate the Galactic cosmic rays using a 1D cosmic ray transport model. We find for Prox Cen b, AU Mic b and AU Mic c that the Galactic cosmic ray fluxes are strongly suppressed and are lower than the fluxes reaching Earth. We include in our models, for the first time for a star other than the Sun, the effect of radial particle drift due to gradients and curvatures in the stellar magnetic field. For Prox Cen we find that the inclusion of particle drift leads to less suppression of Galactic cosmic rays fluxes than when it is excluded from the model. In the case of AU Mic we explore two different wind environments, with a low and high stellar wind mass-loss rate. For AU Mic, the particle drift also leads to less suppression of the Galactic cosmic ray fluxes but it is only significant for the high mass-loss rate scenario. However, both wind scenarios for AU Mic suppress the Galactic cosmic rays strongly. Overall, careful modelling of stellar winds is needed to calculate the Galactic cosmic ray fluxes reaching exoplanets. The results found here can be used to interpret future exoplanet atmosphere observations and in atmospheric models.

5.1 Introduction

In a series of works, we have investigated the propagation of Galactic cosmic rays in M dwarfs (Mesquita et al., 2021, 2022a), with the aim to derive the flux of cosmic rays

that reach the habitable zone of these stars. We also calculated the radiation dose reaching an exoplanet surface (Mesquita et al., 2022a). Here, we continue this series of works, focusing on two nearby M dwarfs whose orbiting planets are amenable to atmospheric characterisation: AU Mic and Prox Cen. M dwarfs have habitable zones that are close-in due to their low luminosity. Because of our current observational biases towards finding close-in planets, this means that it is easiest to observe planets orbiting in the habitable zone of M dwarfs. However, being in the habitable zone (i.e. where surface liquid water can exist, Kasting et al., 1993; Selsis et al., 2007) is not thought to be the only element necessary for a planet to sustain life. Many factors can influence exoplanet habitability (see e.g. Meadows & Barnes, 2018). One important factor for habitability is cosmic rays.

Cosmic rays are a source of ionisation that can drive the production of prebiotic molecules in Earth-like (Airapetian et al., 2016) and Jupiter-like atmospheres (Barth et al., 2021). Hence, cosmic rays may have been important for the beginning of life on Earth and other planets. Fingerprint ions, such as H_3O^+ , H_3^+ and NH_4^+ (Helling & Rimmer, 2019; Barth et al., 2021), have been identified as a good indication of ionisation in hot gas giant atmospheres due to both Galactic and stellar cosmic rays (also known as stellar energetic particles). Spectroscopic observations with the James Webb Space Telescope (JWST, Gardner et al., 2006) and the Atmospheric Remote-sensing Infrared Exoplanet Large-survey (ARIEL, Tinetti et al., 2021) of absorption features due to these fingerprint ions may be able to constrain the cosmic ray fluxes in exoplanet atmospheres in the future. In order to interpret future exoplanet atmosphere observations and also to provide input for atmospheric chemistry models, it is necessary to know the flux of Galactic cosmic rays reaching exoplanets.

As Galactic cosmic rays propagate through stellar systems they are suppressed, in a energy-dependent way, by the existence of a magnetised stellar wind (e.g. Gri  meier et al., 2005; Sadovskii et al., 2018; Herbst et al., 2020; Mesquita et al., 2021; Rodgers-Lee et al., 2021b; Mesquita et al., 2022a). This is analogous to what occurs in the solar system, known as the modulation of Galactic cosmic rays (e.g. Potgieter, 2013). The Galactic cosmic ray fluxes reaching an exoplanet are affected by diffusion, advection, adiabatic losses and particle drift processes that depend on the stellar wind properties (the magnetic field and velocity). They are also affected by the Galactic cosmic ray spectrum in the interstellar medium (ISM) and the ISM properties (velocity and density).

Particle drifts, caused by gradients and curvatures of the heliospheric magnetic field, have been pointed out as an important ingredient in the description of cosmic

ray transport inside the heliosphere (Jokipii et al., 1977). Many works have included the effect of particle drifts to describe the transport of cosmic rays in the heliosphere (Strauss et al., 2012; Strauss & Potgieter, 2014; Potgieter, 2013; Vos & Potgieter, 2015; Potgieter & Vos, 2017; Kopp et al., 2021), in good agreement with observations at Earth. Particle drifts were also included to study the young Sun system (Cohen et al., 2012). However, for other stars the effect of particle drift are usually neglected (Gri  meier et al., 2005; Herbst et al., 2020; Mesquita et al., 2021; Rodgers-Lee et al., 2021b; Mesquita et al., 2022a). One reason for this is that to implement particle drift it is necessary to know the 3D large-scale stellar magnetic field geometry. At this point, the 3D large scale stellar magnetic field geometry is known for more than a hundred stars (e.g. Vidotto et al., 2014a; See et al., 2015; Klein et al., 2021a,b), albeit the stellar wind mass-loss rates have been determined for a smaller number of stars (e.g. Wood, 2004; Wood et al., 2021). Since different stars have different winds due to their different (and some times extreme) magnetic fields and high rotation rates, 3D models of the stellar wind are an important tool to study the propagation of cosmic rays and the effects of particle drift in stellar systems.

In this work, we investigate the well-studied M dwarfs AU Mic and Prox Cen as they both host detected exoplanets (Anglada-Escud   et al., 2016; Plavchan et al., 2020; Martioli et al., 2021). Prox Cen b is an Earth-size planet orbiting at 0.048 au (Anglada-Escud   et al., 2016). AU Mic b and AU Mic c are both Neptune-size planets at 0.064 au and 0.11 au, respectively (Plavchan et al., 2020; Martioli et al., 2021). In particular, Prox Cen b orbits in the habitable zone and AU Mic is a JWST target which will be observed soon using the Near InfraRed Camera (NIRCam) to search for undetected close-in planets. In addition, the large scale magnetic field geometry has been reconstructed with Zeeman-Doppler Imaging (ZDI) for both Prox Cen and AU Mic (Klein et al., 2021a,b). In terms of their stellar wind properties, Prox Cen has a mass-loss rate constrained by Lyman-   observations to be $< 4 \times 10^{-15} M_{\odot} \text{ yr}^{-1}$ (Wood et al., 2001). While mass-loss rate constraints for AU Mic are less stringent, models predict that it ranges from 10 to 1000 times the solar wind mass-loss rate (Plavchan et al., 2020; Chiang & Fung, 2017). Kavanagh et al. (2021) modelled the winds of the Prox Cen and AU Mic planetary systems using these observational constraints for the stellar magnetic fields and mass-loss rates.

In this paper, we use the 3D stellar wind model results from Kavanagh et al. (2021) to compute the propagation of Galactic cosmic rays through the AU Mic and Prox Cen astrospheres (analogous to the heliosphere). We use our 1D model of cosmic ray transport (Rodgers-Lee et al., 2020; Mesquita et al., 2021; Rodgers-Lee et al.,

2021b; Mesquita et al., 2022a) to calculate the spectrum of Galactic cosmic rays within the astrospheres. Here we implement in this model the effect of particle drift for the first time in an M dwarf system. This paper is structured as follows: our modelling framework is explained in Section 5.2. We then apply our model to Prox Cen (Section 5.3) and AU Mic (Section 5.4), where we compute the cosmic ray fluxes that reach the known planets of these systems, as well as in their habitable zones. In the case of AU Mic, we also explore different assumptions for the stellar wind properties, in order to investigate how a poorly constrained mass-loss rate affects our results. Section 5.5 presents a discussion of our results and conclusions.

5.2 Modelling Framework

Our modelling framework consists of the following ingredients. First, we adopt a stellar wind model to derive the stellar wind properties (described in Section 5.2.1). Second, using the stellar wind properties, we model the cosmic ray transport as a diffusive-advective process as they propagate through the stellar wind (see Section 5.2.3). The Galactic cosmic rays are injected at the boundary between the stellar wind and the ISM. We determine this outer boundary by calculating the size of the astrosphere (see Section 5.2.2).

5.2.1 Stellar wind properties

In order to study the propagation of Galactic cosmic rays through an astrosphere it is essential to know the stellar wind velocity and magnetic field strength. For AU Mic and Prox Cen, we use the 3D magnetohydrodynamic (MHD) wind simulations from Kavanagh et al. (2021). These simulations are conducted using the AWSoM model (van Holst et al., 2014; Jin et al., 2017), which was originally derived for the study of the solar wind. Additionally, to benchmark our cosmic ray transport code with observations of cosmic rays at the Earth, we also use a model of the solar wind, which is shown in Section 5.A.

In their study, Kavanagh et al. (2021) used reconstructed surface magnetic field maps for Prox Cen and AU Mic that were obtained using the ZDI method (Klein et al., 2021a,b). In the AWSoM model, the stellar wind is heated and dissipated by Alfvén waves injected at the base of the chromosphere. To account for the range of mass-loss rates expected for AU Mic, Kavanagh et al. (2021) computed two different stellar wind models: one with $\dot{M} = 5.5 \times 10^{-13} M_{\odot} \text{ yr}^{-1}$ and the other with $\dot{M} = 1.2 \times 10^{-11} M_{\odot} \text{ yr}^{-1}$. We refer to these models as ‘AU Mic low’ and ‘AU Mic high’, respectively. Although

these two stellar wind models have the same stellar wind magnetic field map, they have different Alfvén wave fluxes, giving rise to different stellar wind mass-loss rates and terminal velocities.

Table 5.1 summarises some of the properties for the stars studied here, including their adopted stellar wind properties. Fig. 5.1 shows the equatorial plane cut of the stellar wind velocity (top row) and magnetic field intensity (bottom row) for Prox Cen, ‘AU Mic low’ and ‘AU Mic high’. The values shown for small orbital distances ($r < 100 R_\star$) are from the 3D stellar wind model of Kavanagh et al. (2021). Beyond that, the values shown are extrapolated values (see Section 5.B for details). The stellar magnetic field geometry shapes the stellar wind velocity distribution, i.e., a smoother magnetic field geometry results in a smoother velocity. For instance, Prox Cen shows a complex magnetic field geometry (more than simply a dipole component) and streams with very different speeds. AU Mic instead shows a less complex magnetic field geometry (relatively close to a dipole) and consequently less streams with different speeds. Compared to our model for the Sun, with $u_\infty = 540 \text{ km s}^{-1}$, (see Section 5.A), Prox Cen (810 km s^{-1}) and ‘AU Mic low’ (650 km s^{-1}) have comparable terminal wind velocities while ‘AU Mic high’ has a much faster terminal velocity of 2460 km s^{-1} . In relation to the stellar surface magnetic field, both Prox Cen and AU Mic have a much higher magnetic field intensity in comparison to our model for the Sun, $B \sim 2 \text{ G}$ (see Section 5.A).

Table 5.1: Properties of the Prox Cen and AU Mic stellar systems. The quantities without reference are calculated in this work.

Physical parameter	Prox Cen	AU Mic		Unit
		‘AU Mic low’	‘AU Mic high’	
Stellar mass (M_\star)	0.12^a	0.50^b		M_\odot
Stellar radius (R_\star)	0.14^a	0.75^b		R_\odot
Distance (d)	1.30^a	9.79^b		pc
Habitable zone	$0.03 - 0.09^c$	$0.26 - 0.66^c$		au
Average stellar surface magnetic field (B_\star)	200^d	475^e		G
ISM/star relative velocity (v_{ISM})	25^f	19		km s^{-1}
ISM ram pressure (P_{ISM})	2.5×10^{-12}	1.5×10^{-12}		dyn cm^{-2}
Stellar wind mass-loss rate ^g (\dot{M})	5.0×10^{-15}	5.5×10^{-13}	1.2×10^{-11}	$M_\odot \text{ yr}^{-1}$
Stellar wind ram pressure (P_{ram})	3.3×10^{-6}	1.2×10^{-5}	4.6×10^{-4}	dyn cm^{-2}
Terminal velocity ^g (u_∞)	810	650	2460	km s^{-1}
Astrospheric size (R_{ast})	75	980	6140	au

^aAnglada-Escudé et al. (2016); ^bPlavchan et al. (2020); ^ccalculated using the prescription of Kopparapu et al. (2014); ^dKlein et al. (2021a); ^eKlein et al. (2021b);

^fWood et al. (2001); ^gKavanagh et al. (2021).

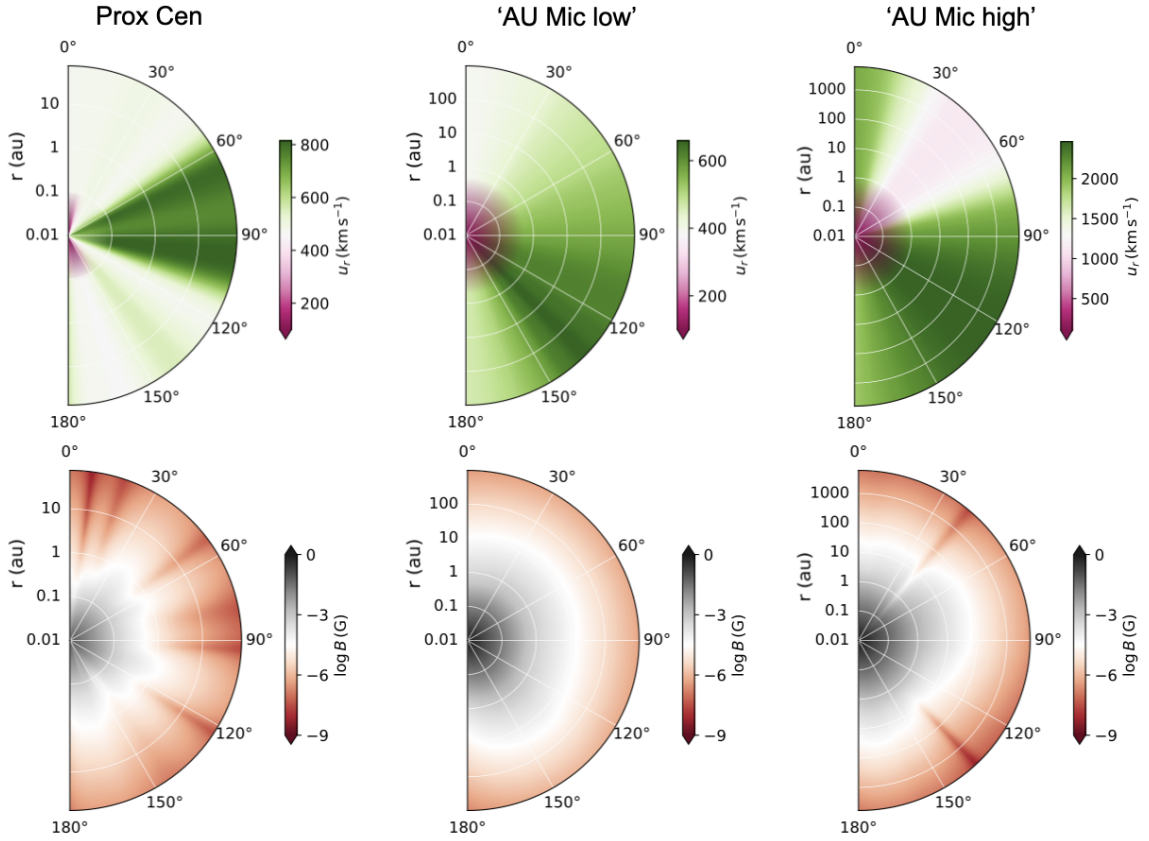


Figure 5.1: Equatorial plane cut of the stellar wind properties, from left to right, for Prox Cen, ‘AU Mic low’ and ‘AU Mic high’. The top row shows the stellar wind velocity and the bottom row shows the magnitude of the total magnetic field for the full radial extent of each star’s astrosphere. The values shown for small orbital distances are from 3D stellar wind models (Kavanagh et al., 2021) and the values shown at large distances are an extrapolation (see Section 5.B for details).

5.2.2 The astrosphere size

The astrosphere is the ‘bubble’ region around a star dominated by its stellar wind. The astrosphere size can be very important for the propagation of Galactic cosmic rays because outside this region cosmic rays are not suppressed. The size of the astrosphere can be calculated as

$$R_{\text{ast}} = \sqrt{\frac{P_{\text{ram}}(R)}{P_{\text{ISM}}}} R, \quad (5.1)$$

where P_{ram} is the ram pressure of the stellar wind expressed as

$$P_{\text{ram}} = \rho u^2 = \frac{\dot{M}u}{4\pi R^2}, \quad (5.2)$$

where u is the wind velocity, R is a given reference distance beyond which the wind has reached its terminal velocity. The ISM ram pressure, P_{ISM} , can be expressed as

$$P_{\text{ISM}} = m_p n_{\text{ISM}} \nu_{\text{ISM}}^2, \quad (5.3)$$

where m_p is the proton mass, n_{ISM} is the total ISM number density of hydrogen and ν_{ISM} is the ISM velocity as observed by the star.

To derive the total ISM number density of hydrogen (n_{ISM}), we use the same ISM neutral hydrogen density ($n_{\text{n}} = 0.14 \text{ cm}^{-3}$) and ionised hydrogen density ($n_{\text{i}} = 0.1 \text{ cm}^{-3}$) as given by Model 10 of Wood et al. (2000) which is a good fit for nearby systems in the local ISM. Assuming that the ISM cloud along the line of sight towards AU Mic is most consistent with the Mic cloud, we derive the heliocentric flow vector in the direction of AU Mic and the radial velocity of the Mic cloud using the ISM Kinematic Calculator (Redfield & Linsky, 2008). The heliocentric velocity of AU Mic is calculated using its proper motion (Gaia Collaboration, 2020) and its radial velocity (Fouqué et al., 2018). From these assumptions, we calculate the ISM velocity and pressure as seen by AU Mic to be $v_{\text{ISM}} = 19 \text{ km s}^{-1}$ and $P_{\text{ISM}} = 1.5 \times 10^{-12} \text{ dyn cm}^{-2}$. If instead we assume that the ISM cloud along the line of sight towards AU Mic is consistent with the Local Interstellar Cloud (LIC), the ISM velocity does not vary significantly ($v_{\text{ISM}} = 19.4 \text{ km s}^{-1}$). For Prox Cen, we use the ISM velocity as given by Wood et al. (2001) and shown in Table 5.1. The astrospheric size of Prox Cen and AU Mic (for the two stellar wind scenarios) are given in Table 5.1. The astrospheric size is proportional to the stellar wind mass-loss rate. Compared with the heliosphere, where $R_{\text{ast}} = 122 \text{ au}$ (as observed by *Voyager 1*, Stone et al., 2013, 2019), Prox Cen’s

astrosphere is 40% smaller while R_{ast} for ‘AU Mic low’ is 8 times larger and for ‘AU Mic high’ it is 50 times larger.

5.2.3 Cosmic ray transport equation

When interacting with magnetised stellar winds, Galactic cosmic rays can experience global changes in their intensity and energy, referred to as modulation. The cosmic ray propagation through a magnetised stellar wind can be described by the transport equation of Parker (1965). We use a 1D cosmic ray transport model to calculate the cosmic rays fluxes within the M dwarf systems. The model used here is based on the model described in Rodgers-Lee et al. (2020) and was already used for M dwarfs (Mesquita et al., 2021, 2022a). Here, we add for the first time, for a star other than the Sun, the effect of particle drift.

We numerically solve the time-dependent, spherically symmetric transport equation for cosmic rays, as given by

$$\frac{\partial f}{\partial t} = \nabla \cdot (\kappa \nabla f) - (\mathbf{u} + \langle \mathbf{v}_d \rangle) \cdot \nabla f + \frac{1}{3} (\nabla \cdot \mathbf{u}) \frac{\partial f}{\partial \ln p}, \quad (5.4)$$

where f and p are the cosmic ray phase space density and momentum, respectively. The diffusion of cosmic rays is represented by the first term on the right-hand side of Equation (5.4) and depends on the diffusion coefficient, κ . The stellar wind velocity, \mathbf{u} , and the particle drift velocity, $\langle \mathbf{v}_d \rangle$, appear in the second term and represent advection of the cosmic rays. The last term represents momentum advection, also known as adiabatic losses, which moves the cosmic rays to lower energies. More details of the model can be found in Rodgers-Lee et al. (2020). Our results in Sections 5.3 and 5.4 present the differential intensity of cosmic rays, j , rather than the phase space density, f , where $j(T) = p^2 f(p)$. T is the cosmic ray kinetic energy.

We use logarithmically spaced spatial and momentum grids. The inner spatial boundary is set as 0.01 au and the outer boundary is set as the astrosphere size, R_{ast} , for each star (see Table 5.1). The spatial grid includes the orbits of the known exoplanets and the habitable zones. The spatial grid has 80 grid zones for Prox Cen, 100 grid zones for the Sun and ‘AU Mic low’ and 120 grid zones for ‘AU Mic high’. The spatial resolution varies for each system because they have different astrosphere sizes. The inner spatial boundary condition is reflective and the outer spatial boundary condition is fixed as the Local Interstellar Spectrum (LIS) for Galactic cosmic rays. The LIS that we adopt is given by the model fit to the *Voyager 1* observations using Eq. (1) of

Vos & Potgieter (2015)¹. The LIS is considered to be constant as a function of time in our simulations. The momentum grid ranges from $p_{\min} = 0.15 \text{ GeV}/c$ to $p_{\max} = 100 \text{ GeV}/c$ with 60 momentum bins. The limits of the momentum grid are chosen due to the fact that cosmic rays with higher energies than the upper limit are quite uncommon and not important for planetary atmosphere chemistry (Rimmer & Helling, 2013), while cosmic rays with lower energy than the lower limit are not expected to reach the planetary surface (Atri, 2017). Low-energy particles, however, can deposit energy in the planetary atmosphere (Rodgers-Lee et al., 2020) and may be relevant for chemical models (e.g. Griebmeier et al., 2015; Barth et al., 2021). Both, inner and outer, momentum boundary conditions are outflow boundary conditions.

5.2.3.1 The diffusion coefficient

The diffusion coefficient, κ , in Equation (5.4), depends on the level of turbulence in the stellar magnetic field and the cosmic ray momentum. From quasi-linear theory (Jokipii, 1966; Schlickeiser, 1989), the diffusion coefficient can be denoted as

$$\frac{\kappa(r, p)}{\beta c} = \eta_0 \left(\frac{p}{p_0} \right)^{1-\gamma} r_L, \quad (5.5)$$

where r_L is the cosmic ray Larmor radius, $p_0 = 3 \text{ GeV}/c$ and $\beta = v/c$ is the ratio between the cosmic ray's velocity and the speed of light. η_0 represents the level of turbulence present in the system. In our simulations we set $\eta_0 = 1$ to be consistent with other works (Rodgers-Lee et al., 2020; Mesquita et al., 2021, 2022a). γ determines the power-law dependency with momentum. The type of turbulence can be described by different prescriptions, such as, Bohm-type ($\gamma = 1$), Kolmogorov-type ($\gamma = 5/3$) and MHD-driven ($\gamma = 3/2$) turbulence. We note that the Galactic cosmic ray spectrum calculated at any given distance is affected by the type of turbulence adopted. The type of turbulence present in M dwarf systems is still unknown and here we simply adopt $\gamma = 1$, i.e. Bohm-type turbulence. This has been used frequently in many works (Svensmark, 2006; Cohen et al., 2012; Rodgers-Lee et al., 2020; Mesquita et al., 2021; Rodgers-Lee et al., 2021b; Mesquita et al., 2022a) and fits the present-day observations at Earth quite well (Rodgers-Lee et al., 2020).

The magnetic field and velocity are important wind properties in the context of Galactic cosmic ray propagation. For instance, the stronger the magnetic field, the

¹As discussed in Mesquita et al. (2021, 2022a), this is a good assumption since according to γ -ray observations the inferred cosmic ray spectrum within a region of 1 kpc in the local Galaxy is consistent with *Voyager* measurements in the local ISM (Neronov et al., 2017).

more the Galactic cosmic ray spectrum is suppressed (for fixed values of γ and η_0). This is because a strong magnetic field implies smaller diffusion coefficients. This means that generally advective processes become more important, resulting in more modulation of cosmic rays. The same is valid for the wind velocity, however to a lesser extent (Mesquita et al., 2022a), i.e. a stronger stellar wind velocity results in more advection which suppresses the cosmic ray fluxes. The stellar wind density does not attenuate the cosmic rays, as the density is very low. However, it influences the size of the astrosphere (see Equation (5.1)). In cases where advection is the dominant physical process, the size of the astrosphere can affect the Galactic cosmic ray fluxes (Rodgers-Lee et al., 2021b).

5.2.3.2 The particle drift

The averaged particle drift velocity, $\langle \mathbf{v}_d \rangle$, is caused by gradients and curvatures in the stellar magnetic field. The drift velocity can be expressed as a function of the magnetic field as (Jokipii et al., 1993)

$$\langle \mathbf{v}_d \rangle = \frac{p\beta c^2}{3e} \nabla \times \frac{\mathbf{B}}{B^2}, \quad (5.6)$$

where B is the stellar wind magnetic field. The drift velocity also depends on the cosmic ray momentum p and velocity v (through β).

In our 1D propagation model, we only include the radial component of the drift velocity, which can be expressed in spherical coordinates as

$$\langle \mathbf{v}_d \rangle = \frac{p\beta c^2}{3e} \frac{1}{r \sin \theta} \left(\underbrace{\frac{\partial}{\partial \theta} \left(\sin \theta \frac{B_\phi}{B^2} \right)}_{\text{i}} - \underbrace{\frac{\partial}{\partial \phi} \left(\frac{B_\theta}{B^2} \right)}_{\text{ii}} \right) \mathbf{e}_r, \quad (5.7)$$

where θ is the polar angle ($\theta = 90^\circ$ at the equator) and ϕ is the azimuthal angle.

Fig. 5.2 shows the absolute value of the drift velocity components that we calculate for Prox Cen for cosmic rays with $p = 1 \text{ GeV}/c$. The left panel shows term i of Equation (5.7) as a function of radial distance and polar angle, θ , for the value of ϕ where the stellar wind velocity have its strongest intensity ($\phi = 97^\circ$). The right panel shows term ii of Equation (5.7) as a function of radial distance and the azimuthal angle, ϕ , for the equatorial plane ($\theta = 90^\circ$). The dotted areas represent regions with negative velocities. The momentum dependency of the drift velocity is a multiplicative factor, i.e., the drift velocity is 100 times higher for $100 \text{ GeV}/c$ momentum cosmic rays than for $1 \text{ GeV}/c$ cosmic rays. Both terms of the drift are spatially non-linear and vary as a

function of r , θ and ϕ significantly, as shown in Fig. 5.2. In the left panel of Fig. 5.2 we did not include $\theta = 0^\circ$ because $1/\sin \theta$ in Equation (5.7) implies that the drift value becomes infinite at this point. In our simulations we only include the drift velocity as a function of r and p for a single value of θ and ϕ where i and ii are combined. We will discuss the effect of the 2D/3D spatial variation of the drift velocity in Section 5.5.

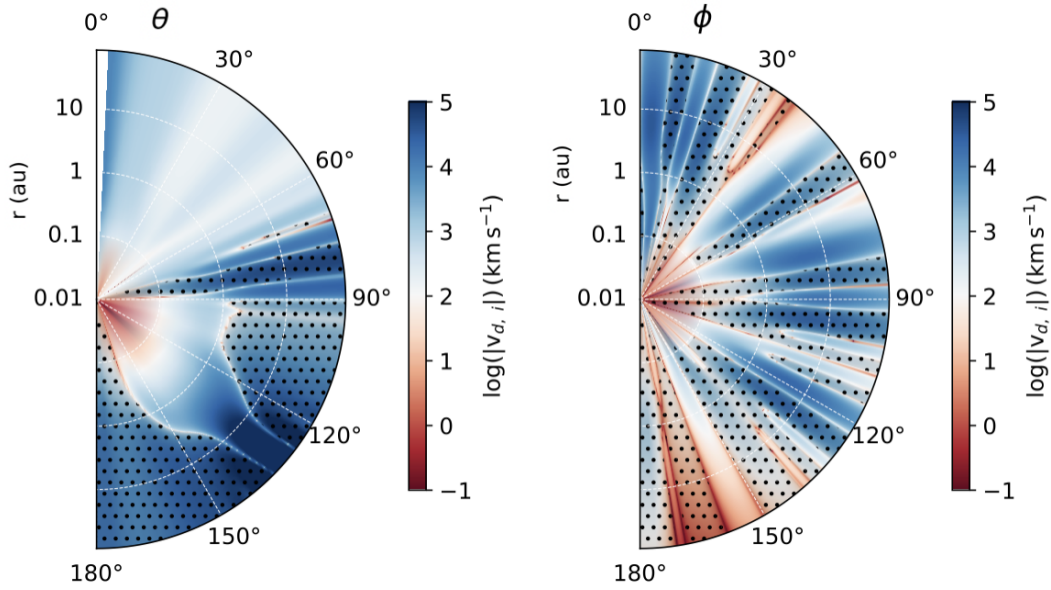


Figure 5.2: Components of the radial drift velocity for Prox Cen for cosmic rays with 1 GeV/c momentum. *Left:* term i of Equation (5.7) as a function of r and θ for ϕ direction where the stellar wind is fastest (see Fig. 5.1 top row). *Right:* term ii of Equation (5.7) as a function of r and ϕ for the equatorial plane. In both plots the dotted regions represent regions with negative velocities.

The effects of $\langle \mathbf{v}_d \rangle$ have been neglected in past studies of M dwarf systems. However, if $\langle \mathbf{v}_d \rangle$ is larger or comparable to the stellar wind velocity, u , it can affect the modulation of cosmic rays. The particle drift acts as an additional advective term. Hence, when the particle drift velocity is positive, i.e. radially outward pointing, then the Galactic cosmic ray fluxes are reduced. We will discuss this in more detail in Sections 5.3 and 5.4.

5.3 Prox Cen: the Galactic cosmic ray fluxes including particle drift effects

Prox Cen is the closest star to the solar system and has a terrestrial planet in its habitable zone. Here, we investigate the propagation of Galactic cosmic rays within its

5.3 Prox Cen: the Galactic cosmic ray fluxes including particle drift effects

astrosphere. Since we use a 1D cosmic ray transport model, we select particular cuts of the 3D wind simulations to calculate the drift velocity at any given orbital distance. We investigate the Galactic cosmic ray fluxes at the equatorial plane ($\theta = 90^\circ$) because this allows us to investigate the effect of Galactic cosmic rays at the planet's equatorial orbit. Since the stellar wind velocity also varies with ϕ , we further fix the value of $\phi = 97^\circ$ for Prox Cen. We note that at the chosen θ and ϕ the stellar wind has already reached its terminal velocity within the 3D stellar wind simulation domain.

Fig. 5.3 shows the intensity of cosmic rays as a function of kinetic energy for Prox Cen when particle drift is considered (dashed lines) and when it is neglected (solid lines) at different distances. The shaded areas represent the Galactic cosmic ray flux in the habitable zone when particle drift is considered (dark salmon) and when it is neglected (light salmon). The black line is the LIS. When particle drift is included, Prox Cen shows a considerably higher flux of cosmic rays for particles with kinetic energy below 1 GeV. At the orbit of Prox Cen b, the intensity of 0.1 GeV energy cosmic rays is 7 times higher when drift is considered (dashed violet line) in comparison with results when drift is neglected (solid violet line). A similar trend is observed at 1 au (green lines) and in the habitable zone (shaded areas).

The effects we see with the inclusion of particle drifts can be understood by comparing the drift velocity with the stellar wind velocity. Fig. 5.4 shows the stellar wind velocity and the drift velocity profiles (for $\theta = 90^\circ$, $\phi = 97^\circ$) for Prox Cen. The green triangles are $|\langle \mathbf{v}_d \rangle|$ for cosmic rays with $p = 1$ GeV/c, while the blue triangles are for $p = 0.15$ GeV/c. The stellar wind velocity is lower than $|\langle \mathbf{v}_d \rangle|$ for $r > 0.3$ au (green triangles) and, as a consequence, the drift velocity affects the modulation of cosmic rays. The Galactic cosmic ray flux within the Prox Cen system is higher when particle drifts are included because the drift velocity is large and negative in value (open triangles in Fig. 5.4). If, on the other hand, the drift velocity were positive, the cosmic ray flux would be reduced.

Our results likely depend on the direction we choose to study (θ and ϕ values). In the case of Prox Cen for instance, it is possible that for azimuthal angles where the wind velocity is lower the particle drift may play an even more important role in modulating the cosmic rays. In Fig. 5.2 we can see that each term of the drift velocity varies significantly with θ and ϕ . A 2D or 3D cosmic ray simulation would be necessary to investigate the cosmic ray propagation in other directions.

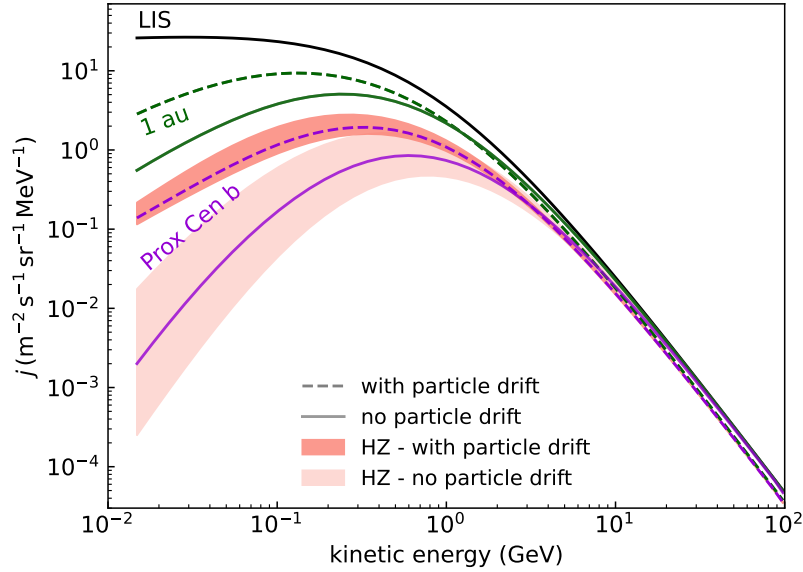


Figure 5.3: Differential intensity of Galactic cosmic rays as a function of cosmic ray kinetic energy for Prox Cen. The solid lines represent the Galactic cosmic ray flux without considering the particle drift and the dashed lines when the drift is considered. The black solid line is the LIS. The green lines are the Galactic cosmic ray flux at 1 au and the violet lines are the Galactic cosmic ray flux at Prox Cen b. The shaded areas are the Galactic cosmic ray flux in the habitable zone, both accounting for (dark salmon) and neglecting (light salmon) particle drift. In the case of Prox Cen, the inclusion of particle drift leads to Galactic cosmic ray fluxes that are an order of magnitude higher for cosmic ray energies $\lesssim 0.1$ GeV.

5.4 AU Mic: the effect of an unconstrained mass-loss rate on Galactic cosmic ray fluxes

AU Mic is a young M dwarf stellar system that hosts two Neptune-size exoplanets. Both exoplanets have close-in orbits and are not within the habitable zone. As discussed in Section 5.2.1, we investigate Galactic cosmic ray propagation for the two stellar wind scenarios explored by Kavanagh et al. (2021). Although their magnetic field profiles are similar, the mass-loss rate and terminal velocity of ‘AU Mic high’ are, respectively, 21 and 4 times larger than the values for ‘AU Mic low’. Because of their different wind properties, the calculated sizes of the astrosphere differ for these two wind models. Similar to Prox Cen, we investigate the flux of Galactic cosmic rays for AU Mic in the equatorial plane and we set $\phi = 133^\circ$ for ‘AU Mic low’ and $\phi = 126^\circ$ for ‘AU Mic high’.

Fig. 5.5 shows the cosmic ray fluxes as a function of kinetic energy for the two wind scenarios of AU Mic. Here, in this figure, we only show the results of our calculations that consider particle drift. The orange shaded areas represent the cosmic ray fluxes

5.4 AU Mic: the effect of an unconstrained mass-loss rate on Galactic cosmic ray fluxes

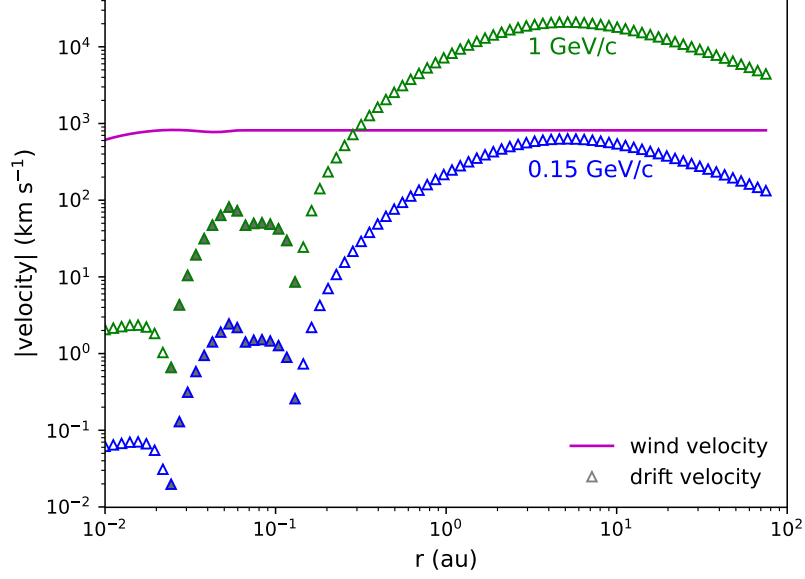


Figure 5.4: Stellar wind and radial drift velocity as a function of distance for Prox Cen at $\theta = 90^\circ$, $\phi = 97^\circ$. The magenta line is the stellar wind velocity from Kavanagh et al. (2021). The green and blue triangles are the absolute value of the radial drift velocity for cosmic rays with 1 GeV/c and 0.15 GeV/c momentum, respectively. Open triangles represent negative values and filled triangles represent positive values. Cosmic rays with higher momenta will have larger drift velocity values and vice-versa.

in the habitable zone, where the dark orange is for ‘AU Mic low’ and the light orange for ‘AU Mic high’. Blue, purple and salmon lines are the cosmic ray fluxes at 1 au, AU Mic b and AU Mic c. In general, the Galactic cosmic ray fluxes for ‘AU Mic high’ are much reduced in comparison to ‘AU Mic low’ (see for instance blue lines in Fig. 5.5). The difference is particularly sharp for cosmic rays with energy lower than 1 GeV. Within each wind prescription, the intensity of cosmic rays at AU Mic b and AU Mic c is similar since the planets have close orbits.

In the case of AU Mic, the unconstrained mass-loss rate of the stellar wind and the different terminal velocities from each model strongly affect the Galactic cosmic ray intensities within the system as shown in Fig. 5.5. This is opposite to what was derived for GJ 436 by Mesquita et al. (2021), in which the wind properties did not strongly affect the cosmic ray fluxes. The reason for this, is that AU Mic is dominated by advective processes (with or without the inclusion of particle drift), while GJ 436 is dominated by diffusive processes. When advection dominates it results in a stronger suppression of cosmic rays, while when diffusion dominates it results in little (or no) modulation. The diffusive/advective processes are correlated with the stellar wind velocity and magnetic field (see Section 5.2.3.1 and the diffusive/advective time-scales

in Section 3.2 of Mesquita et al. 2021). In addition, when advection dominates the size of the astrosphere can affect the suppression of cosmic rays (Rodgers-Lee et al., 2021b).

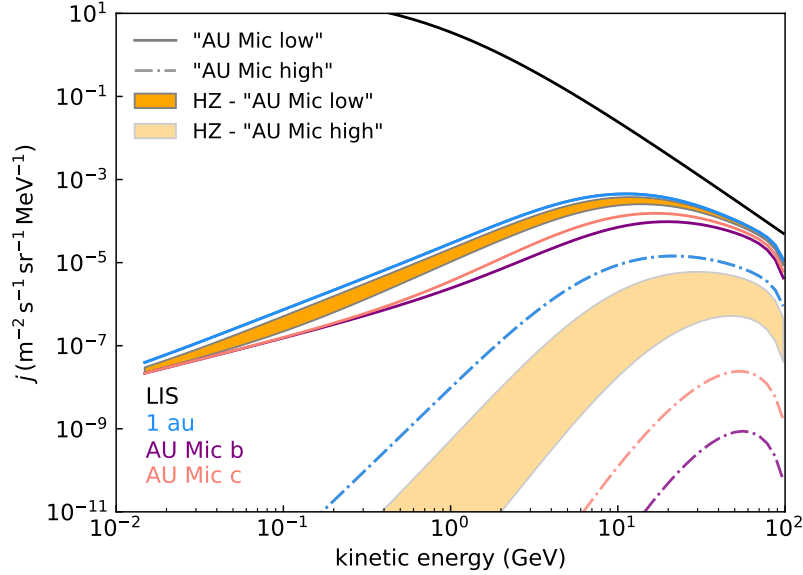


Figure 5.5: Differential intensity of Galactic cosmic rays as a function of cosmic ray kinetic energy for ‘AU Mic low’ (solid lines) and ‘AU Mic high’ (dash dotted lines). Blue, purple and salmon lines are the differential intensity of cosmic rays at 1 au, AU Mic b and AU Mic c, respectively. The orange shaded areas represent the fluxes in the habitable zone, where the dark orange is for ‘AU Mic low’ and the light orange for ‘AU Mic high’. The stellar wind properties for the ‘AU Mic high’ case are more efficient at suppressing the Galactic cosmic ray fluxes.

In the case of ‘AU Mic low’, the drift velocity profile for cosmic rays with 1 GeV/c momentum is negative but almost negligible when compared with the stellar wind velocity profile and, as a consequence, the cosmic ray fluxes are not influenced by the inclusion of drift. For ‘AU Mic high’, the drift velocity for cosmic rays with 1 GeV/c momentum is negligible ($\lesssim 30 \text{ km s}^{-1}$) for $r < 1 \text{ au}$. For $1 \text{ au} < r < 10 \text{ au}$, it is positive and relatively slow, while for $r > 10 \text{ au}$ $|\langle v_d \rangle|$ is negative and fast (but slower than the drift velocity intensities observed for Prox Cen). Thus, the Galactic cosmic ray intensities are slightly affected by the inclusion of particle drift for close-in distances ($r < 1 \text{ au}$). For large distances ($r > 1 \text{ au}$) neglecting the drift can underestimate the cosmic ray fluxes. For instance, we find at 744 au for 1 GeV energy cosmic rays, the intensity of Galactic cosmic rays when drift is considered is two orders of magnitude higher when compared with no drift.

Overall, particle drift is an important ingredient in cosmic ray modulation, particularly when $|\langle v_d \rangle| > u$. Here, we fixed ϕ and θ values as previously discussed. However, we can expect that the presence of particle drift will affect the cosmic ray modulation of Prox Cen and ‘AU Mic high’ at any given location of the equatorial plane. This is due to the fact that particle drift changes the modulation of cosmic ray even in the direction where the wind have the strongest velocity.

5.5 Discussion & Conclusions

In this paper, we investigated the intensity of Galactic cosmic rays within the astrospheres of two planetary systems: AU Mic and Prox Cen. AU Mic hosts two known close-in Neptune-size exoplanets. Prox Cen is our closest star and has a known Earth-size exoplanet orbiting within the habitable zone. We used a 1D cosmic ray transport model which includes the effect of particle drift to calculate the cosmic ray fluxes reaching the exoplanets and the habitable zones. The radial particle drift velocity is calculated using 3D MHD stellar wind models for Prox Cen, AU Mic (with a ‘low’ and ‘high’ mass loss rate) and the Sun for comparison (Kavanagh et al., 2021, see also Section 5.A). This is the first time that radial drift velocities have been quantified for M dwarf systems.

Overall, the inclusion of particle drift velocities, due to gradients and curvatures of the stellar magnetic field, has a significant effect on the propagation of Galactic cosmic rays. In general, a negative drift velocity results in a larger intensity of cosmic rays and a positive drift velocity results in a reduction of cosmic rays. This is because the particle drift acts simply as an extra advective process in the transport model. In the two systems studied here, the drift velocity is negative at the cut where we investigated the flux of Galactic cosmic rays. Prox Cen and ‘AU Mic high’ both have a larger negative drift velocity while for ‘AU Mic low’ the drift velocity is rather slow for cosmic rays with 1 GeV/c momentum. Consequently, the modulation of cosmic rays is significantly affected by the inclusion of drift for Prox Cen and ‘AU Mic high’ but only slightly affected in the case of ‘AU Mic low’.

For Prox Cen, at 1 au (green dashed line in Fig. 5.3) the Galactic cosmic ray fluxes are larger in comparison to Earth. This is because Prox Cen’s magnetic field profile is weaker at larger distances (e.g., from 1 au to the astrosphere edge) in comparison to the solar system and results in less suppression of Galactic cosmic rays for the same distance. In contrast, both AU Mic scenarios (low and high) have a much stronger

stellar magnetic field profile in comparison to the solar system, resulting in an intense suppression of Galactic cosmic rays at the same distance.

Herbst et al. (2020) have also investigated the Galactic cosmic ray fluxes at Prox Cen b, albeit without considering the effects of particle drift. They found that cosmic rays were not effectively reduced in comparison to the LIS. In contrast, our results show lower cosmic ray fluxes at Prox Cen b. For instance, compared to Herbst et al. (2020), the cosmic ray fluxes at Prox Cen b with energy 1 GeV is 7 times smaller in our simulations when particle drift is not included and 5 times smaller when particle drift is included. The differences in our results and Herbst et al. (2020) is likely to be related to the different wind and ISM properties used and the cosmic ray transport properties. They used a surface magnetic field strength of ~ 600 G measured from Zeeman broadening (Reiners & Basri, 2008) and a wind velocity of 1500 km s^{-1} based on MHD simulations (Garraffo et al., 2016). Both quantities are higher than the values we used. We also calculate different astrosphere sizes, 122 au (Herbst et al., 2020) versus 75 au in our work, as a result of our different wind and ISM properties. If the drift velocities for Prox Cen used in our work were included in Herbst et al. (2020) work, they would probably find an even larger flux of Galactic cosmic rays than the values they calculate for Prox Cen b.

In the case of AU Mic, we showed that our lack of a strong constraint for the wind properties (mass-loss rate and wind velocity) strongly affects the intensity of Galactic cosmic rays calculated for the system and the size of the astrosphere (980–6140 au). This is in contrast with the results found by Mesquita et al. (2021) for GJ 436, in which the lack of knowledge of u and \dot{M} did not strongly affect the flux of Galactic cosmic rays in the system. This is related to the physical process that is more dominant (Rodgers-Lee et al., 2021b). While GJ 436 is dominated by diffusion which leads to little (or no) modulation of cosmic rays, AU Mic is dominated by advection processes which strongly suppress cosmic rays. Interestingly, AU Mic is dominated by advective processes even without the inclusion of the particle drift. Additionally, because ‘AU Mic high’ has a larger astrosphere size the Galactic cosmic rays have further to travel through a region of the stellar wind dominated by advection in comparison with ‘AU Mic low’.

In addition to drift effects, the stellar magnetic field and the wind velocity are important ingredients to effectively modulate the Galactic cosmic ray fluxes throughout the astrosphere. A strong stellar magnetic field, leading to smaller diffusion coefficients, combined with a fast stellar wind velocity is effective at suppressing the propagation of Galactic cosmic rays inside the astrosphere. The magnetic field intensity can change if the star has an activity cycle, similar to the solar cycle (see e.g. Hathaway, 2010). When

the Sun is at activity minimum the intensity of Galactic cosmic rays is higher than at activity maximum (Potgieter, 2013), with more than an order of magnitude difference in flux, depending on the cosmic ray energy (Vos & Potgieter, 2015). Prox Cen, similarly to the Sun, has been suggested to have a 7 year activity cycle (e.g. Yadav et al., 2016). The magnetic map adopted in our wind model was derived near its activity maximum (Klein et al., 2021a). This could imply that during its activity minimum Prox Cen would likely experience a higher flux of Galactic cosmic rays than the results presented here. In addition, the particle drift will also vary with activity cycle since it depends on the magnetic field geometry.

Another important aspect to consider is that stars themselves can accelerate stellar cosmic rays during events such as flares and coronal mass ejections (Rodgers-Lee et al., 2021a). Prox Cen and AU Mic are both active stars with strong surface magnetic fields (Klein et al., 2021a,b) and frequent flaring activity (Gilbert et al., 2021, 2022) and, as such, they should be efficient at accelerating stellar cosmic rays. As a result, for these stars, stellar cosmic ray fluxes will dominate over Galactic cosmic rays up to a certain energy. Some works have explored the effect of such events for the exoplanets in the AU Mic and Prox Cen systems. Scheucher et al. (2020) showed that a strong stellar cosmic ray event would be able to heat the otherwise cold planet Prox Cen b, playing an important role in the planet’s habitability. Recently, Carolan et al. (2020) investigated the effects of strong stellar winds in the atmospheric evaporation of AU Mic b. They concluded that, even when atmospheric erosion by the stellar wind is not significant, the geometry and ionisation of the escaping atmosphere can change substantially, impacting the interpretation/prediction of spectroscopic transit observations. In addition to strong winds, coronal mass ejections and flares can also affect planetary atmospheres, by increasing atmospheric erosion (Khodachenko et al., 2007; Hazra et al., 2020, 2022). Although these processes are episodic, they are expected to be more frequent and more energetic in young and/or active stars (Aarnio et al., 2014), such as AU Mic.

To better account for the full 3D nature of planetary systems, 2D/3D cosmic ray transport models should be used, similar to models implemented for the solar system. Although the radial drift velocity varies with the polar and azimuthal angles, which we have neglected, it is possible with 2D/3D simulations that diffusion could smooth these variations, resulting in a more continuous distribution of cosmic rays. In this case, the differential intensity might not be too different than the ones we calculated with our model. The polar and azimuthal drift velocities may also act in a similar way.

Finally, the Galactic cosmic rays fluxes at the exoplanets’ orbits can be used to further investigate the intensity of Galactic cosmic rays in planetary atmospheres and

in atmospheric chemistry models. Our models can also be used to understand future observations of exoplanet atmospheres with instruments such as JWST and ARIEL.

Acknowledgements

This project has received funding from the European Research Council (ERC) under the European Union’s Horizon 2020 research and innovation programme (grant agreement No 817540, ASTROFLOW). DRL would like to acknowledge that this publication has emanated from research conducted with the financial support of Science Foundation Ireland under Grant number 21/PATH-S/9339. The authors wish to acknowledge the SFI/HEA Irish Centre for High-End Computing (ICHEC) for the provision of computational facilities and support.

5.A Galactic cosmic ray propagation in the solar system

In order to benchmark our code we calculate Galactic cosmic ray propagation through the heliosphere. Here we explain the solar wind model and the results we obtain at Earth.

To model the solar wind plasma, we follow the same methodologies as in Kavanagh et al. (2021). Unlike AU Mic and Prox Cen, the mass-loss rate of the solar wind has been measured in-situ to be $2 \times 10^{-14} M_{\odot} \text{ yr}^{-1}$ (Cohen, 2011). The mass-loss rate of the wind is sensitive to the value used for the Alfvén wave flux per unit magnetic field strength S_A/B in the chromosphere (Boro Saikia et al., 2020; Kavanagh et al., 2021). For the Sun, this value has been estimated directly from observations to be $1.1 \times 10^5 \text{ erg s}^{-1} \text{ cm}^{-2} \text{ G}^{-1}$ (Sokolov et al., 2013).

Using this value, with the remaining Alfvén wave inputs being the same as those in Kavanagh et al. (2021), we model the solar wind using a dipolar magnetic field with a polar strength of 3 G, tilted 5° with respect to the rotation axis. Our 3D spherical grid extends out to 20 solar radii, and contains around 4.5 million cells. The solar wind model used here is representative of solar minimum with the heliospheric magnetic field pointing outwards in the northern solar hemisphere (commonly referred to as $A > 0$ cycles). The mass-loss rate we obtain from our model is $\sim 3 \times 10^{-14} M_{\odot} \text{ yr}^{-1}$ and the solar wind terminal velocity is 540 km s^{-1} (which is in the range of observed values, e.g. McComas et al., 2000). By extrapolating the magnetic field strength of the 3D model from its outer edge to 1 au, we found a magnetic field strength at Earth’s orbit

of ~ 4 nT (which is in the range of observed values, e.g. Potgieter et al., 2015b). We set the size of the heliosphere to 122 au, as observed by *Voyager 1* (Stone et al., 2013, 2019). Fig. 5.6 shows the solar wind velocity (left) and total magnetic field intensity (right) throughout the heliosphere. The total magnetic field resembles an \sim aligned dipole, with a bimodal wind velocity distribution typical of solar wind at minimum (McComas et al., 2000). Using this model, we calculate the propagation of Galactic cosmic rays as discussed in Section 5.2.3. The flux of cosmic rays found at Earth is shown as red dots in Fig. 5.7 as a function of the kinetic energy.

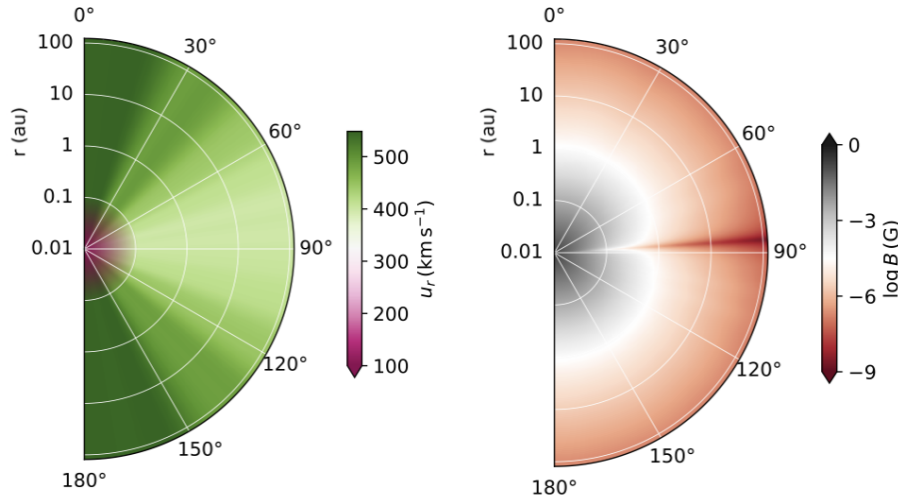


Figure 5.6: *Left:* Equatorial plane cut of the solar wind velocity. *Right:* Equatorial plane cut of the magnitude of the total magnetic field for the full radial extent of the heliosphere. The values shown for small orbital distances are from the 3D solar wind model and the values shown at large distances are an extrapolation (see Section 5.B for details).

Fig. 5.7 shows the differential intensity of Galactic cosmic rays at Earth as a function of kinetic energy during the solar minimum activity and $A > 0$ for different works, namely: this study (red dots), Strauss & Potgieter (2014) (green dashed line), Strauss & Potgieter (2014) (magenta dash-dotted line) and Potgieter & Vos (2017) (blue dotted line). Overall, we get remarkably good agreement between our model and the 3D models to which we compare our results. The main discrepancies are most likely related to the different values of B , u_∞ and heliospheric sizes used in each model and the fact that we use a 1D cosmic ray transport model while the other works use 3D models.

Another point to note is that Potgieter & Vos (2017) uses a ‘softening parameter’ in the drift velocity equation so that the drift is reduced for cosmic rays with momentum

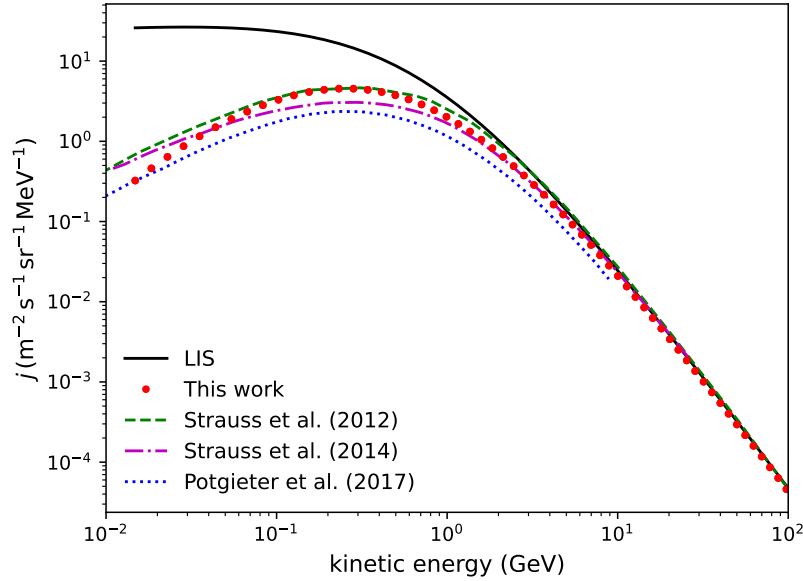


Figure 5.7: Differential intensity of Galactic cosmic rays as a function of kinetic energy at Earth representative of solar minimum conditions. The different linestyles represent different models for comparison, namely: red dots for this study, green dashed line for Strauss & Potgieter (2014), magenta dash-dotted line for Strauss & Potgieter (2014) and blue dotted line for Potgieter & Vos (2017).

below $0.55 \text{ GeV}/c$. This reduction in the particle drift is necessary to explain the observations at Earth. In our models, we did not use a ‘softening parameter’ to reduce the particle drift velocities to avoid including an extra free parameter in to our model.

5.B Extrapolation of stellar wind profiles to the edge of the astrosphere

The outer boundary of the stellar wind models for AU Mic and Prox Cen from Kavanagh et al. (2021) is at $100 R_\star$, however the astrosphere extends much further out. Hence, we extrapolate the quantities u , B_r , B_θ and B_ϕ to account for the whole extent of the astrosphere. Beyond $100 R_\star$, the radial velocity is extrapolated as a constant since the velocity has already reached its asymptotic value. To generate a Parker spiral (Parker, 1958), B_r continues to fall with r^{-2} and B_ϕ with r^{-1} . In the case of B_θ , we use a power law fit for each system. For Prox Cen, B_θ falls with $r^{-1.7}$, for ‘AU Mic low’ with $r^{-2.2}$ and for ‘AU Mic high’ with $r^{-4.7}$. For the Sun we extrapolate B_θ as $1/r^{4.6}$ beyond $r > 0.04 \text{ au}$. Figs. 5.1 and 5.6 show the extrapolated values of the wind velocity and total magnetic field for the stars studied here. Note, our stellar wind model does

5.B Extrapolation of stellar wind profiles to the edge of the astrosphere

not take into account the termination shock (region where the stellar wind properties change due to the interactions with the local interstellar medium).

Bibliography

- Aarnio A. N., Stassun K. G., Matt S. P., 2014, *Proceedings of the International Astronomical Union*, 8, 318–122
- Agostinelli S., et al., 2003, *Nuclear Instruments and Methods in Physics Research A*, 506, 250–96
- Aharonian F. A., et al., 2004, *Nature*, 432, 75–18, 56
- Aharonian F., Peron G., Yang R., Casanova S., Zanin R., 2020, *Phys. Rev. D*, 101, 083018–22, 62, 76
- Airapetian V. S., Glocer A., Gronoff G., Hébrard E., Danchi W., 2016, *Nature Geoscience*, 9, 452–18, 57, 81, 102, 106
- Ajello M., et al., 2014, *Astrophysical Journal*, 789, 20–18
- Alfvén H., 1942, *Nature*, 150, 405–13, 31
- Alves Batista R., et al., 2019, *Frontiers in Astronomy and Space Sciences*, 6, 23–18
- Anglada-Escudé G., et al., 2016, *Nature*, 536, 437–4, 107, 109
- Aschwanden M. J., Poland A. I., Rabin D. M., 2001, *Annual Review of Astronomy and Astrophysics*, 39, 175–42
- Astudillo-Defru N., et al., 2017, *Astronomy & Astrophysics*, 602, A88–84, 96
- Atri D., 2016, *J. R. Soc. Interface*, 13–18, 57, 81
- Atri D., 2017, *Monthly Notices of the Royal Astronomical Society*, 465, L34–19, 58, 91, 96, 113
- Atri D., 2020, *Monthly Notices of the Royal Astronomical Society*, 492, L28–19, 58, 81, 96
- Atri D., Hariharan B., Grießmeier J.-M., 2013, *Astrobiology*, 13, 910–19, 58
- Atri D., MacArthur C., Dobbs-Dixon I., 2020, *arXiv e-prints*, p. arXiv:2012.00568–19, 81

BIBLIOGRAPHY

- Baghmanyany V., Peron G., Casanova S., Aharonian F., Zanin R., 2020, *Astrophysical Journal Letters*, 901, L4 22, 23, 62, 76
- Barth P., et al., 2021, *Monthly Notices of the Royal Astronomical Society*, 502, 6201 18, 24, 27, 57, 81, 101, 106, 113
- Bibring J.-P., et al., 2006, *Science*, 312, 400 3
- Blasi P., 2014, *Comptes Rendus Physique*, 15, 329 18, 56
- Boro Saikia S., Jin M., Johnstone C. P., Lüftinger T., Güdel M., Airapetian V. S., Kislyakova K. G., Folsom C. P., 2020, *Astronomy & Astrophysics*, 635, A178 123
- Bourrier V., Lecavelier des Etangs A., 2013, *Astronomy & Astrophysics*, 557, A124 11
- Bourrier V., Ehrenreich D., Lecavelier des Etangs A., 2015, *Astronomy & Astrophysics*, 582, A65 59, 64, 67
- Bourrier V., Lecavelier des Etangs A., Ehrenreich D., Tanaka Y. A., Vidotto A. A., 2016, *Astronomy & Astrophysics*, 591, A121 44, 45, 50, 59
- Bourrier V., et al., 2018, *Nature*, 553, 477 59, 64
- Brose R., Pohl M., Sushch I., Petruk O., Kuzyo T., 2020, *Astronomy & Astrophysics*, 634, A59 18, 56
- Browning M. K., 2008, *Astrophysical Journal*, 676, 1262 5
- Butler R. P., Vogt S. S., Marcy G. W., Fischer D. A., Wright J. T., Henry G. W., Laughlin G., Lissauer J. J., 2004, *Astrophysical Journal*, 617, 580 59, 64
- Carolan S., Vidotto A. A., Plavchan P., Villarreal D'Angelo C., Hazra G., 2020, *Monthly Notices of the Royal Astronomical Society*, 498, L53 122
- Cauley P. W., Shkolnik E. L., Llama J., Lanza A. F., 2019, *Nature Astronomy*, 3, 1128 100
- Chabrier G., Baraffe I., 1997, *Astronomy & Astrophysics*, 327, 1039 5
- Charbonneau P., 2014, *Annual Review of Astronomy & Astrophysics*, 52, 251 5, 6
- Chiang E., Fung J., 2017, *Astrophysical Journal*, 848, 4 107
- Cohen O., 2011, *Monthly Notices of the Royal Astronomical Society*, 417, 2592 123

- Cohen O., 2017, *Astrophysical Journal*, 835, 220–46
- Cohen O., Drake J. J., Kóta J., 2012, *Astrophysical Journal*, 760, 85–24, 56, 61, 82, 91, 102, 107, 113
- Collier Cameron A., Robinson R. D., 1989, *Monthly Notices of the Royal Astronomical Society*, 236, 57–11
- Cranmer S. R., 2009, *Living Reviews in Solar Physics*, 6, 3–13
- Cranmer S. R., Winebarger A. R., 2019, *Annual Review of Astronomy & Astrophysics*, 57, 157–13, 63
- Cummings A. C., et al., 2016, *Astrophysical Journal*, 831, 18–21, 62, 92
- Czesla S., Schröter S., Wolter U., von Essen, C. Huber, K. F. Schmitt, J. H. M. M. Reichart, D. E. Moore, J. P. 2012, *A&A*, 539, A150–42, 43
- Dartnell L. R., 2011, *Astrobiology*, 11, 551–18, 19, 58, 81
- De Moortel I., Browning P., 2015, *Philosophical Transactions of the Royal Society of London Series A*, 373, 20140269–15, 31
- De Pontieu B., et al., 2007, *Science*, 318, 1574–86
- Díaz R. F., et al., 2019, *Astronomy & Astrophysics*, 625, A17–84
- Donati J.-F., Forveille T., Collier Cameron A., Barnes J. R., Delfosse X., Jardine M. M., Valenti J. A., 2006, *Science*, 311, 633–7
- Donati J. F., et al., 2008, *Monthly Notices of the Royal Astronomical Society*, 390, 545–7
- Ehrenreich D., et al., 2015, *Nature*, 522, 459–43, 59, 63, 74
- Enomoto R., et al., 2002, *Nature*, 416, 823–18, 56
- Fatuzzo M., Adams F. C., Melia F., 2006, *Astrophysical Journal Letters*, 653, L49–23, 76
- Fichtinger B., Güdel M., Mutel R. L., Hallinan G., Gaidos E., Skinner S. L., Lynch C., Gayley K. G., 2017, *Astronomy & Astrophysics*, 599, A127–11, 30, 58, 81

BIBLIOGRAPHY

- Fouqué P., et al., 2018, *Monthly Notices of the Royal Astronomical Society*, 475, 1960 111
- Fraschetti F., Drake J. J., Alvarado-Gómez J. D., Moschou S. P., Garraffo C., Cohen O., 2019, *Astrophysical Journal*, 874, 21 24, 57, 77, 81, 95
- Gaia Collaboration 2020, VizieR Online Data Catalog, p. I/350 111
- Gaidos E. J., Güdel M., Blake G. A., 2000, *Geophysical Research Letters*, 27, 501 11
- Gardner J. P., et al., 2006, *Space Science Reviews*, 123, 485 24, 101, 106
- Garraffo C., Drake J. J., Cohen O., 2016, *Astrophysical Journal Letters*, 833, L4 30, 63, 121
- Gary G. A., 2001, *Solar Physics*, 203, 71 42
- Gilbert E. A., Barclay T., Kruse E., Quintana E. V., Walkowicz L. M., 2021, *Frontiers in Astronomy and Space Sciences*, 8, 190 122
- Gilbert E. A., et al., 2022, *Astronomical Journal*, 163, 147 122
- Gillon M., et al., 2017, *Nature*, 542, 456 4
- Gleeson L. J., Axford W. I., 1968, *Astrophysical Journal*, 154, 1011 73
- González-Álvarez E., et al., 2020, *Astronomy & Astrophysics*, 637, A93 83, 84
- Gough D. O., 1981, *Solar Physics*, 74, 21 3
- Grenfell J. L., et al., 2007, *Astrobiology*, 7, 208 19, 58
- Grenfell J. L., et al., 2012, *Astrobiology*, 12, 1109 24, 57, 77, 81, 95
- Grenfell J. L., et al., 2013, *Astrobiology*, 13, 415 5, 57
- Grißmeier J. M., Stadelmann A., Motschmann U., Belisheva N. K., Lammer H., Biernat H. K., 2005, *Astrobiology*, 5, 587 5, 57, 80, 106, 107
- Grißmeier J. M., Stadelmann A., Grenfell J. L., Lammer H., Motschmann U., 2009, *Icarus*, 199, 526 19, 58
- Grißmeier J. M., Tabataba-Vakili F., Stadelmann A., Grenfell J. L., Atri D., 2015, *Astronomy & Astrophysics*, 581, A44 19, 58, 113

- Griestmeier J. M., Tabataba-Vakili F., Stadelmann A., Grenfell J. L., Atri D., 2016, *Astronomy & Astrophysics*, 587, A159 19, 58
- Guinan E. F., Engle S. G., Durbin A., 2016, *Astrophysical Journal*, 821, 81 5, 57, 80
- Hartmann L., MacGregor K. B., 1980, *Astrophysical Journal*, 242, 260 14, 31, 32
- Hathaway D. H., 2010, *Living Reviews in Solar Physics*, 7, 1 6, 121
- Hazra G., Vidotto A. A., D’Angelo C. V., 2020, *Monthly Notices of the Royal Astronomical Society*, 496, 4017 122
- Hazra G., Vidotto A. A., Carolan S., Villarreal D’Angelo C., Manchester W., 2022, *Monthly Notices of the Royal Astronomical Society*, 509, 5858 122
- Hébrard É. M., Donati J. F., Delfosse X., Morin J., Moutou C., Boisse I., 2016, *Monthly Notices of the Royal Astronomical Society*, 461, 1465 7
- Helling C., Rimmer P. B., 2019, *Philosophical Transactions of the Royal Society of London Series A*, 377, 20180398 24, 106
- Helling C., Rimmer P. B., Rodriguez-Barrera I. M., Wood K., Robertson G. B., Stark C. R., 2016, *Plasma Physics and Controlled Fusion*, 58, 074003 101
- Henry T. J., Jao W.-C., Subasavage J. P., Beaulieu T. D., Ianna P. A., Costa E., Méndez R. A., 2006, *Astronomical Journal*, 132, 2360 4, 80
- Henry T. J., et al., 2018, *Astronomical Journal*, 155, 265 4, 80
- Herbst K., et al., 2020, *Astrophysical Journal Letters*, 897, L27 17, 23, 56, 75, 76, 82, 92, 106, 107, 121
- Hoehler T. M., Som S. M., Kiang N. Y., 2018, in Deeg H. J., Belmonte J. A., eds, , *Handbook of Exoplanets*. Springer International Publishing, Cham, Switzerland, pp 2795–2816, doi:10.1007/978-3-319-55333-7_74 2
- Holzer T. E., Fla T., Leer E., 1983, *Astrophysical Journal*, 275, 808 31
- Howard A. W., et al., 2014, *Astrophysical Journal*, 794, 51 84
- Ip W.-H., Kopp A., Hu J.-H., 2004, *Astrophysical Journal Letters*, 602, L53 100

BIBLIOGRAPHY

- Jardine M., Collier Cameron A., 2019, *Monthly Notices of the Royal Astronomical Society*, 482, 2853 9, 11, 12, 30, 58, 81
- Jasinski J. M., Nordheim T. A., Hasegawa Y., Murphy N., 2020, *Astrophysical Journal Letters*, 899, L18 16, 56, 67, 74, 75
- Jatenco-Pereira V., Opher R., 1989, *Astronomy & Astrophysics*, 209, 327 32, 85
- Jeffers S. V., et al., 2020, *Science*, 368, 1477 84
- Jin M., Manchester W. B., van der Holst B., Sokolov I., Tóth G., Vourlidas A., de Koning C. A., Gombosi T. I., 2017, *Astrophysical Journal*, 834, 172 108
- Johnstone C. P., et al., 2015, *Astrophysical Journal Letters*, 815, L12 8, 30, 41, 80
- Jokipii J. R., 1966, *Astrophysical Journal*, 146, 480 61, 91, 113
- Jokipii J. R., Levy E. H., Hubbard W. B., 1977, *Astrophysical Journal*, 213, 861 107
- Jokipii J. R., Kota J., Merenyi E., 1993, *Astrophysical Journal*, 405, 782 114
- Kafexhiu E., Romoli C., Taylor A. M., Aharonian F., 2018, *Astrophysical Journal*, 864, 148 18
- Kasting J. F., Whitmire D. P., Reynolds R. T., 1993, *Icarus*, 101, 108 2, 4, 30, 57, 71, 80, 106
- Kavanagh R. D., et al., 2019, *Monthly Notices of the Royal Astronomical Society*, 485, 4529 74
- Kavanagh R. D., Vidotto A. A., Klein B., Jardine M. M., Donati J.-F., Ó Fionnagáin D., 2021, *Monthly Notices of the Royal Astronomical Society*, 504, 1511 63, 100, 107, 108, 109, 110, 117, 118, 120, 123, 125
- Khodachenko M. L., et al., 2007, *Astrobiology*, 7, 167 5, 30, 57, 80, 122
- Khodachenko M. L., Shaikhislamov I. F., Lammer H., Berezutsky A. G., Miroshnichenko I. B., Rumenskikh M. S., Kislyakova K. G., Dwivedi N. K., 2019, *The Astrophysical Journal*, 885, 67 46, 52
- Kirkby J., et al., 2011, *Nature*, 476, 429 18, 58, 81

- Kislyakova K. G., Holmström M., Lammer H., Odert P., Khodachenko M. L., 2014, *Science*, 346, 981–11
- Kislyakova K. G., et al., 2019, *A&A*, 623, A131–46, 52, 58, 81
- Klein B., Donati J.-F., Hébrard É. M., Zaire B., Folsom C. P., Morin J., Delfosse X., Bonfils X., 2021a, *Monthly Notices of the Royal Astronomical Society*, 500, 1844–6, 7, 8, 107, 108, 109, 122
- Klein B., et al., 2021b, *Monthly Notices of the Royal Astronomical Society*, 502, 188–107, 108, 109, 122
- Knutson H. A., et al., 2011, *Astrophysical Journal*, 735, 27–59, 64
- Kochukhov O., 2021, *Astronomy & Astrophysics Review*, 29, 1–5, 7
- Kopp A., Raath J. L., Fichtner H., Potgieter M. S., Ferreira S. E. S., Heber B., 2021, *Astrophysical Journal*, 922, 124–107
- Kopparapu R. K., Ramirez R. M., SchottelKotte J., Kasting J. F., Domagal-Goldman S., Eymet V., 2014, *Astrophysical Journal Letters*, 787, L29–93, 109
- Kraft R. P., 1967, *Astrophysical Journal*, 150, 551–34
- Kuin N. P. M., Hearn A. G., 1982, *Astronomy & Astrophysics*, 114, 303–48
- Kulow J. R., France K., Linsky J., Loyd R. O. P., 2014, *Astrophysical Journal*, 786, 132–59
- Lamers H. J. G. L. M., Cassinelli J. P., 1999, *Introduction to Stellar Winds*. Cambridge University Press, doi:10.1017/CBO9781139175012–8
- Lammer H., et al., 2007, *Astrobiology*, 7, 185–5, 57, 80
- Lang P., Jardine M., Morin J., Donati J. F., Jeffers S., Vidotto A. A., Fares R., 2014, *Monthly Notices of the Royal Astronomical Society*, 439, 2122–30
- Lim J., White S. M., 1996, *Astrophysical Journal Letters*, 462, L91–11, 30, 58, 81
- MacGregor K. B., Charbonneau P., 1994, *Astrophysical Journal*, 430, 387–32
- Marquardt J., Heber B., 2019, *Astronomy & Astrophysics*, 625, A153–94, 102

BIBLIOGRAPHY

- Martioli E., Hébrard G., Correia A. C. M., Laskar J., Lecavelier des Etangs A., 2021, *Astronomy & Astrophysics*, 649, A177–107
- Matt S. P., Brun A. S., Baraffe I., Bouvier J., Chabrier G., 2015, *Astrophysical Journal Letters*, 799, L23–8, 30, 41, 80
- McComas D. J., et al., 2000, *Journal of Geophysical Research*, 105, 10419–123, 124
- Meadows V. S., Barnes R. K., 2018, in Deeg H. J., Belmonte J. A., eds, , *Handbook of Exoplanets*. Springer International Publishing, Cham, Switzerland, pp 2771–2794, doi:10.1007/978-3-319-55333-7_57–1, 2, 80, 106
- Meadows V. S., et al., 2018, *Astrobiology*, 18, 630–82
- Mesquita A. L., Vidotto A. A., 2020, *Monthly Notices of the Royal Astronomical Society*, 494, 1297–25, 58, 62, 63, 64, 65, 74, 77, 81, 82, 85, 86
- Mesquita A. L., Rodgers-Lee D., Vidotto A. A., 2021, *Monthly Notices of the Royal Astronomical Society*, 505, 1817–1826–17, 23, 25, 82, 90, 92, 93, 100, 101, 105, 106, 107, 112, 113, 118, 119, 121
- Mesquita A. L., Rodgers-Lee D., Vidotto A. A., Atri D., Wood B. E., 2022a, *Monthly Notices of the Royal Astronomical Society*, 509, 2091–17, 23, 26, 105, 106, 107, 108, 112, 113, 114
- Mesquita A. L., Rodgers-Lee D., Vidotto A. A., Kavanagh R. D., 2022b, *Monthly Notices of the Royal Astronomical Society*, 515, 1218–17, 23, 27
- Miller S. L., 1953, *Science*, 117, 528–27
- Mischna M. A., Kasting J. F., Pavlov A., Freedman R., 2000, *Icarus*, 145, 546–4
- Morin J., 2012, in Reylé C., Charbonnel C., Schultheis M., eds, *EAS Publications Series Vol. 57*, *EAS Publications Series*. pp 165–191, doi:10.1051/eas/1257005–6, 7, 86
- Morin J., et al., 2008a, *Monthly Notices of the Royal Astronomical Society*, 384, 77–7
- Morin J., et al., 2008b, *Monthly Notices of the Royal Astronomical Society*, 390, 567–7
- Morin J., Donati J. F., Petit P., Delfosse X., Forveille T., Jardine M. M., 2010, *Monthly Notices of the Royal Astronomical Society*, 407, 2269–5, 6, 7, 30, 57, 74, 80

- Moutou C., et al., 2017, *Monthly Notices of the Royal Astronomical Society*, 472, 4563 7, 86
- Mullan D. J., MacDonald J., 2001, *Astrophysical Journal*, 559, 353 5
- Müller H.-R., Frisch P. C., Florinski V., Zank G. P., 2006, *Astrophysical Journal*, 647, 1491 16, 24, 56, 66, 74, 82
- Neronov A., Malyshev D., Semikoz D. V., 2017, *Astronomy & Astrophysics*, 606, A22 3, 22, 62, 76, 92, 113
- Padovani M., et al., 2020, *Space Science Reviews*, 216, 29 81, 92
- Pagano P., De Moortel I., 2019, *Astronomy & Astrophysics*, 623 14
- Panagia N., Felli M., 1975, *Astronomy & Astrophysics*, 39, 1 11, 30, 58, 81
- Parker E. N., 1958, *Astrophysical Journal*, 128, 664 13, 30, 65, 88, 125
- Parker E. N., 1965, *Planetary and Space Science*, 13, 9 18, 59, 60, 90, 112
- Pevtsov A. A., Fisher G. H., Acton L. W., Longcope D. W., Johns-Krull C. M., Kankelborg C. C., Metcalf T. R., 2003, *Astrophysical Journal*, 598, 1387 7, 9
- Pinamonti M., et al., 2018, *Astronomy & Astrophysics*, 617, A104 83, 84
- Plavchan P., et al., 2020, *Nature*, 582, 497 107, 109
- Pollack J. B., Kasting J. F., Richardson S. M., Poliakoff K., 1987, *Icarus*, 71, 203 3
- Potgieter M. S., 2013, *Living Reviews in Solar Physics*, 10, 3 18, 20, 22, 24, 27, 56, 106, 107, 122
- Potgieter M. S., Vos E. E., 2017, *Astronomy & Astrophysics*, 601, A23 20, 107, 124, 125
- Potgieter M. S., Vos E. E., Munini R., Boezio M., Di Felice V., 2015a, *Astrophysical Journal*, 810, 141 24, 102
- Potgieter M. S., Vos E. E., Munini R., Boezio M., Di Felice V., 2015b, *Astrophysical Journal*, 810, 141 124
- Prokhorov D. A., Colafrancesco S., 2018, *Monthly Notices of the Royal Astronomical Society*, 478, 2939 76

BIBLIOGRAPHY

- Prokopyshyn A. P. K., Hood A. W., De Moortel I., 2019, *Astronomy & Astrophysics*, 624 15
- Rab C., Güdel M., Padovani M., Kamp I., Thi W. F., Voitke P., Aresu G., 2017, *Astronomy & Astrophysics*, 603, A96 81
- Recchia S., Phan V. H. M., Biswas S., Gabici S., 2019, *Monthly Notices of the Royal Astronomical Society*, 485, 2276 92
- Redfield S., Linsky J. L., 2000, *Astrophysical Journal*, 534, 825 16, 67
- Redfield S., Linsky J. L., 2008, *Astrophysical Journal*, 673, 283 67, 111
- Reiners A., Basri G., 2008, *Astronomy & Astrophysics*, 489, L45 7, 121
- Reiners A., et al., 2022, arXiv e-prints, p. arXiv:2204.00342 5, 7
- Rimmer P. B., Helling C., 2013, *Astrophysical Journal*, 774, 108 5, 57, 91, 113
- Rimmer P. B., Helling C., Bilger C., 2014, *International Journal of Astrobiology*, 13, 173 5, 18, 57, 81, 102
- Rodgers-Lee D., Taylor A. M., Ray T. P., Downes T. P., 2017, *Monthly Notices of the Royal Astronomical Society*, 472, 26 81
- Rodgers-Lee D., Vidotto A. A., Taylor A. M., Rimmer P. B., Downes T. P., 2020, *Monthly Notices of the Royal Astronomical Society*, 499, 2124 17, 24, 56, 59, 60, 61, 69, 72, 73, 82, 90, 91, 93, 102, 107, 112, 113
- Rodgers-Lee D., Taylor A. M., Vidotto A. A., Downes T. P., 2021a, *Monthly Notices of the Royal Astronomical Society*, 504, 1519 27, 57, 77, 81, 95, 122
- Rodgers-Lee D., Vidotto A. A., Mesquita A. L., 2021b, *Monthly Notices of the Royal Astronomical Society*, 508, 4696 17, 18, 23, 82, 100, 101, 106, 107, 113, 114, 119, 121
- Rosenthal L. J., et al., 2021, *The Astrophysical Journal Supplement Series*, p. 8 84
- Route M., 2016, *Astrophysical Journal Letters*, 830, L27 5
- Sadovskii A. M., Struminsky A. B., Belov A., 2018, *Astronomy Letters*, 44, 324 23, 56, 82, 106
- Sakaue T., Shibata K., 2021, *Astrophysical Journal Letters*, 906, L13 63

- Saur J., Grambusch T., Duling S., Neubauer F. M., Simon S., 2013, *Astronomy & Astrophysics*, 552, A119 44, 100
- Scalo J., et al., 2007, *Astrobiology*, 7, 85 5, 57, 80
- Schatzman E., 1949, *Annales d'Astrophysique*, 12, 203 13, 31
- Scherer K., Fichtner H., Stawicki O., 2002, *Journal of Atmospheric and Solar-Terrestrial Physics*, 64, 795 16, 23, 56, 65, 82
- Scherer K., Fichtner H., Heber B., Ferreira S. E. S., Potgieter M. S., 2008, *Advances in Space Research*, 41, 1171 16, 23, 56, 66, 82
- Scheucher M., Grenfell J. L., Wunderlich F., Godolt M., Schreier F., Rauer H., 2018, *Astrophysical Journal*, 863, 6 5, 57
- Scheucher M., et al., 2020, *Astrophysical Journal*, 893, 12 24, 57, 77, 81, 95, 122
- Schlickeiser R., 1989, *Astrophysical Journal*, 336, 243 61, 91, 113
- Schure K. M., Kosenko D., Kaastra J. S., Keppens R., Vink J., 2009, *A&A*, 508, 751 33
- See V., et al., 2015, *Monthly Notices of the Royal Astronomical Society*, 453, 4301 107
- See V., et al., 2019, *The Astrophysical Journal*, 876, 118 30
- Segura A., Walkowicz L. M., Meadows V., Kasting J., Hawley S., 2010, *Astrobiology*, 10, 751 24, 57, 77, 81, 95
- Selsis F., Kasting J. F., Levrard B., Paillet J., Ribas I., Delfosse X., 2007, *Astronomy & Astrophysics*, 476, 1373 2, 3, 4, 30, 57, 71, 80, 106
- Shaviv N. J., 2002, *Physical Review Letters*, 89, 051102 18, 58, 81
- Shaviv N. J., 2003, *New Astronomy*, 8, 39 18, 58, 81
- Shea M. A., Smart D. F., 2000, *Space Science Reviews*, 93, 187 58, 81
- Shields A. L., Ballard S., Johnson J. A., 2016, *Physics Reports*, 663, 1 90
- Shkolnik E., Bohlender D. A., Walker G. A. H., Collier Cameron A., 2008, *Astrophysical Journal*, 676, 628 100

BIBLIOGRAPHY

- Shulyak D., et al., 2019, *Astronomy & Astrophysics*, 626, A86 5, 30, 57, 80
- Sokolov I. V., et al., 2013, *Astrophysical Journal*, 764, 23 123
- Solomon S. C., Head J. W., 1991, *Science*, 252, 252 3
- Sridharan D. M., et al., 2016, *Life Sciences and Space Research*, 9, 19 19, 58, 81
- Stock S., et al., 2020, *Astronomy & Astrophysics*, 643, A112 84
- Stone E. C., Cummings A. C., McDonald F. B., Heikkilä B. C., Lal N., Webber W. R., 2013, *Science*, 341, 150 16, 21, 62, 90, 92, 111, 124
- Stone E. C., Cummings A. C., Heikkilä B. C., Lal N., 2019, *Nature Astronomy*, 3, 1013 16, 90, 111, 124
- Strauss R. D., Potgieter M. S., 2014, *Solar Physics*, 289, 3197 21, 24, 107, 124, 125
- Strauss R. D., Potgieter M. S., Büsching I., Kopp A., 2012, *Astrophysics & Space Science*, 339, 223 20, 24, 107
- Strong A. W., Moskalenko I. V., Ptuskin V. S., 2007, *Annual Review of Nuclear and Particle Science*, 57, 285 76
- Suzuki T. K., Inutsuka S.-i., 2005, *Astrophysical Journal Letters*, 632, L49 32, 85
- Suzuki T. K., Imada S., Kataoka R., Kato Y., Matsumoto T., Miyahara H., Tsuneta S., 2013, *Publications of the Astronomical Society of Japan*, 65, 98 32, 39, 42, 43, 85
- Svensmark H., 2006, *Astronomische Nachrichten*, 327, 871 24, 56, 61, 82, 91, 113
- Svensmark H., Friis-Christensen E., 1997, *Journal of Atmospheric and Solar-Terrestrial Physics*, 59, 1225 18, 58, 81
- Svensmark H., Enghoff M. B., Shaviv N. J., Svensmark J., 2017, *Nature Communications*, 8, 2199 18, 58, 81
- Tabataba-Vakili F., Grenfell J. L., Griesmeier J. M., Rauer H., 2016, *Astronomy & Astrophysics*, 585, A96 5, 24, 57, 77, 81, 95
- Tarter J. C., et al., 2007, *Astrobiology*, 7, 30 57

- Tilley M. A., Segura A., Meadows V., Hawley S., Davenport J., 2019, *Astrobiology*, 19, 64 5, 30, 57, 80
- Tinetti G., et al., 2021, arXiv e-prints, p. arXiv:2104.04824 24, 101, 106
- Tomczyk S., McIntosh S. W., Keil S. L., Judge P. G., Schad T., Seeley D. H., Edmondson J., 2007, *Science*, 317, 1192 15
- Turnbull M. C., 2015, arXiv e-prints, p. arXiv:1510.01731 59
- van Leeuwen F., 2007, *Astronomy & Astrophysics*, 474, 653 67
- van der Holst B., Sokolov I. V., Meng X., Jin M., Manchester W. B. I., Tóth G., Gombosi T. I., 2014, *Astrophysical Journal*, 782, 81 86, 108
- Vedantham H. K., et al., 2020, *Nature Astronomy*, 4, 577 100
- Vida K., Kővári Z., Pál A., Oláh K., Kriskovics L., 2017, *Astrophysical Journal*, 841, 124 5, 30, 57, 80
- Vidotto A. A., 2021, *Living Reviews in Solar Physics*, 18, 3 9, 58, 63, 80
- Vidotto A. A., Bourrier V., 2017, *Monthly Notices of the Royal Astronomical Society*, 470, 4026 9, 11, 12, 30, 44, 45, 46, 52, 58, 64, 67, 68, 81
- Vidotto A. A., Cleary A., 2020, *Monthly Notices of the Royal Astronomical Society*, 494, 2417 80
- Vidotto A. A., Donati J. F., 2017, *Astronomy & Astrophysics*, 602, A39 11, 30, 58, 81
- Vidotto A. A., Jatenco-Pereira V., 2006, *Astrophysical Journal*, 639, 416 14, 31, 33, 35, 48
- Vidotto A. A., Jatenco-Pereira V., 2010, *Advances in Space Research*, 46, 509 32, 85
- Vidotto A. A., Jardine M., Opher M., Donati J. F., Gombosi T. I., 2011, *Monthly Notices of the Royal Astronomical Society*, 412, 351 80
- Vidotto A. A., Jardine M., Morin J., Donati J. F., Lang P., Russell A. J. B., 2013, *Astronomy & Astrophysics*, 557, A67 5, 80
- Vidotto A. A., Jardine M., Morin J., Donati J. F., Opher M., Gombosi T. I., 2014a, *Monthly Notices of the Royal Astronomical Society*, 438, 1162 5, 30, 57, 63, 80, 86, 107

BIBLIOGRAPHY

- Vidotto A. A., et al., 2014b, *Monthly Notices of the Royal Astronomical Society*, 441, 2361 7, 9
- Vidotto A. A., Feeney N., Groh J. H., 2019, *Monthly Notices of the Royal Astronomical Society*, 488, 633 76
- Villarreal D'Angelo C., Jardine M., See V., 2018, *Monthly Notices of the Royal Astronomical Society*, 475, L25 11
- Villarreal D'Angelo C., Vidotto A. A., Esquivel A., Hazra G., Youngblood A., 2021, *Monthly Notices of the Royal Astronomical Society*, 501, 4383 46, 52
- Vos E. E., Potgieter M. S., 2015, *Astrophysical Journal*, 815, 119 20, 21, 22, 23, 62, 92, 107, 113, 122
- Wargelin B. J., Drake J. J., 2001, *Astrophysical Journal Letters*, 546, L57 58, 81
- Wargelin B. J., Drake J. J., 2002, *Astrophysical Journal*, 578, 503 30, 58, 81
- Weber E. J., Davis Leverett J., 1967, *Astrophysical Journal*, 148, 217 34
- Welsh B. Y., Lallement R., Vergely J. L., Raimond S., 2010, *Astronomy & Astrophysics*, 510, A54 9
- West A. A., et al., 2004, *Astronomical Journal*, 128, 426 5, 57, 80
- West A. A., Hawley S. L., Bochanski J. J., Covey K. R., Reid I. N., Dhital S., Hilton E. J., Masuda M., 2008, *Astronomical Journal*, 135, 785 5, 57
- West A. A., Weisenburger K. L., Irwin J., Berta-Thompson Z. K., Charbonneau D., Dittmann J., Pineda J. S., 2015, *Astrophysical Journal*, 812, 3 5, 57, 80
- Winebarger A. R., Warren H. P., 2004, *Astrophysical Journal Letters*, 610, L129 15, 31
- Winters J. G., et al., 2015, *Astronomical Journal*, 149, 5 4, 80
- Wood B. E., 2004, *Living Reviews in Solar Physics*, 1, 2 9, 10, 30, 58, 81, 107
- Wood B. E., Müller H.-R., Zank G. P., 2000, *Astrophysical Journal*, 542, 493 89, 111
- Wood B. E., Linsky J. L., Müller H.-R., Zank G. P., 2001, *Astrophysical Journal Letters*, 547, L49 10, 11, 30, 107, 109, 111

- Wood B. E., Müller H.-R., Zank G. P., Linsky J. L., 2002, *The Astrophysical Journal*, 574, 412–30
- Wood B. E., Müller H.-R., Zank G. P., Linsky J. L., Redfield S., 2005, *The Astrophysical Journal*, 628, L143–30
- Wood B. E., Müller H.-R., Redfield S., Edelman E., 2014, *The Astrophysical Journal*, 781, L33–58
- Wood B. E., et al., 2021, *Astrophysical Journal*, 915, 37–9, 11, 12, 13, 81, 82, 83, 84, 87, 107
- Yadav R. K., Christensen U. R., Wolk S. J., Poppenhaeger K., 2016, *Astrophysical Journal Letters*, 833, L28–122
- Zendejas J., Segura A., Raga A. C., 2010, *Icarus*, 210, 539–5

BIBLIOGRAPHY

Nederlandse Samenvatting

In dit proefschrift heb ik de interactie tussen M dwerg winden en galactische kosmische straling en hun mogelijke effecten op de bewoonbaarheid van exoplaneten onderzocht. Fig. 1 toont een schema dat het hier bestudeerde systeem samenvat. De interactie tussen het interstellair medium en de stellaire wind creëert een gebied rond de ster dat de astrosfeer wordt genoemd. Buiten de astrosfeer diffunderen Galactische kosmische stralen door de Melkweg en hun intensiteit wordt beschreven door de lokale interstellair spectrumwaarden. Om door de astrosfeer te dringen, moeten galactische kosmische stralen de gemagnetiseerde sterrenwind overwinnen. Eenmaal in de astrosfeer kunnen galactische kosmische stralen interageren met planeten die rond de ster draaien. De belangrijkste parameters om dit systeem te beschrijven zijn de eigenschappen van de stellaire wind, de eigenschappen van het interstellair medium (ISM) en de beschrijving van het transport van kosmische straling.

M dwergen, die bewoonbare zones in de buurt hebben, zijn de perfecte kandidaten voor observaties van mogelijk bewoonbare exoplaneten. Hun winden zijn echter zwak en uitdagend om te observeren. In dit proefschrift heb ik numerieke simulaties gebruikt om de sterwinden van Mdweren te beschrijven. In het bijzonder heb ik een 1D MHD Alfvén-golfgedreven windmodel gebruikt waarin de stellaire wind wordt verwarmd en versneld door Alfvén golven die aan de basis van de wind worden gegenereerd. De simulatieruimteparameter wordt beperkt door gebruik te maken van waarneembare parameters, zoals massaverliessnelheid, röntgenhelderheid en magnetisch veld. Observatiebeperkingen zijn niet altijd beschikbaar en soms zijn ze niet voldoende om mogelijke degeneratie in de modellen te overwinnen. Dat is het geval met GJ 436 stellaire wind, besproken in Hoofdstuk 2. Door gebruik te maken van röntgenwaarnemingen werd de massaverliessnelheid van GJ 436 tot een bovengrens beperkt ($\dot{M} < 7.6 \times 10^{-15} M_{\odot} \text{ yr}^{-1}$). Deze bovengrens zou echter kunnen worden gereproduceerd door verschillende waarden van het stellaire magnetische veld. Dit laat zien hoe belangrijk observatiebeperkingen zijn om sterrenwindmodellen te beschrijven.

Stellaire windmodellen geven ons informatie over de windeigenschappen, zoals magnetisch veld, eindsnelheid en massaverlies. Gecombineerd met ISM-eigenschappen binnen elke ster, kan de astrosfeerafstand worden geschat. Hoofdstukken 3, 4 en 5 laten de diversiteit zien van astrosferische afmetingen die gevonden worden binnen verschillende

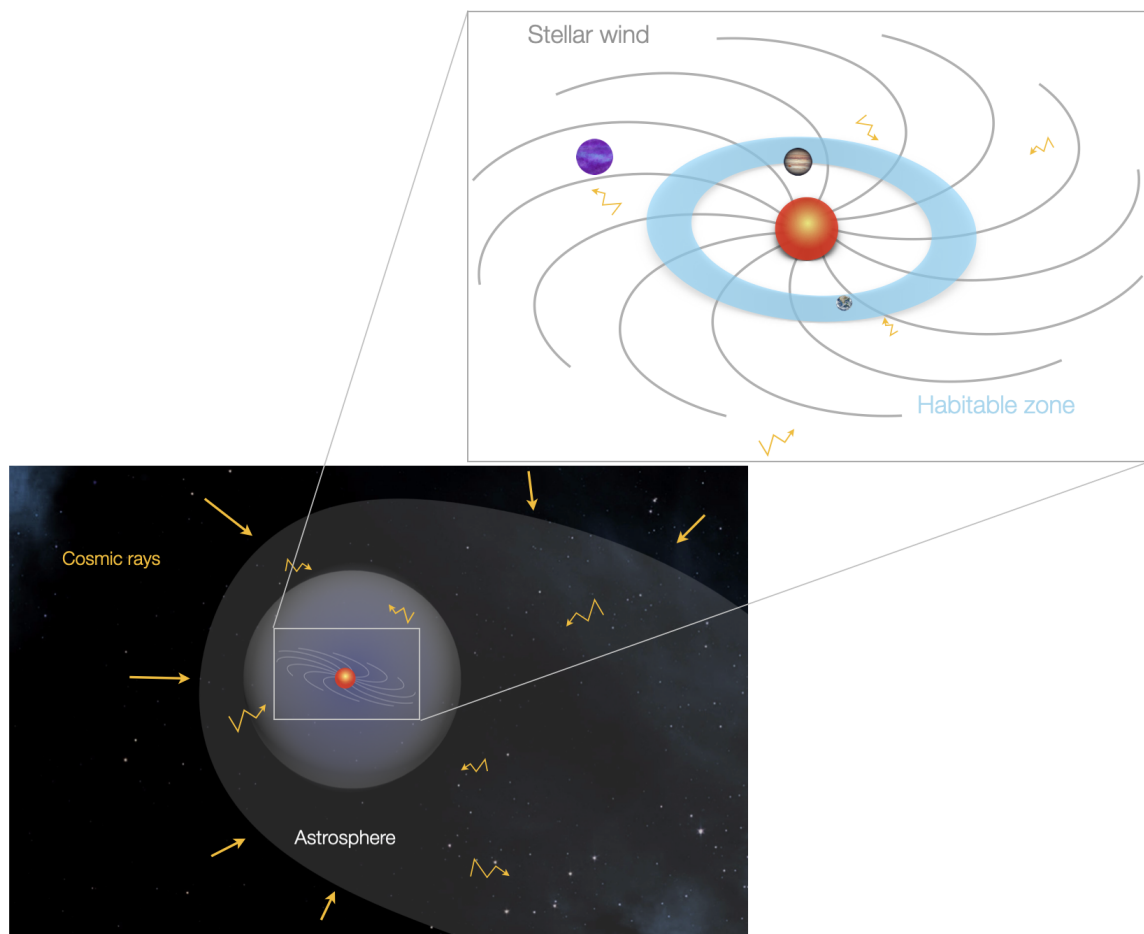


Figure 1: Schema van het sterrenstelsel dat in dit proefschrift wordt bestudeerd. De interactie tussen het ISM en de sterrenwind leidt tot een Astrosfeer. Buiten de Astrosfeer verspreiden Galactische kosmische stralen zich door de Melkweg. Om de Astrosfeer binnen te dringen, moeten galactische kosmische stralen de gemagnetiseerde sterrenwind overwinnen. In de Astrosfeer kunnen Galactische kosmische stralen interageren met de gastplaneten.

M dwergen, variërend van 6 tot 6140 au voor de steekproef van sterren die hier wordt bestudeerd.

Kosmische straling is belangrijk in de context van planetaire bewoonbaarheid. Metingen van galactische kosmische stralen die de aarde bereiken, worden al vele jaren gedaan. Bovendien zijn kosmische stralingstransportmodellen om de voortplanting van galactische kosmische straling naar de aarde te beschrijven uitgebreid gebruikt om de effecten van kosmische straling op aarde te begrijpen. De effecten van kosmische straling rond andere exoplaneten zijn echter niet goed begrepen. Helaas zijn metingen van kosmische straling op andere planeten nog steeds niet mogelijk. Om de voortplanting van galactische kosmische straling door M dwergen in dit proefschrift te beschrijven

en te bestuderen, heb ik een 1D kosmisch stralingstransportmodel gebruikt. Deze simulaties kwantificeren de flux van galactische kosmische straling die elke afstand in de atmosfeer bereikt.

Het stellaire magnetische veld en de windsnelheid spelen een essentiële rol bij de voortplanting van galactische kosmische straling. Een sterker stellair magnetisch veld resulteert bijvoorbeeld in een grotere onderdrukking van de intensiteit van galactische kosmische straling (voor vaste turbulentie-eigenschappen en in vergelijking met een lagere magnetische veldsterkte). Dit kan worden verklaard door het feit dat een sterk magnetisch veld kleinere diffusiecoëfficiënten impliceert. Als gevolg hiervan worden advectionele processen belangrijker, wat resulteert in lagere fluxen van galactische kosmische straling. Vergelijkbaar, maar in mindere mate, resulteert een sterkere stellaire windsnelheid ook in een lagere intensiteit van galactische kosmische straling in de atmosfeer (vergeleken met een zwakke stellaire windsnelheid). Dit komt omdat een sterkere stellaire windsnelheid meer advectione impliceert, wat de flux van galactische kosmische straling verzwakt.

De stellaire massaverliessnelheid (of stellaire winddichtheid) heeft geen directe invloed op de intensiteit van kosmische straling, aangezien de stellaire winddichtheid erg laag is. Het heeft echter wel invloed op de grootte van de atmosfeer (via de drukbalans). De fluxen van galactische kosmische straling kunnen echter worden beïnvloed door variaties in de atmosferische grootte. Als het fysieke proces wordt gedomineerd door diffusie, heeft de atmosferische grootte geen effect op de onderdrukking van kosmische straling. Dit is het geval bij GJ 436 (zie Hoofdstuk 3) en GJ 338B (zie Hoofdstuk 4). Aan de andere kant, als advectione het dominante proces is, kan de grootte van de atmosfeer de flux van galactische kosmische straling beïnvloeden. Dit is het geval bij AU Mic (zie Hoofdstuk 5). Samengevat, door advectionele gedomineerde systemen leiden tot een sterkere onderdrukking van kosmische straling, terwijl diffusie-gedomineerde systemen tot weinig (of geen) modulatie leiden.

Net als wat er voor de Aarde gebeurt, beïnvloedt het opnemen van driftsnelheden van deeltjes, als gevolg van gradiënten en krommingen van het stellaire magnetische veld, ook de voortplanting van galactische kosmische straling door M-dwergastrosferen (zie Hoofdstuk 5). Over het algemeen werd voor de twee sterren, waarin de deeltjesdrift was opgenomen, Prox Cen en AU Mic, een grotere flux van galactische kosmische straling waargenomen (vergeleken met simulaties zonder de opname van deeltjesdrift). Dit kan worden verklaard door het feit dat beide systemen een negatieve driftsnelheid hadden bij de onderzochte radiale schijf, wat resulteerde in een grotere intensiteit

van kosmische straling. Dit komt door het feit dat deeltjesdrift gewoon als een extra advectioneel proces in het transportmodel fungeert.

In het hier bestudeerde monster, met 8 M dwergen en 12 planeten, ontvangen de meeste exoplaneten een veel lagere flux van galactische kosmische straling dan de waarden die op aarde zijn waargenomen. De uitzondering is GJ 15A c, die een grotere halve lange as heeft en een flux heeft die vergelijkbaar is met de aarde, en GJ 411 c, die ook een grotere halve lange as heeft en Galactische kosmische straling ontvangt fluxen vergelijkbaar met het lokale interstellair spectrum (LIS). De bewoonbare zone van drie sterren, GJ 411, GJ 436 en GJ 887, bleek vergelijkbare galactische kosmische stralingsfluxen te hebben met de waarden van de aarde, terwijl de andere sterren (AU Mic, GJ 15A, GJ273, GJ 338B en Prox Cen) krijgen een lagere flux.

Ten slotte kunnen de hier gevonden resultaten belangrijk zijn voor het begrijpen van toekomstige waarnemingen van de atmosfeer van exoplaneten met JWST en ARIEL. Bovendien zullen de waarnemingen van de exoplaneet atmosfeer ons in staat stellen om de fluxen van kosmische straling in de atmosfeer van exoplaneten te beperken en mogelijk helpen om de bewoonbaarheidspuzzel te voltooien.

English Summary

In this thesis, I have investigated the interaction between M dwarf winds and Galactic cosmic rays and their possible effects on exoplanets' habitability. Fig. 1 shows a schematic that summarises the system studied here. The interstellar medium and stellar wind interaction create a region around the star called the astrosphere. Outside the astrosphere, Galactic cosmic rays diffuse throughout the Galaxy and their intensity is described by the local interstellar spectrum values. To penetrate through the astrosphere, Galactic cosmic rays have to overcome the magnetised stellar wind. Once inside the astrosphere, Galactic cosmic rays can interact with planets orbiting the star. The main parameters to describe this system are the stellar wind properties, the interstellar medium (ISM) properties and the cosmic ray transport description.

M dwarfs, which have close-in habitable zones, are the perfect candidates for observations of potentially habitable exoplanets. However, their winds are tenuous and challenging to observe. In this thesis, I have used numerical simulations to describe the stellar winds of M dwarfs. In particular, I have used a 1D MHD Alfvén-wave-driven wind model in which the stellar wind is heated and accelerated by Alfvén waves induced at the base of the wind. The simulation space parameter is constrained by using observable parameters, such as mass-loss rate, X-ray luminosity, and magnetic field. Observational constraints are not always available and sometimes they are not enough to overcome possible degeneracy in the models. That is the case of GJ 436 stellar wind, discussed in Chapter 2. By using X-ray observations, GJ 436's mass-loss rate was constrained to an upper limit ($\dot{M} < 7.6 \times 10^{-15} M_{\odot} \text{ yr}^{-1}$). However, this upper limit could be reproduced by different values of stellar magnetic field. This shows how important observational constraints are to describe stellar wind models.

Stellar wind models give us information on the wind properties, such as magnetic field, terminal velocity and mass-loss rate. Combined with ISM properties within each star, the astrosphere distance can be estimated. Chapters 3, 4 and 5 show the diversity of astrospheric sizes found within different M dwarfs, varying from 6 to 6140 au for the sample of stars studied here.

Cosmic rays are important in the context of planetary habitability. Measurements of Galactic cosmic rays reaching Earth have been made for many years. Additionally, cosmic ray transport models to describe the propagation of Galactic cosmic rays to

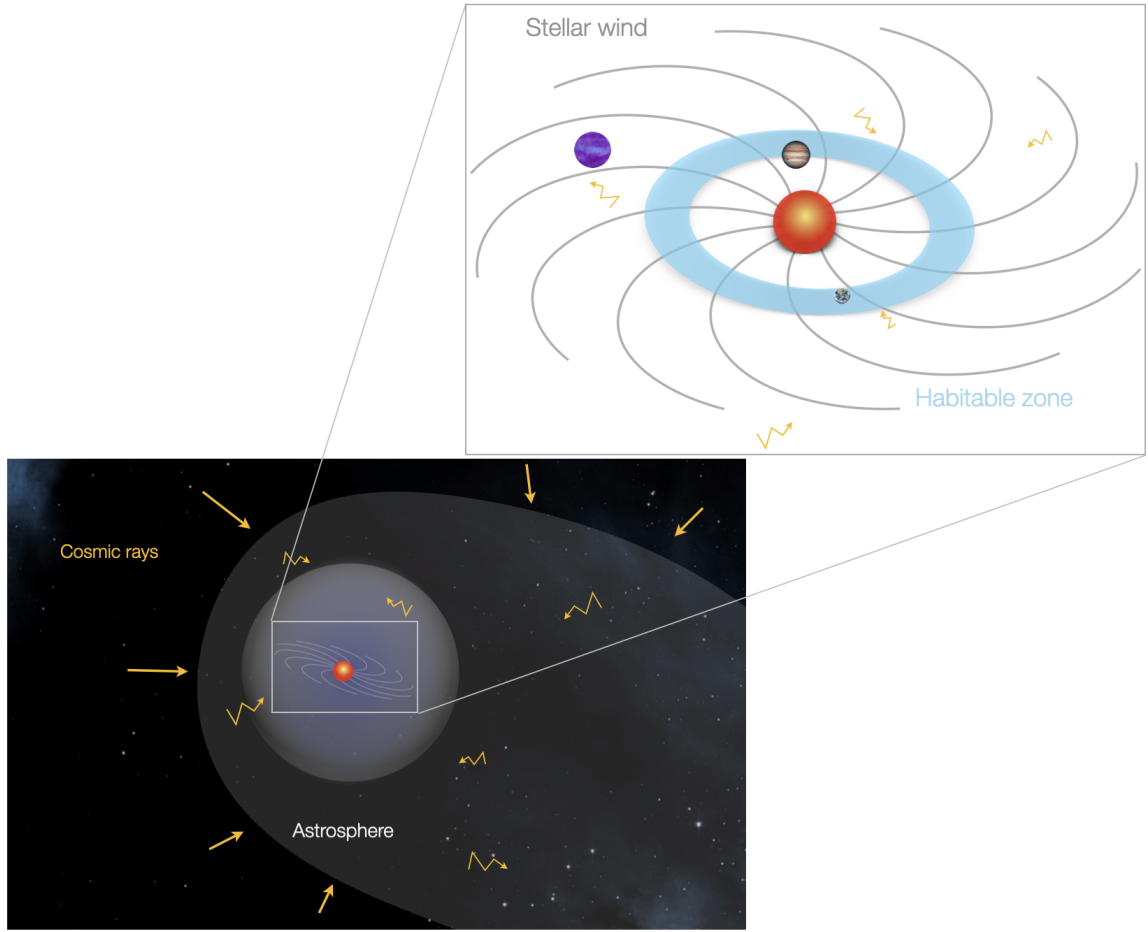


Figure 1: Schematic of the stellar system studied in this thesis. The interaction between the ISM and the stellar wind gives rise to an astrosphere. Outside the astrosphere, Galactic cosmic rays diffuse throughout the Galaxy. To penetrate the astrosphere, Galactic cosmic rays need to overcome the magnetised stellar wind. When inside the astrosphere Galactic cosmic rays can interact with the host planets.

Earth have been extensively used to understand the effects of cosmic rays at Earth. However, the effects of cosmic rays around other exoplanets are not well understood. Unfortunately, measurements of cosmic rays on other planets are still not possible. To describe and study the propagation of Galactic cosmic rays through M dwarfs in this thesis, I have used a 1D cosmic ray transport model. These simulations quantify the flux of Galactic cosmic rays reaching any distance in the astrosphere.

The stellar magnetic field and the wind velocity play an essential role in the propagation of Galactic cosmic rays. For instance, a stronger stellar magnetic field result in a larger suppression in the intensity of Galactic cosmic ray (for for fixed turbulence properties, and when compared with a lower magnetic field strength). This can be explained by the fact that a strong magnetic field implies smaller diffusion coefficients. As

a consequence, advective processes become more important, resulting in lower Galactic cosmic ray fluxes. Similar, but to a lesser extent, a stronger stellar wind velocity also results in a lower intensity of Galactic cosmic rays in the astrosphere (when compared with a weak stellar wind velocity). This is because a stronger stellar wind velocity implies more advection, which attenuates the flux of Galactic cosmic rays.

The stellar mass-loss rate (or stellar wind density) does not influence the intensity of cosmic rays directly, as the stellar wind density is very low. However, it does affect the size of the astrosphere (through the pressure balance). The Galactic cosmic ray fluxes, however, may be affected by variations in the astrospheric size. If the physical process is dominated by diffusion, the astrospheric size has no effect on the suppression of cosmic rays. This is the case of GJ 436 (see Chapter 3) and GJ 338B (see Chapter 4). On the other hand, if advection is the dominant process, the size of the astrosphere can affect the flux of Galactic cosmic rays. This is the case of AU Mic (see Chapter 5). In summary, advective-dominated systems lead to stronger suppression of cosmic rays, while diffusion-dominated systems lead to little (or no) modulation.

Similar to what happens for Earth, the inclusion of particle drift velocities, due to gradients and curvatures of the stellar magnetic field, also affects the propagation of Galactic cosmic rays through M dwarf astrospheres (see Chapter 5). Overall, for the two stars, in which the particle drift was included, Prox Cen and AU Mic, a larger flux of Galactic cosmic rays was observed (when compared with simulations without the inclusion of particle drift). This can be explained by the fact that both systems had a negative drift velocity at the investigated radial slice, resulting in a larger intensity of cosmic rays. This is due to the fact that particle drift acts simply as an extra advective process in the transport model.

In the sample studied here, with 8 M dwarfs and 12 planets, the majority of exoplanets receive a much lower flux of Galactic cosmic rays than values observed at Earth. The exception, is GJ 15A c, which has a larger semi-major axis and has a flux comparable with the Earth, and GJ 411 c, which also has a larger semi-major axis and receives Galactic cosmic ray fluxes similar to the local interstellar spectrum (LIS). The habitable zone of three stars, GJ 411, GJ 436 and GJ 887 was found to have comparable Galactic cosmic ray fluxes with Earth's values, while the other stars (AU Mic, GJ 15A, GJ273, GJ 338B and Prox Cen) receive a lower flux.

Finally, the results found here may be important to understanding future exoplanet atmosphere observations with JWST and ARIEL. In addition, the exoplanet atmosphere observations will enable us to constrain cosmic ray fluxes in exoplanet atmospheres and possibly help to complete the habitability “puzzle”.

ENGLISH SUMMARY

Publications

Amanda L. Mesquita, Donna Rodgers-Lee, Aline A. Vidotto, & Robert D. Kavanagh. *The strong suppression of Galactic cosmic rays reaching AU Mic b, c and Prox Cen b*
2022, MNRAS, 515, 1218–1227

Amanda L. Mesquita, Donna Rodgers-Lee, Aline A. Vidotto, Dimitra Atri, & Brian E. Wood. *Galactic cosmic ray propagation through M dwarf planetary systems.*
2022, MNRAS, 509, 2091–2101

Donna Rodgers-Lee, Aline A. Vidotto, & **Amanda L. Mesquita**. *Charting nearby stellar systems: the intensity of Galactic cosmic rays for a sample of solar-type stars.*
2021, MNRAS, 508, 4696–4704

Amanda L. Mesquita, Donna Rodgers-Lee, & Aline A. Vidotto. *The Earth-like Galactic cosmic ray intensity in the habitable zone of the M dwarf GJ 436.*
2021, MNRAS, 505, 1817–1826

Amanda L. Mesquita, & Aline A. Vidotto. *Global trends in winds of M dwarf stars.*
2020, MNRAS, 494, 1297–1307

PUBLICATIONS

Curriculum Vitae

I was born in Lavras, Minas Gerais, Brazil, on June 10, 1992. However, I grew and lived the majority of my life in a small countryside village called Ijaci, situated ~ 12 km away from Lavras.

As far as I remember, I liked maths and science. For this reason, I decided to study physics as my undergrad. My BSc was done mainly at *Universidade Federal de Lavras* with one year at *Universidad de Valladolid* as part of the government project “science without borders”. My BSc’s final year project was associated with the study of specific heat of crystalline solids supervised by Prof. Antônio Silva.

By the end of my BSc, I decided to start a Master’s. I receive a scholarship from *Instituto Nacional de Pesquisas Spaciais* for a two-year MCs program in space geophysics. This was when I had more contact with astrophysics and started to appreciate the subject more. During my MCs, I worked with solar coronal mass ejections observed by the LASCO instrument under the supervision of Prof. Alisson Dal Lago. My research focused on the prediction of coronal mass ejection’s arrival at Earth using an algorithm to track and calculate the kinematic properties of these ejections.

I had a good experience during my MCs and decided to do a PhD. Initially, I started a PhD at *Instituto Nacional de Pesquisas Spaciais* for almost a year to extend my Master’s project. I was then offered a scholarship to do a PhD abroad at Trinity College Dublin and decided it would be better for my career. During three of the four-year PhD program, my PhD was at Trinity College. However, for my last year, with my research group, I relocated to Leiden. Under the supervisor Dr. Aline Vidotto and Dr. Donna Rodgers-Lee, I worked with numerical simulations of stellar winds and cosmic rays. I focused on M dwarfs and the effects of Galactic cosmic rays within their environment.

CURRICULUM VITAE

Acknowledgements

During my PhD, many people helped me in many different aspects and for this reason, I am very thankful to everyone. I would like to especially thank my parents, Lúcia and João, and my sister Tamiris for their love and support during my life, particularly during this time abroad.

I would like to thank my supervisors, Donna and Aline, for their support and guidance during my academic life and everyone in our group, all the PhDs and postdocs.

To everyone in our office in Dublin, thanks for making my days a lot easier, for helping me improve my English (even when it was difficult to understand the Irish accent), and for the many board games we played together. Thanks to Marina and Thais for helping me during difficult moments in my life and also for giving me great input.

As an international student, I feel obliged to thank everyone in Dublin and in Leiden that helped me with visas, houses, and many other trivial things associated with moving to another country.

A special thanks to my partner, who have always supported me during difficult times in my academic life, and also for staying many nights awake while I was writing my thesis.